PLOS BIOLOGY

Comparative genomics of the closely related fungal genera *Cryptococcus* and *Kwoniella* reveals karyotype dynamics and suggests evolutionary mechanisms of pathogenesis
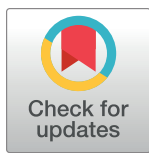
Marco A. Coelho[1]☉, Márcia David-Palma[1]☉, Terrance Shea[2], Katharine Bowers[2], Sage McGinley-Smith[2], Arman W. Mohammad[2], Andreas Gnirke[2], Andrey M. Yurkov[3], Minou Nowrousian[4], Sheng Sun[1]*, Christina A. Cuomo[2‡]*, Joseph Heitman[1‡]*

1 Department of Molecular Genetics and Microbiology, Duke University Medical Center, Durham, North Carolina, United States of America, 2 Broad Institute of MIT and Harvard, Cambridge, Massachusetts, United States of America, 3 Leibniz Institute DSMZ-German Collection of Microorganisms and Cell Cultures, Braunschweig, Germany, 4 Lehrstuhl für Molekulare und Zelluläre Botanik, Ruhr-Universität Bochum, Bochum, Germany

☉ These authors contributed equally to this work.
‡ CAC and JH also contributed equally to this work. CAC and JH are joint senior authors on this work.
* sheng.sun@duke.edu (SS); cuomo@broadinstitute.org (CAC); heitm001@duke.edu (JH)

Abstract

In exploring the evolutionary trajectories of both pathogenesis and karyotype dynamics in fungi, we conducted a large-scale comparative genomic analysis spanning the *Cryptococcus* genus, encompassing both global human fungal pathogens and nonpathogenic species, and related species from the sister genus *Kwoniella*. Chromosome-level genome assemblies were generated for multiple species, covering virtually all known diversity within these genera. Although *Cryptococcus* and *Kwoniella* have comparable genome sizes (about 19.2 and 22.9 Mb) and similar gene content, hinting at preadaptive pathogenic potential, our analysis found evidence of gene gain (via horizontal gene transfer) and gene loss in pathogenic *Cryptococcus* species, which might represent evolutionary signatures of pathogenic development. Genome analysis also revealed a significant variation in chromosome number and structure between the 2 genera. By combining synteny analysis and experimental centromere validation, we found that most *Cryptococcus* species have 14 chromosomes, whereas most *Kwoniella* species have fewer (11, 8, 5, or even as few as 3). Reduced chromosome number in *Kwoniella* is associated with formation of giant chromosomes (up to 18 Mb) through repeated chromosome fusion events, each marked by a pericentric inversion and centromere loss. While similar chromosome inversion–fusion patterns were observed in all *Kwoniella* species with fewer than 14 chromosomes, no such pattern was detected in *Cryptococcus*. Instead, *Cryptococcus* species with less than 14 chromosomes showed reductions primarily through rearrangements associated with the loss of repeat-rich centromeres. Additionally, *Cryptococcus* genomes exhibited frequent interchromosomal translocations, including intercentromeric recombination facilitated by transposons shared between centromeres. Overall, our findings advance our understanding of genetic changes possibly associated with pathogenicity in *Cryptococcus* and provide a

foundation to elucidate mechanisms of centromere loss and chromosome fusion driving distinct karyotypes in closely related fungal species, including prominent global human pathogens.

Introduction

Human fungal pathogens are estimated to be responsible for over 1.5 million deaths worldwide annually [1]. Growing concern regarding invasive fungal diseases led the World Health Organization (WHO) to publish its first list of priority fungal pathogens, with *Cryptococcus neoformans* ranked first in the critical group [2]. Even though direct selection of traits favoring human virulence or infection is not expected because humans are not the natural hosts for any pathogenic *Cryptococcus* species, interactions of these yeasts with other eukaryotes in their natural environments could select traits that enhance virulence in mammals [3–6]. Exploring the evolutionary trajectories of pathogenic and nonpathogenic *Cryptococcus* species and closely related genera can provide insights into the broader mechanisms that govern fungal evolution and shed light on why some species, but not others, have evolved traits that cause pathogenesis in humans [7,8].

The genus *Cryptococcus* encompasses diverse species, including both pathogenic and closely related nonpathogenic saprobic species [9–12]. Within the pathogenic clade, there are 7 recognized species that can be pathogenic for both immunocompromised and immunocompetent individuals [13–15]: *Cryptococcus neoformans*, *Cryptococcus deneoformans*, and 5 species within the *Cryptococcus gattii* species complex [9]. The *C. gattii* complex also includes another recently discovered lineage described as *C. gattii* VGV [16], which has not yet been linked to human infection. The nonpathogenic species include *Cryptococcus wingfieldii*, *Cryptococcus amylolentus*, *Cryptococcus floricola*, *Cryptococcus depauperatus*, and *Cryptococcus luteus* [11,12,17,18]. Phylogenetically, the genus *Kwoniella* is considered the closest relative to *Cryptococcus* [17–19]. All known *Kwoniella* species are saprophytic and found in diverse ecological niches ranging from insect frass and soil to plant debris, illustrating their broad environmental adaptability [10,20–22]. Additionally, while most *Cryptococcus* species exhibit well-defined sexual reproduction cycles [11,12,23–25], sexual reproduction has so far been documented in only 2 *Kwoniella* species (*Kwoniella mangrovensis* and *Kwoniella heveanensis*) [20,21], with many species known from only a few isolated strains [26], which complicates efforts to fully understand their reproductive strategies and genetic diversity.

Although *Cryptococcus* and *Kwoniella* genome assemblies have improved in quality and completeness in recent years [11,12,27–29], there has been no comprehensive comparative genomic study so far that leverages complete genome assemblies. By comparing chromosome-level genome assemblies of multiple strains and species, we can now identify the extent of collinearity between the chromosomes of different species and infer structural variation, as well as identify specific regions where variation occurs, with a high degree of accuracy. Chromosomal rearrangements, including inversions, translocations, fusions, and fissions, underlie the extensive karyotypic variability seen across eukaryotes [30–32]. These sources of structural variation aid organisms in adapting to diverse environments [33,34], influence changes in mating systems [27,35–37], drive the evolution of pathogenic traits [38–40], and play roles in speciation [41–45].

Chromosome number reduction is common in eukaryotes and often results from chromosome fusion events. This is exemplified in several muntjac deer species, where karyotype

changes occurred through chromosome fusion during speciation [45], in the formation of the extant human chromosome 2 [46,47], in chromosome number reduction in the plant *Arabidopsis thaliana* [48,49], and in the nematode *Diploscapter pachys* that achieved a single-chromosome karyotype through fusion of 6 ancestral chromosomes [50]. In fungi, telomere-to-telomere fusions altering chromosome numbers are also observed, such as in Ascomycota yeast species [51], and in *Fusarium graminearum*, where chromosome fusion has led to a reduced karyotype compared to related species, with the sites of fusion corresponding to former subtelomeric regions retaining high genetic diversity and heterochromatin marks [52–54]. Similarly, chromosome fusion is suggested to underlie karyotype reduction in Basidiomycota *Malassezia* species [55,56].

Here, we explored the genomic characteristics of *Cryptococcus* and *Kwoniella* species, focusing on karyotype and gene variation. We generated high-quality chromosome-level genome assemblies for 22 species, capturing most of the known diversity of the 2 genera. Analysis of structural variation across species revealed contrasting mechanisms of karyotype evolution. In *Kwoniella*, karyotypic variation was primarily driven by chromosome fusion events involving pericentric inversions and centromere loss, leading to chromosome numbers varying from 14 to as few as 3, without notable loss of genomic information. Interestingly, in species with only 3 chromosomes, one has evolved into a "giant" chromosome (approximately 16 to 18 Mb) formed by successive fusion events. In stark contrast, *Cryptococcus* species largely retained the ancestral karyotypic arrangement of 14 chromosomes, apart from 2 species where chromosome number reduction entailed substantial interchromosomal rearrangements and centromere inactivation through loss of repeat-rich sequences. We also examined gene content variation, finding that genes related to canonical pathogenesis phenotypes are highly conserved across all species, although some notable pathogen-specific gene signatures were identified. This study highlights key genetic characteristics of both genera and establishes a foundation for understanding pathogenesis evolution, centromere loss, and the role of chromosome fusions in the evolution and adaptation of these fungal species.

Results

Chromosome-level assemblies, genomic features, and phylogeny of *Cryptococcus* and *Kwoniella* species

We generated 22 chromosome-level genome assemblies for 7 *Cryptococcus* and 15 *Kwoniella* species by combining long- (Oxford Nanopore or PacBio) and short-read (Illumina) sequencing (**Figs 1A** and **S1**). This dataset includes 2 new *Cryptococcus* (isolates OR849 and OR918 [57]) and 4 new *Kwoniella* species (isolates B9012, CBS6097, CBS9459, and DSM27149) that will be formally described elsewhere (**Fig 1**). Five of the newly obtained *Cryptococcus* assemblies belong to pathogenic species known to cause disease in humans and animals: Four of these are improved assemblies of species within the *Cryptococcus gattii* complex, and the other one is an updated assembly of *C. deneoformans* reference strain JEC21. All of these assemblies have higher contiguity than their previous versions, which were in general more fragmented with many scaffolds and gaps and/or were not fully resolved at centromeres and chromosome ends (**S1 Appendix**). We also incorporated the genome assemblies of 7 other *Cryptococcus* species generated in previous studies [11,12,16,28,29,43,58] for comparative genomic analysis. This resulted in a comprehensive dataset of 14 *Cryptococcus* and 15 *Kwoniella* genomes, covering most of the currently known diversity within the 2 groups (**Figs 1A** and **S1** and **S1 Appendix**).

Gene set evaluation, following gene prediction and annotation (see Materials and methods and **S1 Appendix**), revealed a high level of completeness, with an average of 97.8% presence of
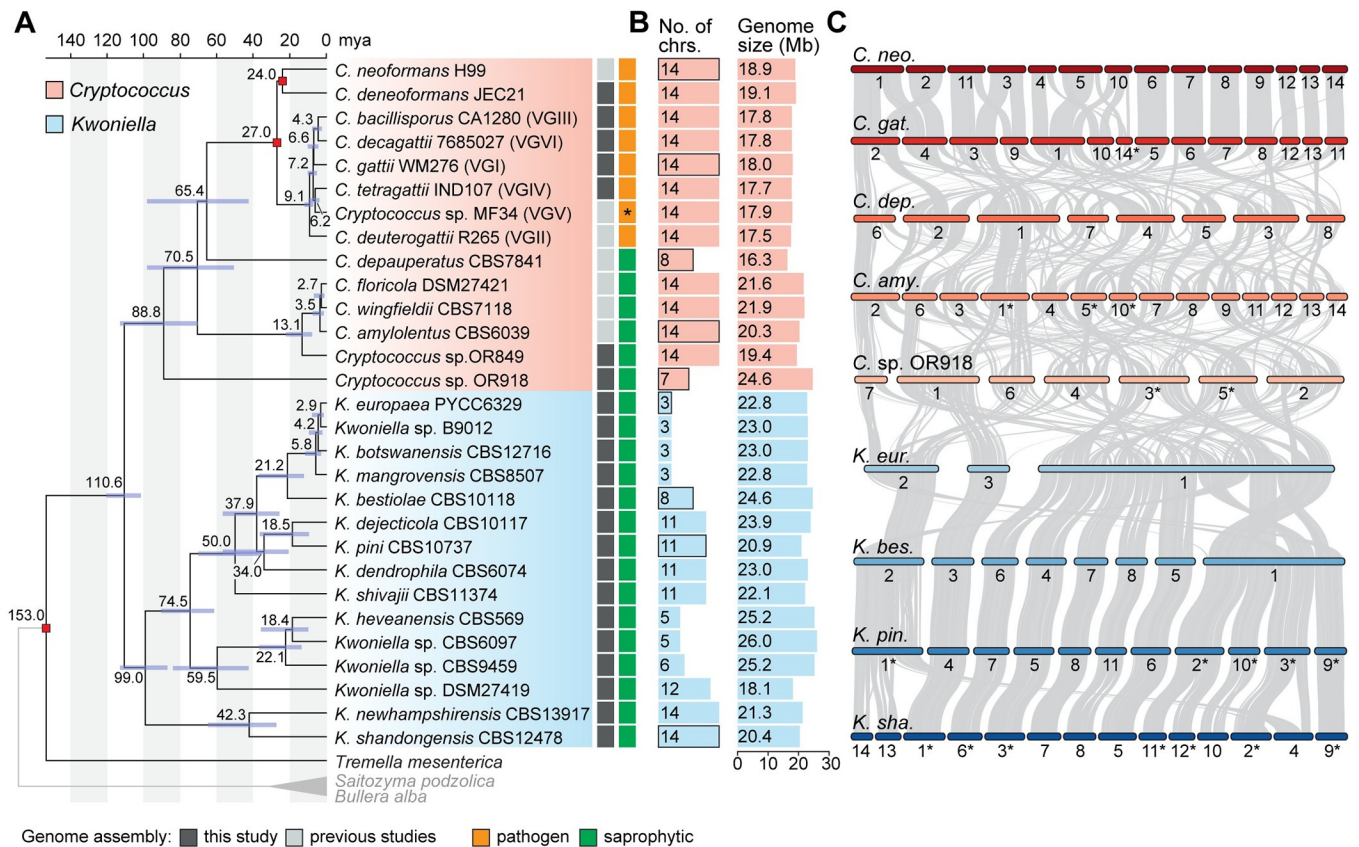
Fig 1. Molecular time tree for *Cryptococcus* and *Kwoniella* and genome composition. (A) Time tree including all *Cryptococcus* and *Kwoniella* strains analyzed in this study. Different genera are depicted by different-colored boxes as shown in the key. Divergence time estimation was conducted with the RelTime algorithm employing a phylogeny inferred by maximum likelihood analysis using a concatenation-based approach on a data matrix composed of protein alignments of 3,430 single-copy genes shared across all species and 3 outgroups. All branches are 100% supported (SH-aLRT and UFboot tests; see **S1** Fig). For dating estimation, *T. mesenterica* was included as ingroup and absolute divergence time estimates were calibrated using the following constraints: separation of *T. mesenterica* from other species [153.0 million years ago (mya)], the origin of the pathogenic *Cryptococcus* species (27.0 mya) and the *C. neoformans* and *C. deneoformans* split (24 mya). Blue boxes around each internode correspond to 95% divergence time confidence intervals for each branch of the phylogeny. Complete genome sequences obtained in this study are marked in dark gray. An asterisk indicates that VGV has not as yet been linked to human infection. **(B)** Number of chromosomes and genome size (Mb, megabase pair). **(C)** Pairwise synteny relationships between representative *Cryptococcus* and *Kwoniella* species with different number of chromosomes highlighting markedly distinct routes of karyotypic evolution (many interchromosomal rearrangements in *Cryptococcus* vs. chromosome fusion events in *Kwoniella*). Links represent the boundaries of syntenic gene blocks identified by MCScanX with pairwise homologous relationships determined by SynChro. Chromosomes were reordered and/or inverted (marked with asterisks) relative to their original assembly orientations to maximize collinearity. The data underlying this Figure can be found in **S1 Appendix** and at https://doi.org/10.5281/zenodo.11199354.

https://doi.org/10.1371/journal.pbio.3002682.g001

Benchmarking Universal Single-Copy Orthologs (BUSCO) genes from the fungal tremellomycetes_odb10 database, ranging from 93.9% to 99.7% (**S1C Fig**). This underscores the high quality of the assembled genomes and their gene sets. Further analysis showed that, on average, *Cryptococcus* genomes are smaller (16.3 to 24.6 Mb, average 19.2 Mb) compared to *Kwoniella* genomes (18.1 to 26.0 Mb, average 22.9 Mb) (**Figs 1B** and **S1H;** $P = 0.0004$, Mann–Whitney U Test). The larger sizes of *Kwoniella* genomes can be attributed to both a higher average number of predicted genes ($P = 0.004$, Mann–Whitney U Test) and longer introns ($P < 0.0001$, Mann–Whitney U Test) (**S1I–S1K Fig**). However, while larger genome sizes among *Cryptococcus* species is strongly correlated with a higher number of genes (Spearman's correlation coefficient $\rho = 0.86$, $P < 0.0001$), this association is less pronounced in *Kwoniella* ($\rho = 0.49$, $P = 0.0668$, **S1L Fig**), where longer introns appear to be a significant factor in genome size ($\rho = 0.91$, $P < 0.0001$; **S1M Fig**). Additionally, no significant correlation was found between the number

of introns per coding sequence and genome size changes within or between the 2 groups (**S1K** and **S1N Fig**).

Comparative genomic analysis revealed striking differences in chromosome numbers between the 2 genera. With the exception of 2 species, all other *Cryptococcus* species analyzed have 14 chromosomes, in contrast to *Kwoniella* where chromosome numbers range widely. Some species, like *Kwoniella shandongensis* and *Kwoniella newhampshirensis*, have 14 chromosomes, whereas others, such as *Kwoniella mangrovensis*, have as few as 3 chromosomes (**Fig 1B**). Owing to these variations in *Kwoniella*, we carried out pulsed-field gel electrophoresis and Hi-C mapping as additional validation measures to ensure accuracy of a subset of the assemblies, particularly for those species with fewer chromosomes. The combined results of both methods corroborated our assemblies (**S2 Fig**).

Prompted by these findings we conducted an in-depth investigation of the karyotypic evolution within and across these 2 genera. To provide a phylogenetic framework for subsequent evolutionary analysis, we first established phylogenetic relationships by identifying 3,430 single-copy genes shared across all *Cryptococcus* and *Kwoniella* species, and 3 outgroups (*Tremella mesenterica*, *Saitozyma podzolica*, and *Bullera alba*) selected based on their phylogenetic placement external to *Cryptococcus* and *Kwoniella*, as evidenced by previous studies [17], and the availability genome assemblies. Phylogenetic reconstructions based on a concatenation-based approach differentiated *Cryptococcus* and *Kwoniella* species into distinct clades and validated the status of some of the new isolates as distinct species, as evidenced by their clear phylogenetic separation and divergence (**Figs 1A** and **S1**). Estimation of the divergence times using the RelTime method and 3 calibration points [59,60] suggests that *Cryptococcus* and *Kwoniella* diverged from their last common ancestor about 110 million years ago (mya), with the initial splits within the 2 genera occurring around 90 and 100 mya, respectively (**Fig 1A**). While these divergence times generally align with other studies [61–63], we note that previous estimates suggested an earlier divergence for the last common ancestor of disease-causing Cryptococci, ranging from 40 to 100 mya, compared to approximately 27.0 mya estimated in our analysis (**Fig 1A**) [64,65]. Nevertheless, even if our analysis generally underestimates the divergence times, it still suggests that the initial divergence within the 2 genera occurred at roughly the same time.

Distinct modes of chromosome evolution in *Cryptococcus* and *Kwoniella*

To understand the pronounced differences in chromosome number between *Cryptococcus* and *Kwoniella*, a detailed analysis of chromosomal rearrangements was conducted based on whole-genome alignments from species with varying chromosome numbers in both groups. As shown in **Fig 1A** and **1C**, although the crown node times of *Cryptococcus* and *Kwoniella* are relatively similar, the 2 groups have experienced distinct types of chromosomal rearrangements throughout evolution. Within *Cryptococcus*, interchromosomal rearrangements predominate, whereas chromosome fusions are the dominant type of rearrangement within *Kwoniella* and seem to account for the extensive variation in chromosome number across species (**Fig 1C**). Previous studies have linked large-scale interchromosomal rearrangements in *Cryptococcus* to recombination within gene-devoid, transposable element-rich centromeres [27,43]. Combining this genomic hallmark of *Cryptococcus* centromeres [11,12,28,66–68] with synteny analysis, we assigned in silico each of the 14 centromeres of *C. neoformans* to a predicted centromeric region in *K. shandongensis*, a *Kwoniella* species with 14 fully assembled chromosomes (**S3 Fig**). This karyotypic similarity between *C. neoformans* and *K. shandongensis* supports the hypothesis that both lineages descended from a common ancestor with a 14-chromosome karyotype.

Karyotype reduction in *Kwoniella* occurred through recurrent chromosome–chromosome fusions across evolutionary timescales

To trace the sequence of chromosomal rearrangements that unfolded throughout *Kwoniella* evolution, synteny blocks were reconstructed with SynChro [69], employing *K. shandongensis* as reference. As detailed in **Fig 2**, karyotype reduction within *Kwoniella* occurred both
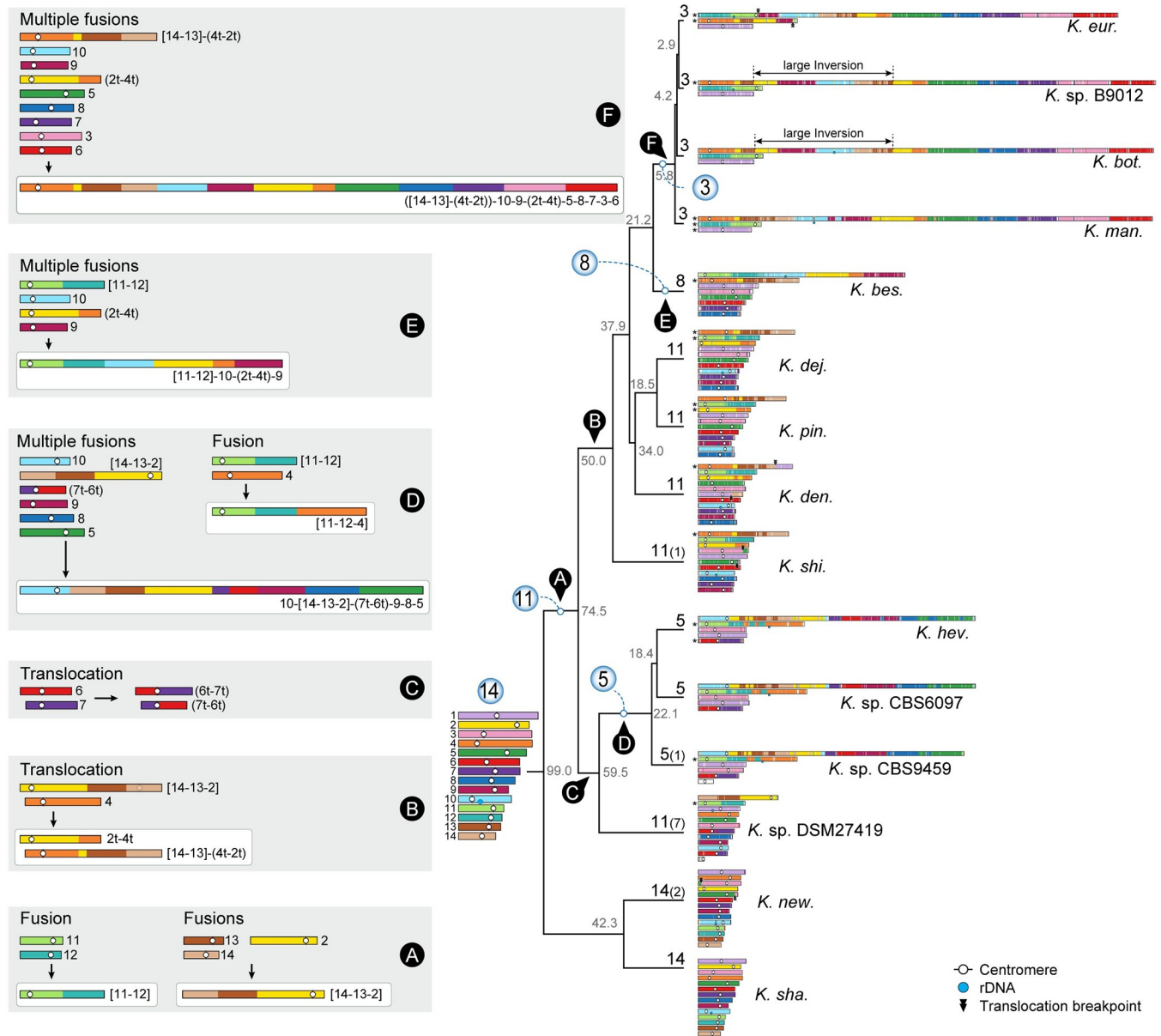
Fig 2. Karyotype reduction in *Kwoniella* occurred independently through recurrent chromosome fusions over evolutionary time. Major chromosomal rearrangement events, labeled from A to F, are illustrated along the evolution of *Kwoniella*. The karyotype of *K. shandongensis* (with 14 chromosomes) served as the reference for reconstructing synteny blocks in pairwise comparisons. The number of chromosomes in each species is depicted at the tips of the tree, with numbers in parentheses indicating additional small chromosomes lacking clear syntenic relationships with any other chromosome; these may constitute supernumerary, mini-chromosomes, or recently formed chromosomes. Only chromosomes above 100 kb are illustrated, with asterisks marking those inverted from their original assembly orientations. Numbers in gray around each internode represent median divergence time estimates in millions of years, obtained from Fig 1. Chromosomal fusions and translocations are labeled, respectively, within brackets or parentheses, based on their original IDs (e.g., "[11–12]" indicates a chromosome resulting from fusion of ancestral chrs. 11 and 12; "(7t-6t)" represents one of the chromosomes resulting from a reciprocal translocation between ancestral chrs. 6 and 7).

progressively and independently over time, primarily through chromosome fusions. We identified fusion events that have emerged more ancestrally, such as the fusion between chromosomes corresponding to *K. shandongensis* chrs. 11 and 12, occurring between 99 and 74.5 mya (event A in **Figs 2** and **S4A**), which is consistently seen as an individual chromosome in 8 of 13 species with fewer than 14 chromosomes. Another ancestral event combined chrs. 14, 13, and 2 (**S4B Fig**). The outcome of this fusion persists as a single chromosome (chr. 1) in *Kwoniella* sp. DSM27419 (**S4B Fig**), but in other species, this chromosome became more rearranged due to intrachromosomal rearrangements (as observed in *K. heveanensis* and closely related species) or underwent a translocation with another chromosome prior to diversification (event B in **Fig 2**). These fusion events led to the emergence of an 11-chromosome state in one of the lineages that branched off from the *Kwoniella* common ancestor and persisted in 4 extant *Kwoniella* species (*K. dejecticola*, *K. pini*, *K. dendrophila*, and *K. shivajii*). The other lineage, comprising *K. shandongensis* and *K. newhampshirensis*, retained the 14-chromosome karyotype.

More recent fusion events, between 59.5 to 5.8 mya, led to unique chromosomal arrangements in different lineages. In *K. heveanensis*, *Kwoniella* sp. CBS6097, and *Kwoniella* sp. CBS9459, our analysis suggests their common ancestor had a 5-chromosome karyotype. Specifically, chr. 2 emerged through fusion of the prefused chr. 11 to 12 with a chromosome corresponding to chr. 4 of *K. shandongensis* (event D in **Fig 2**), followed by species-specific intrachromosomal rearrangements, mainly inversions (**S4A Fig**). Likewise, chr. 1 seems to be the product of a past event where 6 chromosomes underwent fusion, generating an approximately 13-Mb chromosome (event D in **Figs 2**, and **S5**). Parallel events involving multiple chromosome fusions also took place in *K. bestiolae*, where a different set of 4 chromosomes fused together (event E in **Figs 2**, and **S6**). Yet, the most striking event, entailing the fusion of 9 chromosomes, is inferred to have occurred between 21.2 to 5.8 mya, in the shared ancestor of *K. europaea*, *Kwoniella* sp. B9012, *K. botswanensis*, and *K. mangrovensis*, leading to a 3-chromosome karyotype with an exceptionally large, approximately 18.2 Mb chromosome (event F in **Fig 2**). Postbranching from *K. mangrovensis*, this "giant" chromosome, which is 7 to 8 times larger than the other two, underwent structural changes, including a large inversion and a reciprocal translocation with chr. 2 in *K. europaea*, along with smaller, independent inversions in each species (**Fig 3A**). The data at hand does not allow, however, determining whether the 8 fusion events underlying the formation of the "giant" chromosome occurred in a single simultaneous step or through multiple consecutive events. This naturally formed "giant" chromosome is unusual and novel, particularly given its size, and its formation has clearly been tolerated despite some evidence suggesting that larger chromosomes may face additional challenges during mitotic segregation and replication [70].

Chromosome fusion events are associated with inversions between centromere- and telomere-proximal regions

To elucidate how these chromosomal fusion events occurred, all resulting junction sites were inspected. First, the possible presence of interstitial telomeric repeat sequences were examined near the fusion sites, as they could have been retained as remnants of past telomere-to-telomere fusion events [46]. However, no telomeric arrays, consisting of a minimum of 2 repeats of the telomeric motif TAAC(4,5), were detected beyond the chromosome ends.

Next, by aligning the giant chromosome of *K. mangrove*nsis with the individual chromosomes of *K. pini*, we unexpectedly found that at each fusion point, one side had sequences matching the end of one of the fused chromosomes, while the sequences on the other side aligned with an internal region of the other chromosome, rather than its end (illustrated in
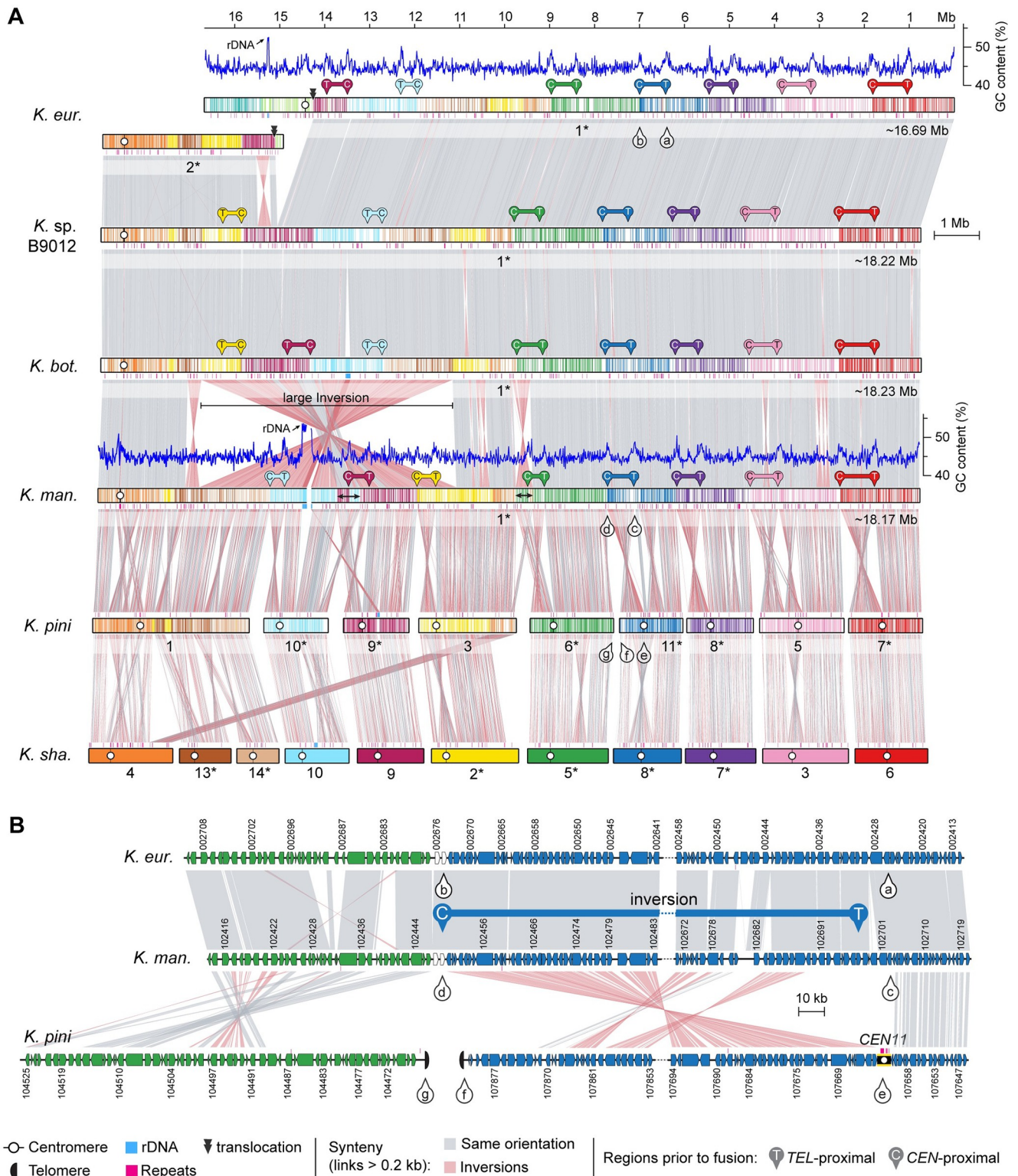
Fig 3. Giant chromosome formation in the ancestor of *K. mangrovensis* and sibling species resulted from multiple chromosome fusions events and inversions between centromere and telomere proximal regions. (A) Synteny comparison showing that the giant chromosome of *K. mangrovensis*, *K. botswanensis*, *Kwoniella* sp. B9012 and *K. europaea* (chr. 1) resulted from fusion of 9 chromosomes extant in *K. pini* (equivalent to 11 ancestral chromosomes). Note that the centromere-proximal regions of *K. pini* chromosomes correspond to regions near the fusion points on the giant chromosomes, whereas the telomere-proximal regions match more internalized regions, suggesting that a large pericentric inversion targeting the

centromere-adjacent region is associated with each fusion event. Small inversions in *K. mangrovensis* relocating the telomere- and centromere-proximal regions after fusion are marked by a double-sided black arrow, and a large inversion is predicted to have occurred after the split from *K. mangrovensis* but before divergence of the other 3 species. In *K. europaea*, the progenitor giant chromosome subsequently underwent a translocation with chr. 2. Chromosomes inverted relative to their original assembly orientations are marked with asterisks. **(B)** Zoomed-in synteny view of the genomic regions marked in panel A (pins with lowercase letters from a–g), shown as an example.

Fig 3B for *K. pini* chrs. 6 and 11). Further examination revealed that these internal sequences are chromosomal regions adjacent to in silico predicted centromeres (**Fig 3B**), suggesting that large inversions between telomere- and centromere-proximal regions are associated with centromere loss. This pattern, prevalent in most chromosomal fusion events contributing to the giant chromosome formation (**Fig 3A**), was also observed in fusion events across other *Kwoniella* species (**S4**–**S6** **Figs**), demonstrating a widespread occurrence. Predictably, this pattern is more discernable in more recent chromosome fusion events or when comparing chromosomes of closely related species. In a few instances, subsequent postfusion secondary inversions may have obscured this pattern (e.g., the fusion of chrs. chrs. 9-10 and 3-6 in the giant chromosome, **Fig 3A**; or the fusion at the origin of chr. 2 of *Kwoniella* sp. CBS9459, **S4A Fig**).

Kwoniella species have significantly shorter centromeres

The finding of extensive karyotypic variation in *Kwoniella*, along with large inversions involving centromeric regions associated with chromosome fusion events, led us to inspect (i) the conservation of kinetochore components essential for accurate chromosome segregation and (ii) experimentally validate in silico predicted centromeres in selected *Kwoniella* species with different chromosome numbers.

The centromere-specific histone H3 variant CENP-A, a key epigenetic marker for centromeres and kinetochore formation, previously characterized in *Cryptococcus* and other fungi [27,28,55,66,68,71–75], was confirmed to be conserved in both *Cryptococcus* and *Kwoniella* species, together with most outer kinetochore proteins such as those of the KMN (Knl1, Mis12, and Ndc80 complexes) network and Dam1/DASH complex (**S7 Fig** and **S2 Appendix**). Additionally, despite most inner kinetochore proteins being absent in the Agaricomycotina subphylum (to which *Cryptococcus* and *Kwoniella* belong), bridgin (Bgi1), which along with CENP-C connects outer kinetochore network to centromeric chromatin [76], was found in all species. Together, this indicates that machinery for accurate chromosomal segregation has been largely retained.

To characterize centromeres in *Kwoniella*, N-terminally mCherry-tagged CENP-A proteins were functionally expressed in *K. europaea* (3 chrs.), *K. bestiolae* (8 chrs.), and *K. pini* (11 chrs.). A genetic construct expressing the fusion protein from its native promoter was randomly inserted into each strain via biolistic transformation. Live cell imaging showed the mCherry-tagged proteins exhibit centromere localization patterns consistent with those reported in *Cryptococcus* species (**S7C Fig**) [27,66], indicating that the mCherry-CENP-A alleles are functional. We also attempted to express these constructs in *K. shandongensis* (with 14 chrs.) but were unsuccessful in obtaining transformants. To identify functional centromeres, we performed CENP-A chromatin immunoprecipitation sequencing (ChIP-seq). Because *C. neoformans* and *C. deuterogattii* centromeric regions are also enriched for other epigenetic marks, including 5-methylcytosine (5mC) DNA methylation, and heterochromatic histone modification H3K9me2 [66–68,77,78], ChIP-seq with an antibody specific to H3K9me2 and whole-genome bisulfite-sequencing (WGBS) were also conducted.

A single CENP-A bound region was significantly enriched on each of the chromosomes of the 3 *Kwoniella* species (**Figs 4** and **S8**-**S10**), matching the centromeric regions initially

predicted by synteny analysis, thereby validating our in silico approach. All centromeres also exhibited enrichment for H3K9me2, but the presence of 5mC was less consistent; e.g., high levels of 5mC were detected across all centromeres of *K. europaea* (**S8 Fig**), but only on *CEN3*, *CEN4*, and *CEN7* of *K. bestiolae* (**S9 Fig**). In *K. pini*, 5mC was absent from all centromeres, despite being present in a few other genomic regions (**S10 Fig**). Notably, this variation was not strictly correlated with the presence/absence of transposable elements (TEs) as *K. pini* centromeres still retain some TE remnants (**S10 Fig**). Building on recent research [77], we have also determined that all *Kwoniella* species possess both de novo and maintenance-type DNA methyltransferases (Dnmt5 and DnmtX) for cytosine DNA methylation, unlike all *Cryptococcus* species, including *Cryptococcus* sp. OR918 representing the earliest-branching lineage of this group, which only retained Dnmt5, and *C. depauperatus* that has specifically lost both proteins (**S11 Fig** and **S2 Appendix**). An independent loss event of DnmtX is also noted in the outgroup species, *Bullera alba* (**S11 Fig**). Considering all of the evidence, we conclude that the genomic regions identified in *Kwoniella* serve as binding sites for the centromeric histone CENP-A, affirming their role as bona fide centromeres.

As established in *C. neoformans*, *C. deneoformans*, *C. deuterogattii*, and *C. amylolentus* [27,66,68] and here demonstrated for 3 *Kwoniella* species, the lengths of the CENP-A-bound regions largely coincide with the ORF-free regions predicted to be centromeres. As such, the distance between centromere-flanking genes was leveraged as a metric to quantify centromere length across species. This analysis revealed significantly shorter centromeres in *Kwoniella* compared to *Cryptococcus* ($P < 0.0001$, Mann–Whitney U Test), with *Kwoniella* centromeres averaging 6.7 kb in median length (mean 8.3 kb) versus *Cryptococcus* centromeres that have a median length of 32.9 kb (mean 40.3 kb) (**Fig 5A** and **S1 Appendix**).

Kwoniella centromeres show significantly fewer TEs, consistent with a reduced genomic TE load

Although centromere identity and function are typically defined by CENP-A binding rather than by specific DNA sequences, repetitive sequences, such as TEs, are frequently observed in the centromeres of plants, animals, and fungi [79–81]. As established in previous studies, *Cryptococcus* species exhibit large regional centromeres that are enriched in specific long-terminal-repeat retrotransposons (LTRs) from the Ty3/*Gypsy* and Ty1/*copia* families [27,28,66]. It is thus not surprising that a genome-wide comparative analysis of repetitive elements revealed a significantly higher prevalence of TEs in *Cryptococcus* species ($P < 0.0001$, Mann–Whitney U Test), accounting for approximately 0.9% to 7% of the genome (median 2.7%), compared to *Kwoniella* species, which exhibit substantially lower TE content, ranging from 0.02% to 1.3% (median 0.2%) (**Fig 5B** and **5D**). Among the pathogenic *Cryptococcus* clade, *C. neoformans* and *C. deneoformans* are the 2 species situated at the higher end of transposon density (estimated at approximately 5.7% and 5.6%, respectively) while *C. deuterogattii* represents the lower end (approximately 1.5%). No substantial differences in transposon load were found between pathogenic and nonpathogenic *Cryptococcus* species (**Fig 5E**; $P = 0.95$, Mann–Whitney U Test).

Interestingly, while we found a significant negative correlation between TE content and genome size in this group of species (**Fig 5F**), indicating that the dynamics influencing genome size involves factors beyond TE content alone, a strong positive correlation was detected between TE content and the average length of centromeres ($\rho = 0.82$, $P < 0.0001$; **Fig 5G**), with most LTRs being located within the predicted centromeric regions in both genera (**Fig 5C**). However, *K. dendrophila* deviates from this pattern; this species exhibits low TE density genome-wide, and the predicted centromeres are devoid of LTRs and 5mC DNA methylation,
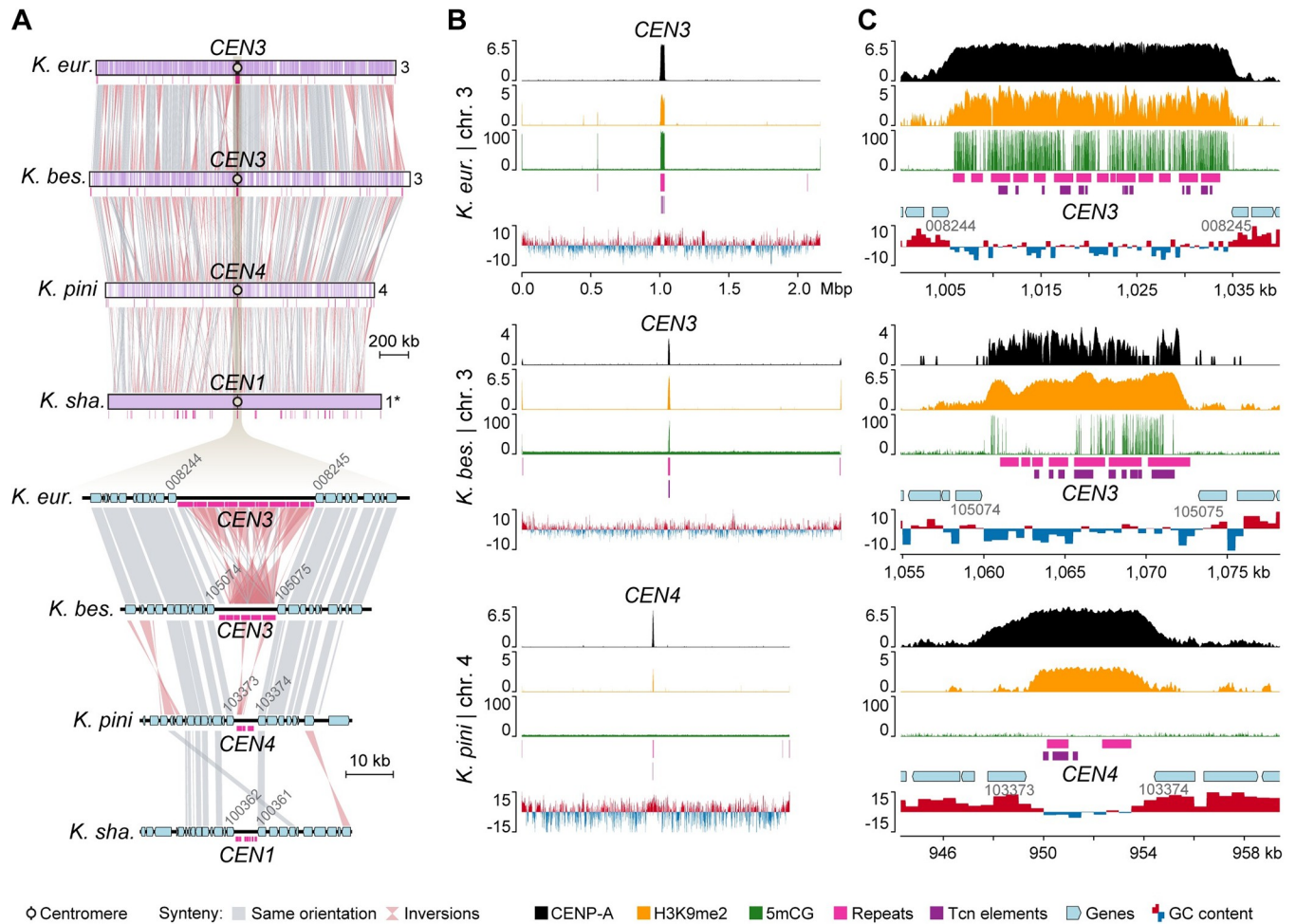
Fig 4. Experimental validation of *Kwoniella* centromeres in 3 species with different numbers of chromosomes. (A) Gene synteny conservation spanning a predicted centromeric region in 4 *Kwoniella* species (*CEN3* of *K. europaea*, *CEN3* of *K. bestiolae*, *CEN4* of *K. pini*, and *CEN1* of *K. shandongensis*). **(B)** Plots of the chromosomes depicted in panel A (except for *K. shandongensis*) displaying CENP-A (black) and H3K9me2 (orange) enrichment, fraction of CG cytosine DNA methylation (5mCG, green), repeat content (pink), Tcn-like LTR elements (purple), and GC content (shown as deviation from the genome average—red, above; blue, below). The fold enrichment of each sample over the input DNA is shown on the left of each panel for CENP-A and H3K9me2. **(C)** Zoomed-in sections show the regions spanning the centromeres with adjacent genes (light blue). In panels B and C, data are computed in 5-kb nonoverlapping windows.

while still exhibiting enrichment for H3K9me2 (**S12 Fig**). Additional exceptions were detected in *K. shandongensis* and *K. newhampshirensis*, as in these species, remnants of LTRs are only present in a subset of the predicted centromeres, along with other unclassified repeat elements (**S13 Fig**). These findings highlight the complex and diverse nature of centromere structures, emphasizing significant genetic and epigenetic characteristics of these critical chromosomal regions, even among closely related species.

Shorter centromeres in *Kwoniella* do not appear to be a result of RNAi loss

Previous studies in *C. neoformans* and *C. deneoformans* identified centromeres as primary sources for production of small-interfering RNA (siRNA) for transposon silencing via the RNA interference (RNAi) pathway [66], with these species retaining the canonical RNAi components: Argonaute (Ago), Dicer (Dcr), and RNA-dependent RNA polymerase (Rdp) [82,83]. In contrast, the RNAi-deficient species *C. deuterogattii* has lost many RNAi components [84]
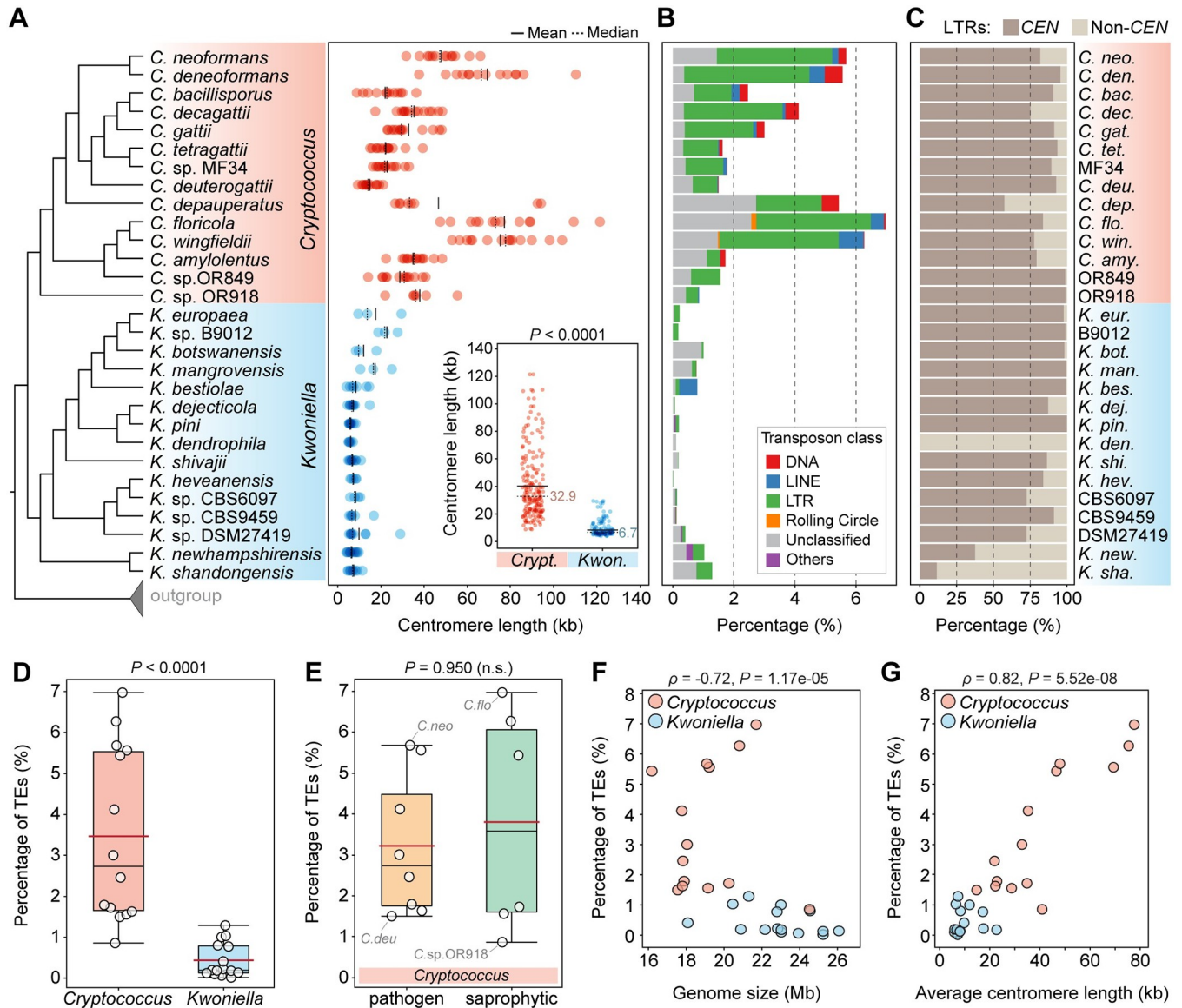
Fig 5. Centromere length and TE content in *Cryptococcus* and *Kwoniella*. (A) Comparison of estimated centromere lengths (in kb) along the phylogeny of *Cryptococcus* and *Kwoniella* species. Each dot represents a single centromere, and solid and dashed black lines represent mean and median lengths, respectively. A comparison between the 2 genera is summarized in the inset, showing significantly smaller centromeres in *Kwoniella* compared to the *Cryptococcus* lineage (*P* value obtained by Mann–Whitney U Test). **(B)** Estimated TE content within each genome. **(C)** Relative percentage of LTR retrotransposons found in centromeric (*CEN*) versus non-centromeric (non-*CEN*) regions (normalized by the total percentage of LTRs). **(D, E)** Box plots comparing TE content between *Cryptococcus* and *Kwoniella*, and between pathogenic and nonpathogenic *Cryptococcus* species (*P* values obtained by Mann–Whitney U Test; n.s., not significant). The red line, black line, and boxes denote the mean value, median value, and interquartile range, respectively. **(F, G)** Correlations between TE abundance with genome size **(F)** and average centromere length **(G)**. Spearman's correlation coefficients (*ρ*) indicate the strength and direction of these relationships. The data underlying this Figure can be found in **S6 Appendix** and at https://doi.org/10.5281/zenodo.11199354.

https://doi.org/10.1371/journal.pbio.3002682.g005

and harbors shortened centromeres containing only LTR remnants [66]. This led us to question whether the comparatively shorter centromeres in *Kwoniella* could be due to a lack of active RNAi.

To address this, we conducted an in-depth analysis of the key RNAi genes across *Cryptococcus* and *Kwoniella*, which revealed that the common ancestor of the 2 lineages likely had a functional RNAi pathway, with 2 Ago proteins (Ago1 and Ago4), 1 Dicer (Dcr1), and 1 RNA-

dependent RNA polymerase (Rdp1) (**S14 Fig**). Additionally, we uncovered a complex pattern of gene duplication and loss across lineages (refer to **S1 Text** for details), yet, excluding *C. deuterogattii*, all species seem to be RNAi-proficient based on the presence of canonical RNAi genes (**S14 Fig**). Beyond the core components of the RNAi-pathway, we also examined 8 additional genes (*ZNF3 GWC1*, *QIP1*, and *RDE1* to *RDE5*) essential for global siRNA production in *C. neoformans* [84–86] (**S1 Text** and **S2 Appendix**). While most genes were consistently conserved, *ZNF3* (CNAG_02700) was an exception, having been lost independently 3 times in *Cryptococcus* (**S1 Text**, **S15 Fig**, and **S2 Appendix**). In *Kwoniella*, Znf3 proteins are shorter but retain essential zinc finger domains, suggesting potential functionality (**S1 Text**, **S15 Fig**, and **S2 Appendix**). These findings suggest that *Kwoniella* retains both canonical and auxiliary RNAi components, pointing to an active RNAi pathway. Thus, the shorter centromeres in *Kwoniella* likely result from factors other than RNAi pathway deficiencies, underscoring the need for further research into factors influencing centromere length.

Identification of mini-chromosomes in *Kwoniella*

Our genomic analyses detected unusually small chromosomes (<100 kb) in some *Kwoniella* species, which we termed "mini-chromosomes." Specifically, 6 mini-chromosomes were identified in *Kwoniella* sp. DSM27419 (ranging from approximately 43.7 to 83 kb), 2 in *K. newhampshirensis* (approximately 39 kb each), and 1 in *K. shivajii* (approximately 87.6 kb). This was substantiated by PFGE and read coverage analyses from both Illumina and long-read sequencing, along with the identification of telomeric repeats at both ends of each mini-chromosome (**S16A and S16B Fig**). Compared to regular chromosomes, these mini-chromosomes have a lower gene density and reduced GC content (**S16C–S16H Fig**). Interestingly, *Kwoniella* sp. DSM27419 has an extra chromosome (chr. 12) approximately 228 kb in size, and *Kwoniella* sp. CBS9459 also features a smaller chromosome (chr. 6) approximately 745 kb. Both chromosomes show no synteny with other *Kwoniella* chromosomes (**Figs 2** and **S16F**), leaving their origin and function currently unclear and subject to further investigation.

Chromosome number reduction in *Cryptococcus* via centromere inactivation and transposon loss

Unlike the broad spectrum of chromosome numbers in *Kwoniella*, *Cryptococcus* species maintain a more uniform chromosome number, with only 2 species having fewer than 14 chromosomes (*C. depauperatus* and *Cryptococcus* sp. OR918, **Fig 1B**). To investigate if chromosome number reduction in *Cryptococcus* follows mechanisms similar to those identified in *Kwoniella* (chromosome fusions with pericentric inversions), we focused on comparisons between *C. depauperatus* (8 chromosomes), and 2 other *Cryptococcus* species, *C. neoformans* and *C. amylolentus* (each with 14 chromosomes).

Synteny analysis revealed substantial interchromosomal rearrangements in these species after diverging from their last common ancestor (**Fig 6A**). Analysis of the centromere-flanking regions indicates that *C. depauperatus* centromeres have served as frequent target sites for chromosomal arm exchanges through intercentromeric recombination, similar to *C. neoformans* and *C. amylolentus* [27,66]. However, whereas only 3 centromere-mediated translocations are estimated since the last shared ancestor of *C. neoformans* and *C. amylolentus*, in *C. depauperatus*, 7 out of 8 extant centromeres appear to be products of repeated intercentromeric recombination (**Fig 6B**).

Synteny analysis also suggests that the reduction from 14 to 8 chromosomes in *C. depauperatus* did not result from sequential chromosome fusions as in *Kwoniella*. This chromosome number reduction involved inactivating or losing 6 centromeres. We traced the fate of 4 of

Fig 6. Chromosome number reduction in *Cryptococcus* involves centromere inactivation via loss of LTR-rich regions. (A) Pairwise synteny relationships between *C. depauperatus* (8 chromosomes), and *C. neoformans* and *C. amylolentus* (14 chromosomes each). Links represent the boundaries of syntenic gene blocks identified by MCScanX with pairwise homologous relationships determined by SynChro. Chromosomes are color-coded per *C. neoformans* and were reordered or inverted (marked with asterisks) from their original assembly orientations to maximize collinearity. **(B)** Overlay of synteny blocks and centromere locations, underscoring several intercentromeric rearrangements between *C. neoformans* and the other species. Red

arrowheads pinpoint predicted inactivated centromeric regions. (**C-E**) Linear chromosome plots depicting gene synteny conservation between *C. depauperatus* (*Cd*), *C. neoformans* (*Cn*), and *C. amylolentus* (*Ca*) chromosomes in regions corresponding to inactivated *CEN4* (i*CEN4*), i*CEN8*, and i*CEN7* in *C. depauperatus*, respectively.

these centromeres, aligning with *CEN4*, *CEN5*, *CEN7*, and *CEN8* of *C. neoformans*, with reasonable accuracy (**Fig 6B**). The other two, linked to recombined *CEN6*/*CEN9* and *CEN12* in *C. neoformans*, seem to have been lost due to additional rearrangements. Our previous work reported that the inactivation of the centromere in *C. depauperatus*, aligning with *CEN5* in *C. neoformans* (or *CEN10*/*CEN4* in *C. amylolentus*), likely resulted from gross chromosomal rearrangements linked to the complex evolution of the mating-type locus [11]. Consequently, we focused on losses in *C. depauperatus* corresponding to *CEN4*, *CEN7*, and *CEN8* of *C. neoformans*.

Examination of the gene content in *C. depauperatus* that aligns with *C. neoformans CEN4* suggests that inactivation of this centromere might have resulted from intercentromeric recombination followed by loss of the LTR-rich region. This is supported by the gene organization in C. *depauperatus*, which aligns well with a juxtaposition of the genes flanking the opposite sides of *CEN4* and *CEN6* in *C. neoformans* (**Fig 6C**). Similarly, inactivation of *CEN7* and *CEN8* appears to be associated with the removal of their LTR-rich regions, without major loss of flanking genes or rearrangements (**Fig 6D** and **6E**). Notably, the *C. depauperatus* region corresponding to inactivated *CEN7* still contains TE remnants, suggesting it may represent a more recently inactivated centromere. These findings collectively indicate that reduction in chromosome number in *Cryptococcus* resulted from chromosomal rearrangements other than full-chromosome fusions, and centromere loss is primarily attributable to excisions of centromeric DNA sequences.

Surveying genomic signatures of karyotypic variation

In light of the marked karyotypic differences between *Cryptococcus* and *Kwoniella*, along with the unique chromosome dynamics in the *Kwoniella* clade, we leveraged our high-resolution genome assemblies to identify potential variations in gene families related to telomere length maintenance and protection (shelterin complex). To examine gene conservation, orthologs were identified across 32 genomes (14 *Cryptococcus*, 15 *Kwoniella*, and 3 outgroup species) (**Fig 7**). A total of 4,756 orthogroups (OGs) were found in all the *Cryptococcus* and *Kwoniella* genomes. Key telomere-length regulation proteins such as Tel2, Tel1, Tert, and Blm helicase were conserved across species (**S2 Appendix**). However, except for *POT1*, *TPP1*, and a *TEN1*-like gene, no other clear shelterin complex orthologs were found (see **S2 Text** for details and **S2 Appendix**). This suggests either that other shelterin components are absent or that other proteins fulfilling these roles have evolved, in line with the reported diversity of fungal shelterin proteins [87–89]. Additionally, the analysis of 152 genes known to impact telomere length [90,91] in the budding yeast *Saccharomyces cerevisiae* also showed a high degree of conservation (**S2 Appendix**), with an average of approximately 82% of these genes present across species. Significantly, species with "giant" chromosomes showed a similar conservation rate, highlighting the lack of major gene composition differences across species with varied chromosome numbers (**S2 Text** and **S2 Appendix**).

To examine more closely if differences in selection may have contributed to, or resulted from, karyotypic variation, we carried out a branch selection analysis. We compared the evolutionary patterns of orthologous genes in 4 *Kwoniella* species with 3 chromosomes (foreground branch) to a sister clade of 4 species with 8 to 11 chromosomes (background branch). Genes in the foreground clade with higher dN/dS ratios compared to the background clade indicate a
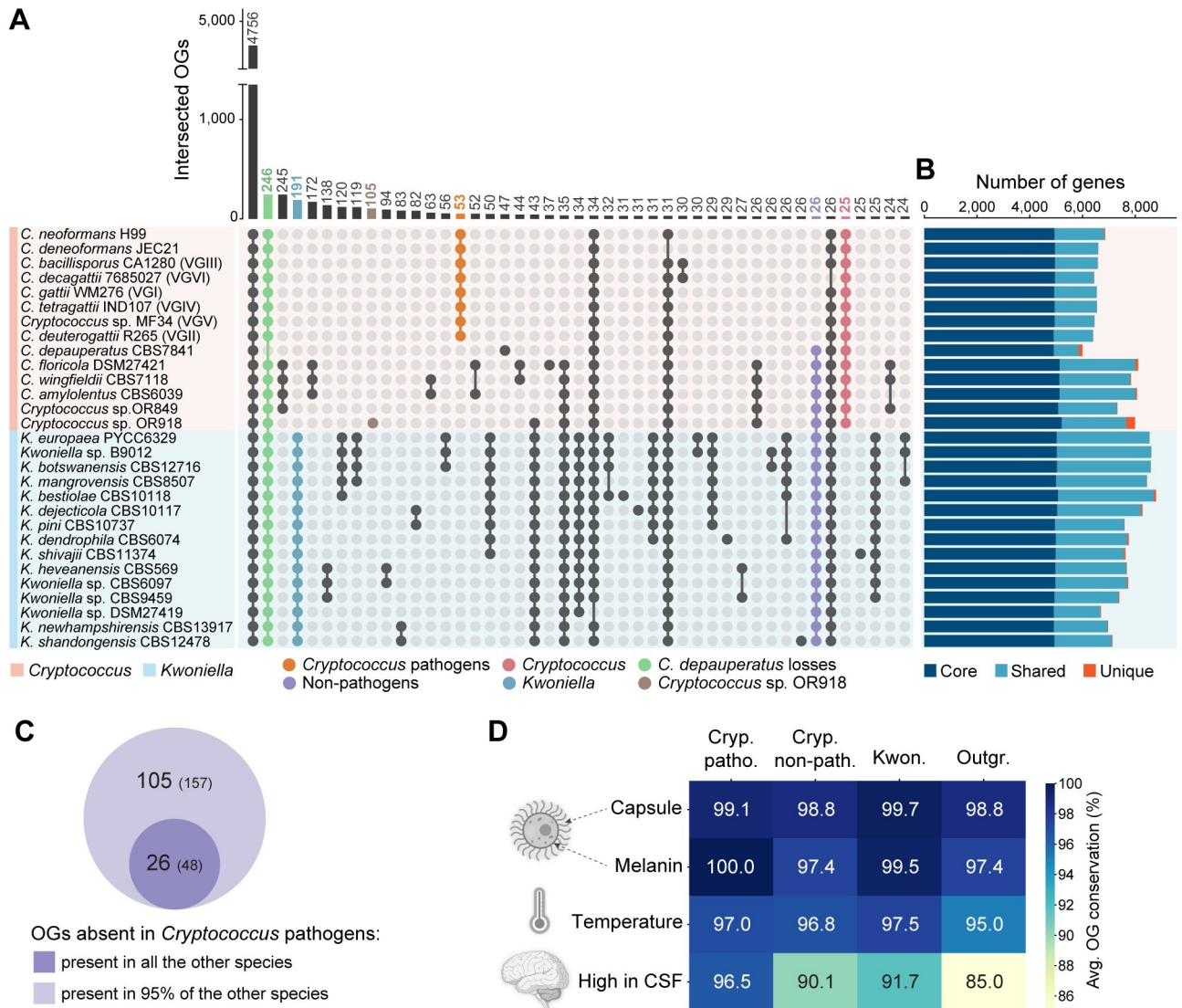
Fig 7. Gene family analysis in *Cryptococcus* and *Kwoniella*. (A) UpSet plot displaying protein family overlaps between *Cryptococcus* and *Kwoniella*. The numbers of protein families (OGs) defined by OrthoFinder are indicated for each species intersection, with key intersections emphasized as per the accompanying key. (B) Bar plot categorizing orthology classes into core genes (found in all genomes; dark blue), shared genes (present in multiple but not all genomes; light blue), and unique genes (present within species-specific OGs; dark orange). (C) Venn diagram comparing OGs absent in all pathogenic *Cryptococcus* species but present in all or 95% of nonpathogenic *Cryptococcus* and *Kwoniella* species. (D) Heatmap depicting the average conservation rate in *Cryptococcus* pathogens, nonpathogenic *Cryptococcus*, *Kwoniella*, and outgroup species, of OGs identified in *C. neoformans* known to be involved in capsule and melanin production, growth at 37°C, and high expression in human cerebrospinal fluid (CSF). Created using clipart from BioRender (https://www.biorender.com/) with permission. The data underlying this Figure can be found in **S4** and **S5 Appendices** and at https://doi.org/10.5281/zenodo.11199354.

https://doi.org/10.1371/journal.pbio.3002682.g007

greater degree of selection. Top scoring genes included those associated with cell structure, ribosomal functions, and DNA modification or repair (**S3 Appendix**). Two genes related to centromere function in the top 30 corresponded to *C. neoformans* CNAG_02218, a putative homolog of *SCM3* (suppressor of chromosome missegregation) [92,93] and CNAG_01334, an ortholog of *S. cerevisiae SLI15*, encoding a subunit of the Chromosomal Passenger Complex (CPC) that regulates kinetochore–microtubule interactions and is important for chromosome segregation [94,95]. These findings may suggest a model in which instability in chromosome segregation could be a driving event in karyotype instability.

Gene family losses in pathogenic and nonpathogenic *Cryptococcus* species

Complete genomes sequences of *Cryptococcus* and *Kwoniella* species also provide a new window into the evolution of their gene content. Beyond the 4,756 shared OGs between both groups, the next most frequent pattern is the specific absence of 246 OGs in *C. depauperatus*, which has the smallest gene set (**Figs 7 and S1, S1** and **S4 Appendices**). This substantial gene loss in *C. depauperatus* is aligned with its reduced genome size (**Figs 1** and **S1** and **S1 Appendix**) and possibly associated with loss of yeast phase growth [11]. Notable gene losses include major facilitator superfamily proteins, glycosyl hydrolase family 3 proteins, and DNA-interacting proteins, such as Msh4 and Msh5 mismatch repair proteins, and the Rad8 DNA repair protein. Also missing are genes encoding uracil/uridine permeases (CNAG_04632 and CNAG_07917) (**S4 Appendix**), aligning with our own experimental observations that no 5-FOA resistant mutants could be isolated [11], suggesting an inability of *ura5* mutants to import uracil or uridine to compensate for auxotrophy.

In analyzing genes absent in all pathogens yet present in all nonpathogens, we identified 26 OGs, corresponding to 48 genes in nonpathogenic *C. floricola*. These genes displayed diverse enzymatic activities, including a large set of short chain dehydrogenase/reductases and amino acid permeases (**Fig 7A** and **7C** and **S4 Appendix**). Recognizing that some gene losses in pathogens might also sporadically occur in nonpathogens due to environmental adaptations or specific organismal interactions, we refined our criteria to include genes absent in all pathogens but present in at least 95% of nonpathogens. This adjustment resulted in identifying 79 additional OGs (109 genes in *C. floricola*) (**Fig 7C**). Among these, 2 genes, *PRA1* and *ZRT1*, stand out for their roles in zinc acquisition in *C. albicans*. Pra1, a zincophore [96], and Zrt1, a zinc transporter [97], are adjacent and divergently transcribed, and this arrangement was found to predate the Basidiomycota–Ascomycota split, with *PRA1* having subsequently experienced multiple losses across fungal clades [98,99]. Loss of *PRA1* in certain species was recently suggested as a possible evolutionary step for fungal pathogenesis [100], offering a strategic advantage by reducing fungal visibility to immune systems that have evolved to recognize and target this protein, thereby decreasing the likelihood of fungal detection and elimination by host defenses [100]. Previously, the absence of the *PRA1/ZRT1* cluster was noted in some pathogenic *Cryptococcus* species, contrasting with 6 nonpathogenic species surveyed that retain it [97]. We have now broadened this analysis by confirming the absence of this gene cluster in all pathogenic *Cryptococcus* species, and its presence in most, though not all, nonpathogenic *Cryptococcus* and *Kwoniella* species (**S16A Fig**). Exceptions include *Cryptococcus* sp. OR849 and *K. newhampshirensis*, which have recently lost the cluster as inferred from synteny analysis (**S16A, S16F, and S16G Fig**). Additionally, *Cryptococcus* sp. OR918 and most (13 of 15) *Kwoniella* species possess a second *PRA1* variant (*PRA1-2*) with significant sequence differences and no adjacent zinc transporter (**S16B and S16C Fig**). The consistent loss of the *PRA1/ZRT1* gene cluster in pathogenic species, along with its selective loss in nonpathogens, underscores its potential significance in fungal pathogen evolution, warranting further investigation. Specifically, the loss of this cluster in nonpathogenic species, likely driven by evolutionary pressures unrelated to host interactions, could incidentally equip these fungi with traits advantageous in hostile host environments, potentially representing an example of preadaptation that facilitates transition to an opportunistic pathogenic lifestyle.

Gene families in pathogenic *Cryptococcus*

Among the genes specifically present in the *Cryptococcus* pathogens (53 OGs, corresponding 57 *C. neoformans* genes), there is a large group predicted to interact with DNA, including 6 predicted transcription factors or DNA binding proteins (**S4 Appendix**) and 2 of the 4 genes

annotated as B-glucuronidases (PFAM glycosyl hydrolase family 79C), implicated in cell wall modification [101]. As strong signatures of pathogenesis were not detected in this analysis, the conservation of genes associated with the canonical features of cryptococcal pathogenesis were evaluated. Genes associated with capsule biosynthesis [102,103], melanin production [104–108], and ability to grow at 37 degrees [109] were all found to be highly conserved across all species (**Fig 7D** and **S5 Appendix**). Only a gene set identified as highly expressed in human cerebrospinal fluid (CSF) across diverse *C. neoformans* strains [110] was found to be less conserved in nonpathogenic *Cryptococcus*, *Kwoniella*, and the outgroup species (**Fig 7D** and **S5 Appendix**).

Gene family analysis also found an exclusive gene in pathogenic *Cryptococcus*, residing approximately 82 kb from the right end of chr. 1 in *C. neoformans* H99, predicted to encode a D-lactate dehydrogenase, expressed under various conditions (see CNAG_00832 in FungiDB) (**Fig 8**). Surprisingly, BLAST analysis shows its closest homologs are *Aspergillus* proteins with about 87% identity, indicating possible horizontal gene transfer (HGT) from these ascomycetous molds. Investigating further, we used the CNAG_00832 protein sequence to search the NCBI clustered nr database and conducted phylogenetic analysis of the top 1,000 hits. The resulting tree (**Fig 8A**) places *Cryptococcus* proteins within the genus *Aspergillus* (**Fig 8B**), while also suggesting a more ancient bacterial origin for this fungal D-lactate dehydrogenase. In line with this, AlphaFold 3D structure predictions following pairwise structure alignments
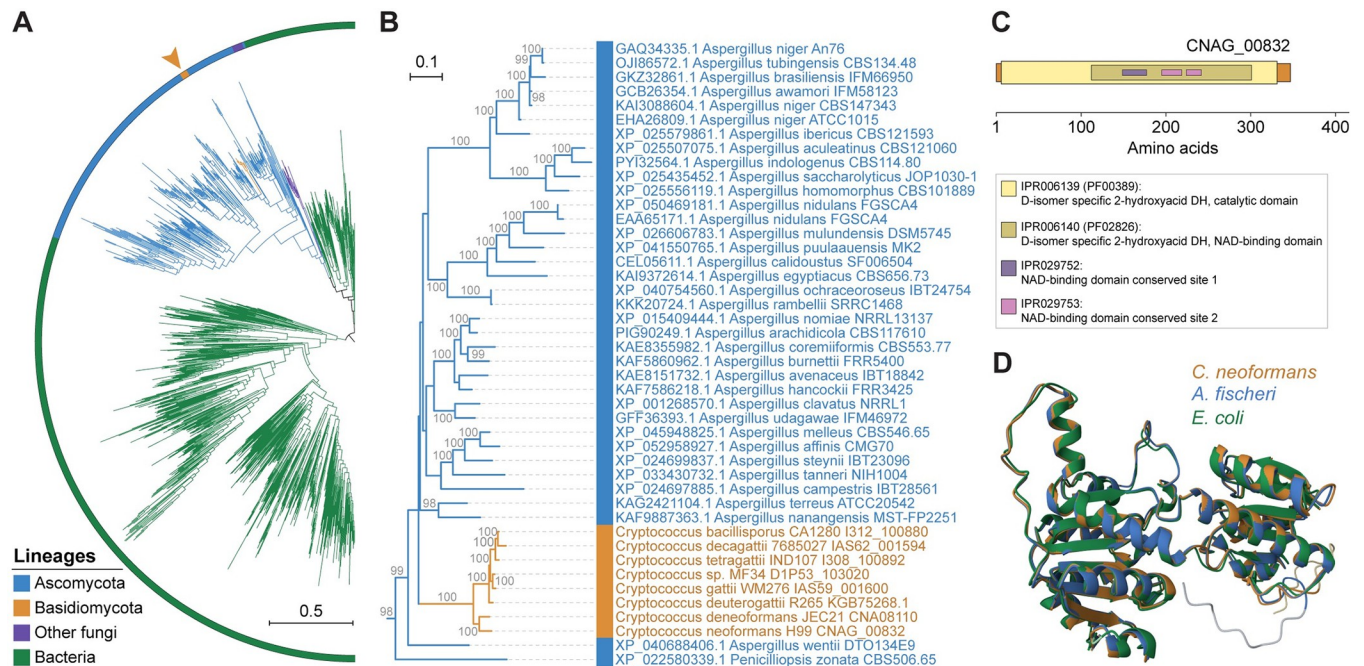
Fig 8. Horizontal gene transfer and the origin of a putative D-lactate dehydrogenase specific to pathogenic *Cryptococcus* species. (**A**) Maximum likelihood (ML) phylogeny encompassing 1,007 protein sequences obtained from a BLASTP search against the NCBI clustered nr database, using the *C. neoformans* CNAG_00832 protein sequence as query and selecting the top 1,000 hits. The identified sequences in pathogenic *Cryptococcus* species were also included. Tree branches are colored as per the key, depicting major groups of organisms. The tree, visualized with iTOL v6, was constructed with IQ-TREE2, with internal branch support assessed by 10,000 replicates of Shimodaira–Hasegawa approximate likelihood ratio test (SH-aLRT) and ultrafast bootstrap (UFboot), and is rooted at the midpoint. Branch lengths are given in number of substitutions per site. (**B**) Pruned ML phylogeny showing the position of *Cryptococcus* proteins clustering within the presumed Aspergilli donor lineage. (**C**) Domain organization of the protein sequence encoded by CNAG_00832 with identified InterPro (IPR) and Pfam (PF) domains highlighted. (**D**) Overlay of AlphaFold predicted structures of D-lactate dehydrogenase proteins from *C. neoformans* (UniProt J9VFV7), *Aspergillus fischeri* (UniProt A1D163), and *Escherichia coli* (UniProt P52643) showing structural similarity. Pairwise structure alignments were performed and visualized in the Protein Data Bank (PDB) website (https://www.rcsb.org/alignment) using the JjFATCAT-rigid algorithm. The phylogenetic tree file is provided at https://doi.org/10.5281/zenodo.11199354.

https://doi.org/10.1371/journal.pbio.3002682.g008

revealed similar structures among 3 representative sequences of each of the 3 lineages (**Figs 8D** and **S18**). This structural congruence reinforces the notion of a complex HGT event, where an initial bacterial gene was likely acquired by an ascomycetous fungus and later transferred to *Cryptococcus*. The precise function of this gene in *Cryptococcus* pathogens, particularly in interconverting D-lactate and pyruvate, along with the reduction/oxidation of NAD+ and NADH, is the subject of ongoing work but could be important for *Cryptococcus* growth in glucose-limited environments like the brain during cryptococcal meningoencephalitis, potentially via gluconeogenesis [111].

Discussion

Our broad comparative genomics analysis of *Cryptococcus* and *Kwoniella* has uncovered extensive karyotypic variation, particularly within *Kwoniella*, and significant gene content conservation in pathogenic and nonpathogenic species. Our findings support a nonpathogenic common ancestor, with pathogenic traits evolving more recently in *Cryptococcus*. While pathogenic *Cryptococcus* species display distinct phenotypic traits, including higher temperature tolerance and melanin and capsule virulence factors [10], genes responsible for these characteristics are largely conserved across all species. This suggests that gene sets enabling adaptation to diverse environmental niches might predispose certain species to develop pathogenicity in humans. Echoing the minimal gene content differences between humans and great apes [112], our study indicates that differences in pathogenic *Cryptococcus* species may stem from finer scale gene variation or differential genetic and epigenetic regulation, rather than major changes in gene content. While it seems plausible that shared traits underlie emergence of pathogenic species, it is also likely that finer differences will emerge within the pathogens given that some species (*C. neoformans*, *C. deneoformans*, *C. bacillisporus*, and *C. tetragattii*) predominantly infect HIV/AIDS patients, whereas others (*C. gattii* and *C. deuterogattii*) infect largely non-HIV/AIDS patients, such as those with autoantibodies to the cytokine GM-CSF [113–116]. Understanding these differences will require incorporating further population, transcriptomic, epigenetic, and functional data.

The notable plasticity of fungal genomes, particularly evident in *Cryptococcus* species, is highlighted by a variety of mechanisms and processes that drive genetic variation (such as hybridization [117–119], ploidy variation [120,121], transposon mobilization [122,123], gene loss [124], and gene gain via duplication [125] or horizontal gene transfer [126]) and also by diverse reproductive strategies (e.g., [127]). Our analysis found a few, but likely significant gene losses, especially within *Cryptococcus*. First, we expanded the previously reported loss in *Cryptococcus* of a de novo methyltransferase (DnmtX) [77] involved in 5mC methylation, by identifying its absence in an earlier-derived *Cryptococcus* lineage (strain OR918). Contrastingly, DnmtX persists across *Kwoniella* species. Alongside the ubiquitous presence of a maintenance methyltransferase (Dnmt5) in both genera (with *C. depauperatus* as an exception, lacking both genes), this suggests the possibility of distinct DNA methylation landscapes in the 2 genera, potentially impacting gene regulation and TE control. Secondly, in examining the genetic network encoding RNAi components across the 2 genera, we uncovered a complex evolutionary history characterized by both ancestral and recent, species/clade-specific, gene duplications and losses (*AGO1/2/3/4*, *DCR1/2*, and *RDP1/2*). Besides *C. deuterogattii*, which uniquely lost multiple RNAi genes [84], these genes are otherwise retained in all other species, suggesting they have active RNAi pathways. This is of interest given the dramatic differences in centromere length between *Cryptococcus* and *Kwoniella*, and previous studies associating RNAi loss and centromere length contractions [66]. This may imply alternative mechanisms in *Kwoniella* for transposon control and centromere length regulation, as discussed further

below. Interestingly, *Kwoniella* has maintained a higher number of Ago genes since diverging from a shared ancestor with *Cryptococcus*, which might indicate redundancy or functional specialization as observed in other organisms [128,129]. The third example of gene loss is in the unusual species *C. depauperatus*, which lacks a yeast phase and grows exclusively as a hyphal organism engaged in continuous sexual reproduction [11]. This species has lost genes for uracil/uridine import and DNA repair, underscoring distinct evolution. Finally, our analysis broadens previous findings on the *PRA1/ZRT1* gene cluster, implicated in zinc acquisition and recently hypothesized as a key factor in fungal pathogen evolution [100]. We show this gene cluster was lost in all pathogenic *Cryptococcus* species yet present in most, but not all, nonpathogens. This dichotomy indicates potential evolutionary pathways that could have facilitated pathogenic trait development in *Cryptococcus*, aligning with the view that most human fungal pathogens are opportunistic and that the emergence of fungal pathogenesis is an outcome of intricate interactions between pathogens, hosts, and their environments [8].

Our analysis provides evidence that gene gain via HGT might have contributed to pathogenicity evolution in *Cryptococcus*. Specifically, we identified a gene encoding a putative D-lactate dehydrogenase that is unique to *Cryptococcus* pathogenic species and appears to have been acquired from the genus *Aspergillus*. While the function of this *Cryptococcus* gene is still under investigation, it could promote growth via gluconeogenesis during glucose deprivation (common during brain infections) [130,131]. This aligns with proposed hypotheses that lactate, a C_3 substrate, might be more favorable for biomass production in brain infection than C_2 substrates such as acetate [111]. Supporting this, the glyoxylate shunt pathway, which uses C_2 substrates, is not essential for *C. neoformans* virulence [132,133]. These findings could suggest that *Cryptococcus* pathogens may have a preexisting advantage in glucose-limited environments, such as the human brain. However, given that the *Cryptococcus* pathogenic group predates their interaction with humans, these traits might have stemmed from broader environmental pressures rather than solely due to human host interactions. Further studies of gene loss/gain, allied with comparative transcriptomic analyses under various conditions, will be needed to unravel other genetic and regulatory changes leading from nonpathogenicity to pathogenicity in these fungi.

Our extensive comparative genomic analysis also identified distinct karyotypic evolution in *Kwoniella* compared to *Cryptococcus*. In *Kwoniella*, chromosome fusion is the major driving force, occurring repeatedly and independently throughout the genus. Starting from an inferred ancestral chromosome number of 14, various extant *Kwoniella* species show reduced chromosome numbers—11, 8, 5, and as few as 3—due to successive chromosome fusions. At the extreme, these fusions have formed giant chromosomes, 15 to 18 Mb in size, which are up to 8 times larger than other extant chromosomes, comprising as much as 80% of the genome. Investigating what drove repeated chromosome–chromosome fusion events in *Kwoniella*, we observed that each fusion typically involves a pericentric inversion extending from one telomere to just beyond the centromere. As shown in **Fig 9**, these pericentric inversions may have occurred before (model A) or after chromosome fusion (model B).

Model A proposes an initial pericentric inversion shifting the centromere of one chromosome to the end, resulting in a telo- or acrocentric chromosome. This is followed by a symmetric reciprocal translocation with another chromosome, involving breakpoints near the centromere on the long arm of the telo- or acrocentric chromosome and near the end of the second chromosome. The resulting larger translocation product, combining most of both chromosomes, is retained, while the smaller product comprising the centromere of the telo- or acrocentric chromosome plus 2 telomeres, often devoid of essential genes, is lost due to unstable transmission. Supporting this model, no evidence was found for interstitial telomeric repeats sequences at any of the junctions, albeit such sequences are known to be unstable
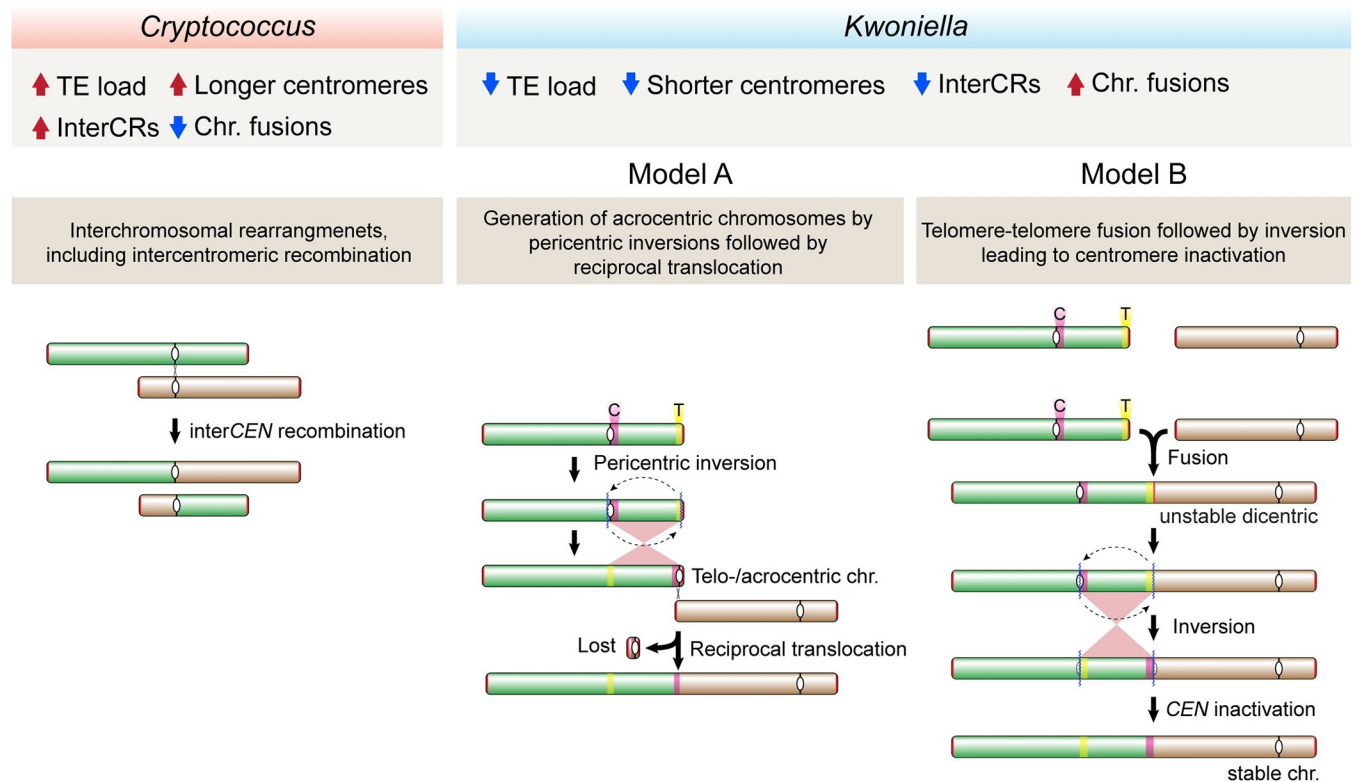
Fig 9. Proposed model of chromosome evolution in *Cryptococcus* and *Kwoniella*. The hypothesized mechanisms driving chromosome evolution in *Cryptococcus* and *Kwoniella* account for the distinct patterns of chromosomal rearrangements observed in these 2 groups. *Cryptococcus* (left) is characterized by frequent interchromosomal rearrangements, including intercentromeric recombination likely influenced by longer centromeres and higher TE content. *Kwoniella* (right), however, predominantly shows chromosome fusions, associated with lower TE content and shorter centromeres, and fewer interchromosomal rearrangements. Two mechanisms for chromosome fusions in *Kwoniella* are proposed: Model A, involving a pericentric inversion followed by a reciprocal translocation between chromosomes, typically resulting in the loss of the smaller translocation product; and Model B, based on "end-to-end fusion" leading to a dicentric chromosome that becomes monocentric through a pericentric inversion (see text for details).

https://doi.org/10.1371/journal.pbio.3002682.g009

[134], and might have decayed if initially present. Interestingly, some chromosome fusions described in *Arabidopsis* may have originated through a similar process [49].

A derived hypothesis for Model A, particularly considering the shorter centromeres in *Kwoniella* compared to *Cryptococcus*, is the potential loss of centromere function due to telomeric silencing or DNA sequence erosion resulting from pericentric inversion. In this context, a possible outcome following the pericentric inversion could be the restoration of viability through chromosomal fusion. This hypothesis aligns with findings in *C. deuterogattii*, where centromere deletion led to both neocentromere formation (without karyotype change) and chromosome fusion, reducing the karyotype from 14 to 13 chromosomes [68]. Interestingly, in this case, no interstitial telomeric sequences were found at the junctions, which points towards microhomology-mediated end joining (MMEJ) as the likely fusion mechanism [68]. Thus, events impairing centromere function may have driven chromosome fusion in *Kwoniella*.

Model B, on the other hand, proposes an "end-to-end fusion" hypothesis, possibly in cells with dysfunctional or critically shortened telomeres, engaging in nonhomologous end joining. This process potentially results in an unstable dicentric chromosome, which may be stabilized into a monocentric chromosome through an inversion targeting one of the centromeres (leading to its inactivation) and the initial fusion point (potentially a fragile site). This contrasts with telomere–telomere style chromosome fusion events observed in other species, such as the

formation of chromosome 2 in humans [46], the fusion events leading to the 4-chromosome karyotype in *F. graminearum* [52], and similar events during laboratory crosses in *C. deneoformans* [135].

In both models, pericentric inversions might have been mediated by repetitive sequences like TEs in inverted configurations near centromeres and telomere-proximal regions. While no such inverted repeats were detected in our study, possibly due to decay over time, this hypothesis finds a parallel in recent chromosome fusion events in muntjac deer. In these species, telomeric and centromeric repeats at the fusion sites of ancestral chromosomes are still present, indicating their role in driving illegitimate recombination leading to chromosome fusions [45]. Notably, the events in muntjac deer occurred roughly 3 mya, thus significantly more recent than the divergence of the last common ancestor between 2 *Kwoniella* species with different karyotypes, such as *K. europaea* (1n = 3) and *K. bestiolae* (1n = 8), estimated approximately 21.2 mya. The potential discovery of more recently diverged *Kwoniella* species exhibiting karyotypic differences due to similar chromosomal fusion events could provide insights into these processes.

Moving forward, experimental approaches such as CRISPR-mediated pericentric inversion could model chromosomal fusion events observed in *Kwoniella* under laboratory conditions. Alternatively, using CRISPR to induce chromosome fusions, generating dicentrics similar to recent experiments in *C. deuterogattii* [67], could test if postfusion pericentric inversions occur. Successfully reducing chromosome numbers in both budding (*S. cerevisiae*) and fission (*Schizosaccharomyces pombe*) yeasts, yielding functional single-chromosome organisms, was recently achieved [136,137]. These unique yeasts showed comparable vitality to their wild-type counterparts under various conditions and stresses, with at most a slight reduction. However, when mixed with a normal strain, the single-chromosome budding yeast was rapidly outcompeted [136], suggesting that the mild fitness differences observed in the lab might be more detrimental in natural environments. Additionally, several genes involved in DNA replication were up-regulated in the single-chromosome budding yeast, indicating challenges in replicating the giant chromosome [136]. Interestingly, our selection analysis comparing *Kwoniella* species with 3 chromosomes to a sister clade with 8 to 11 chromosomes reveals differential selection in proteins associated with the centromere and kinetochores. This suggests centromere instability might be a catalyst for chromosome fusion in *Kwoniella*, and the potential mitotic segregation and replication challenges associated with larger chromosomes [70] have been either overcome or significantly mitigated in *Kwoniella*. Future research will examine chromosome stability in these species under different conditions, including meiosis.

Other mechanisms for chromosome fusion include dysfunction in telomere protection, as seen in human cells with compromised shelterin complexes leading to dicentric fusions [138–140]. While similar defects in shelterin subunits or telomerase in *Kwoniella* could be promoting chromosome fusions, our analysis did not reveal obvious defects in shelterin subunits or telomerase compared with *Ustilago maydis* [87,141,142], although the RNA subunit of telomerase in *Kwoniella* remains unidentified. While challenging to detect bioinformatically, innovative approaches like those used in *U. maydis* [143,144] could be key. However, telomeric repeat sequences present at chromosome termini in *Kwoniella* suggests functional telomerase and intact telomeres.

In contrast to chromosome fusions leading to giant chromosome formation in *Kwoniella* species, a strikingly different mode of karyotype evolution emerged from our comparative genomic analysis of pathogenic and nonpathogenic *Cryptococcus* species. The ancestral karyotype of 14 chromosomes has remained largely conserved in all of the pathogenic species and most (4 of 6) nonpathogenic species. Despite this conservation, *Cryptococcus* species have experienced significantly more interchromosomal rearrangements, both within and beyond

centromeric regions. Intercentromeric recombination between abundant and shared centromeric TEs has been well documented in *C. neoformans* and *C. amylolentus* [27,28,66]. Such recombination leads to balanced chromosomal translocations, resulting in stable monocentric chromosomes rather than unstable dicentric resulting from chromosome fusions [43]. In *C. depauperatus*, the chromosome number has been reduced from 14 to 8, by a process different from simple chromosome fusion. Instead, this reduction results from different types of rearrangements, including intercentromeric recombination followed by loss of repeat-rich centromeres. DNA double-stranded breaks in these regions can promote loss of centromeric sequence [43], and in *Malassezia* species centromere fission followed by fusion of the acentric chromosome arms to other chromosomes has driven chromosome number reduction [55].

Why is the pattern of karyotype evolution so strikingly different between *Cryptococcus* and *Kwoniella* species? These differences may be attributable to the size and complexity of their centromeres, as well as the presence or activity of mechanisms constraining TE movement. *Cryptococcus* centromeres are, on average, nearly 5 times larger than *Kwoniella* centromeres, with the largest *Cryptococcus* centromere exceeding 120 kb, compared to approximately 30 kb in *Kwoniella*. This size difference, along with a higher number of shared TEs in *Cryptococcus* centromeres, likely increases the frequency of homologous recombination leading to more chromosomal translocations. Additionally, our analysis also shows significantly higher TE density in *Cryptococcus* compared to *Kwoniella* (over 10-fold), suggesting a more active role of TEs in *Cryptococcus* genomic rearrangements. The disparity in TE prevalence between the 2 genera points to different mechanisms of TE control. One notable difference is the absence of the de novo DNA methyltransferase (DnmtX) gene in all *Cryptococcus* species, whereas all *Kwoniella* species have retained this gene. Based on analysis of 5mC DNA methylation patterns across the *Kwoniella* genus, it is clear TEs are methylated, and in species where H3K9me2 was analyzed, this also correlates with heterochromatin formation. Thus, the combination of de novo 5mC DNA methylation and heterochromatin formation may operate to dramatically reduce TE activity in *Kwoniella*, resulting in more compact centromeres and a lower genome-wide TE density. In contrast, without DnmtX, *Cryptococcus* species are unable to establish new methylation patterns on recently mobilized TEs, leading to less controlled TE activity and increased density in the genome. It is currently unclear if loss of de novo methylation in *Cryptococcus* is compensated by other TE suppression mechanisms, such as histone modifications (H3K9me2) or RNAi. Future research aimed at deciphering the interplay between DNA methylation and other epigenetic mechanisms in regulating TE activity in these species could involve expressing the DnmtX gene in *C. neoformans* strains, both with and without active RNAi and that exhibit high TE loads [123,145], and observing if this decreases transposon mobilization.

A final interesting facet that emerged from our comparative genomic analysis was the finding that several *Kwoniella* species harbor mini-chromosomes as linear pieces of DNA with telomeric repeats at both ends. To our knowledge, this is a novel finding for a yeast. Previous studies in other fungi have revealed similar examples of what have been termed accessory, dispensable, or B-chromosomes, and these have been associated with host range of plant fungal pathogens [146–149]. At present, the origin and biological function(s) of the *Kwoniella* mini-chromosomes are unknown, and it is unclear if they represent remnants resulting from past chromosome fusion events. Future studies can be directed to test their stability during mitosis, transmission following genetic crosses, and possible functions of genes they encode through gene deletion or chromosome loss analyses.

This research provides a robust platform for further studies. Incorporating comparative transcriptomic data could refine current annotations and aid in functional gene characterization, particularly those relevant to pathogenicity across different species. Future studies may

also include comparison of the closely related species comprising the *C. gattii* species complex to define genetic factors associated with more prevalent infections in immunocompromised patients by some species and in immunocompetent patients by others. Assessing the pathogenic potential of species of these 2 genera is crucial, especially as human encroachment into natural habitats exposes us to new opportunistic pathogens. This knowledge will be vital in anticipating and mitigating future health threats posed by these fungi.

Materials and methods

Strains and media

Strains studied in this work were grown on YPD (10 g/L yeast extract, 20 g/L Bacto Peptone, 20 g/L dextrose, and 20 g/L agar) media unless specified otherwise. *Cryptococcus* strains were incubated at 30˚C, while *Kwoniella* strains were grown at room temperature (20 to 23˚C). *E. coli* strains were grown on FB media (25 g/l tryptone, 7.5 g/L yeast extract, 1 g/L glucose, 6 g/L NaCl, 50mM Tris-HCl (pH 7.6)) with added ampicillin (100 μg/ml) and kanamycin (50 μg/ml) at 37˚C. Strains studied are listed in **S7 Appendix**.

Genomic DNA extraction

High-molecular weight (HMW) DNA was prepared with a cetyltrimethylammonium bromide (CTAB) extraction as previously described [43], avoiding vortexing during sample preparation. Where necessary, DNA samples for Oxford Nanopore or PacBio long read sequencing were enriched for HMW DNA (>25 kb) employing the Short Read Eliminator Kit (Circulomics/PacBio). Quality control was performed by determining A260/A280 and A260/A230 ratios on NanoDrop, and quantification was done with Qubit dsDNA Assay Kit (Invitrogen) on the Qubit fluorometer. The size and integrity of the DNA were confirmed by clamped homogeneous electric fields (CHEF) electrophoresis carried out at 6 V/cm with an initial switch time (IST) of 1 second and final switch time (FST) of 6 seconds, for 18 hours at 14˚C, in a CHEF-DR III system apparatus (Bio-Rad). CHEF gels were prepared with 1% pulsed field certified agarose (Bio-Rad) in 0.5X TBE or 1X TAE, with CHEF DNA 8 to 48 kb and CHEF DNA 5 kb (Bio-Rad) size standards. For some samples, gDNA extraction for Illumina sequencing was done with a phenol:chloroform-based protocol previously described [150], with minor modifications. Briefly, equivalent amounts of cell pellet and 0.5 mm acid-washed beads (approximately 250 μL) were mixed and washed with sterile bidistilled water. After centrifugation and removal of the supernatant, the pellet and beads were resuspended in 500 μL of DNA lysis buffer (10 mM Tris, 1 mM EDTA, 100 mM NaCl, 1% SDS, 2% Triton X-100 in water) and 500 μL of phenol:chloroform:isoamyl alcohol (25:24:1) solution. After cell disruption by bead beating at 4˚C, centrifugation, and collection of the supernatant, an additional chloroform extraction was performed. Supernatants were then precipitated in 100% ethanol for 1 hour, and gDNA pellets were then collected by centrifugation. After performing pellet clean-up with 70% ethanol, gDNA was dissolved in 10 mM Tris-Cl (pH 8), and treated with RNase A for 30 minutes at 37˚C. After a final chloroform extraction, ethanol precipitation and washing, the gDNA pellet was resuspended in 10 mM Tris-Cl (pH 8).

Illumina, Nanopore, and PacBio sequencing

Whole-genome sequencing was performed with Nanopore, PacBio, and Illumina technologies. Nanopore sequencing was carried out both in-house (Duke) and at the Broad Institute Technology Labs. PacBio sequencing was conducted at the Duke University Sequencing and Genomic Technologies (SGT) core, and Illumina sequencing was performed either at the Broad

Institute Genomics Platform or at the Duke SGT. For PacBio sequencing, 15- to 20-kb insertion-size libraries were prepared and run on a PacBio RS II or Sequel (2.0 chemistry) system. For nanopore sequencing, a single strain was sequenced using the SQK-LSK108 kit, or up to 4 different DNA samples were barcoded using the SQK-LSK109 and EXP-NBD103/EXP-NBD104 kits. These libraries, either single or pooled, were sequenced on R9 flow-cells (FLO-MN106) for 48 hours or 72 hours at default voltage in a MinION system using the latest MinION software. For some strains, 2 Illumina libraries were constructed. A fragment library was prepared from 100 ng of genomic DNA, sheared to approximately 250 bp using a Covaris LE instrument, and adapted for sequencing as previously described [151]. A 2.5-kb "jumping" library was prepared using the 2- to 5-kb insert Illumina Mate-pair library prep kit (V2; Illumina). These libraries were sequenced on an Illumina HiSeq 2000, producing 101-base paired reads. Specific details on sequencing platforms, basecalling, and demultiplexing are provided in **S1 Appendix** for each genome.

Genome assembly

Initial assemblies were conducted with Illumina data using Allpaths [152] for preliminary investigations of genome architecture. Complete genomes were then assembled with Canu [153] using default parameters and Nanopore or PacBio data, followed by polishing with Illumina short reads (see **S1 Appendix** for details). The consensus accuracy of Nanopore-based assemblies was improved by first correcting errors with Nanopolish v0.11.2 (https://nanopolish.readthedocs.io/en/latest/) and then with up to 5 rounds of polishing with Pilon v1.22 [154] (`--fix all`) with Illumina reads mapped to the first pass-polished assembly using BWA-MEM v0.7.17-r1188 [155]. PacBio-based assemblies were only polished with Pilon as above. Contigs containing exclusively rDNA sequences detected by Barrnap (https://github.com/tseemann/barrnap) (`--kingdom euk`) or that could be assigned to mitochondrial DNA were removed from the final nuclear assemblies. Assembly integrity (including telomeric regions) was confirmed by aligning Canu-corrected and Illumina reads with minimap2 v2.9-r720 [156] and BWA-MEM v0.7.17–93 r1188, respectively, and examining read coverage profiles in the Integrative Genomics Viewer (IGV) [157]. Genome assemblies and sequencing data are available at DDBJ/EMBL/GenBank, with accession numbers given in **S1 Appendix**.

Gene prediction, annotation, and statistical analyses

Gene models were predicted ab initio with BRAKER2 v2.1.5 [158] as previously described [11]. BRAKER2 was run in ETP-mode when RNA-seq data were available, leveraging both RNA-seq and protein data for GeneMark training. Otherwise, BRAKER2 was run in EP-mode, relying only on protein data for training. Protein sets from *C. neoformans* H99 [28] and *C. amylolentus* CBS6039 [27], along with RNA-seq data from 2 growth conditions (see below), were used as input. Naming of protein-coding genes combined results from HMMER PFAM/TIGRFAM, Swiss-Prot, and KEGG products. Gene set completeness was assessed with BUSCO v4.0.6 against the tremellomycetes_odb10 database [159,160]. Genomic features (number of genes, the number of introns in coding sequences (CDSs), and mean intron length) were calculated using AGAT (https://github.com/NBISweden/AGAT), utilizing the "agat_sp_statistics.pl" tool. Statistical analyses comparing these genomic features between *Cryptococcus* and *Kwoniella*, employed Python3 with Pandas, Seaborn, Matplotlib, and SciPy libraries. Differences between the 2 groups were assessed using the 2-sided Mann–Whitney U test. To evaluate correlations within each group, correlation analysis was conducted between genome size and other genomic metrics. The strength and direction of these correlations was quantified using the Spearman's correlation coefficient (ρ).

RNA extraction, sequencing, and data processing

RNA-seq libraries were prepared from *C. bacillisporus* CA1280, *C. decagattii* 7685027, *C. gattii* WM276, and *C. tetragattii* IND107 cells grown in 50 ml YPD, at 30°C or 37°C, conducted in duplicate. Each of these *Cryptococcus* cell preparations was spiked in with one-tenth (OD/OD) of *S. cerevisiae* strain S288C cells grown in YPD at 30°C, followed by washing and snap freezing. Total RNA was extracted with TRIzol as previously described [28] and then adapted for sequencing using the TagSeq protocol [161], in which ribosomal RNA was depleted using the RiboZero Yeast reagent. Sequencing was performed on an Illumina HiSeq 2000 at the Broad Institute Genomics Platform, producing 101-base paired reads. TagSeq adapters were removed and RNA-seq data were preprocessed with Trim Galore v0.6.7 (https://github.com/FelixKrueger/TrimGalore) discarding reads shorter than 75 nt after quality or adapter trimming (parameters: `--paired --quality 20 --phred33 --length 75`). Splice read alignment was performed with STAR aligner v2.7.4a [162] (indexing: `--genomeSAindexNbases 11`; aligning: `--alignIntronMin 10 --alignIntronMax 2000 --outSAMtype BAM SortedByCoordinate`). Spike-in reads from *S. cerevisiae* were first removed by keeping the reads that did not align to *S. cerevisiae* S288C genome. The remaining reads were then mapped to the respective *Cryptococcus* genome assemblies, and the resulting BAM files were input into the BRAKER pipeline.

Whole-genome bisulfite sequencing (WGBS) and 5mCG analysis

Genomic DNA from *Kwoniella* strains CBS8507, CBS10737, CBS12478, CBS6074, CBS10118, and PYCC6329 was isolated following the CTAB method. Following quantification and quality control, whole-genome bisulfite sequencing was performed at the Duke University SGT on a NovaSeq 6000 system to generate 50-base paired-end reads. Bisulfite-treated library reads were trimmed with Trim Galore v0.6.7 and analyzed with Bismark v0.22.3 [163] employing bowtie2 and the respective reference genome. Methylation was called using Bismark default settings. Additionally, 5mCG calls were obtained from the Nanopore data using Nanopolish [164]. Output files were converted to bedGraph format for visualization in IGV or for plotting with pyGenomeTracks [165].

Ortholog identification, alignment, and selection analysis

A phylogenomic data matrix was constructed with single-copy orthologs determined by OrthoFinder v2.5.2 [166] across all *Cryptococcus* and *Kwoniella* species, and 3 outgroups: *Tremella mesenterica* ATCC28783 (GCA_004117975.1), *Saitozyma podzolica* DSM27192 (GCA_003942215.1), and *Bullera alba* JCM2954 (GCA_001600095.1). OrthoFinder was run with default setting and with BLAST as the search tool. The amino acid sequences of 3,430 single-copy orthologs, identified as shared among all species, were individually aligned with MAFFT v7.310 [167] (arguments: `--localpair --maxiterate 1000`) and, subsequently trimmed with TrimAl v1.4.rev22 [168] (parameters: `--gappyout --keepheader`). For selection analysis, nucleotide sequences of single-copy orthologs were backaligned to their amino acid alignments using Egglib v3 [169]. For branch model analysis, a foreground species clade with 3 chromosomes (*K. europaea* PYCC6329, *Kwoniella* sp. B9012, *K. botswanensis* CBS12716, and *K. mangrovensis* CBS8507) was compared to a background species clade with 8 to 11 chromosomes (*K. bestiolae* CBS10118, *K. dejecticola* CBS10117, *K. pini* CBS10737, and *K. dendrophila* CBS6074), using an unrooted tree with codeml (with model = 2 NSsites = 0 CodonFreq = 7 and estFreq = 0) [170–172]. A null M0 model was run on the unrooted tree with no clade labels. Significance of fit between these models measured by the likelihood ratio test was corrected for multiple testing using FDR correction.

Species phylogeny and time tree estimation

A maximum likelihood (ML) phylogeny was with IQ-TREE v2.1.3 [173], employing a concatenation approach with gene-based partitioning. Individual protein alignments were input to IQ-TREE with `"-p"` argument to form a supermatrix (of 32 taxa, with 3,430 partitions and 1,803,061 sites) for partition analysis. This approach employs an edge-linked proportional partition model to account for variances in evolutionary rates across different partitions. The best amino acid substitution model for each partition was identified by ModelFinder applying the Bayesian information criterion (BIC). The highest-scoring ML tree was determined using the parameters "`--seed 54321 -m MFP -msub nuclear -B 1000 -alrt 1000 -T 20`", incorporating 1,000 iterations of the Shimodaira–Hasegawa approximate likelihood ratio test (SH-aLRT) and ultrafast bootstrap (UFboot) for branch support.

A time tree was computed in MEGA11 [174] utilizing the RelTime method [175]. This method relaxes the strict molecular clock assumptions in phylogenetic analysis and converts relative node ages into absolute dates using calibration constraints on one or more nodes. The inferred ML species phylogeny was taken as input and transformed into an ultrametric tree with relative times. Absolute dates were then assigned by applying 3 calibration constraints obtained from other studies [59,60] and the TimeTree project [176] (http://www.timetree.org/): the separation of *T. mesenterica* from other species (153.0 mya), the emergence of the pathogenic *Cryptococcus* species (27.0 mya), and the split between *C. neoformans* and *C. deneoformans* (24 mya). In RelTime, divergence times for the outgroup are not estimated when applying calibration constraints, as it relies on ingroup evolutionary rate to estimate divergence times, without presuming the evolutionary rates in the ingroup clade are applicable to the outgroup. Therefore, to utilize the divergence of *T. mesenterica* from other species as a calibration point, this species was incorporated as part of the ingroup for this analysis.

Gene genealogies

Protein sequences for the genes of interest were retrieved from the relevant orthogroups identified by OrthoFinder, subjected to manual inspection, and reannotated as required. The curated protein sequences were subsequently aligned, trimmed, and ML phylogenies were generated with IQ-TREE2. The resulting phylogenies were visualized with iTOL v5.6.3 [177]. The specific model parameters for phylogenetic reconstruction are provided in the corresponding figure legends.

Synteny analyses

Conserved synteny blocks between pairwise comparisons of *Cryptococcus* and *Kwoniella* genomes were determined using SynChro [69] with synteny block stringency (delta parameter) set to 3. Comparisons within *Kwoniella* and *Cryptococcus*, respectively, employed the genomes of *K. shandongensis* and *C. neoformans* as references. Synteny blocks determined by SynChro were also input to MCScanX_h [178] and visualized with SynVisio (https://synvisio.github.io/#/) for representation purposes (**Figs 1C**, **6A**, and **S3A**). Detailed linear synteny plots comparing chromosomes and specific genomic regions, such as centromeres, were generated with EasyFig [179] using BLASTN and retaining hits above 200 bp. Fusion events within *Kwoniella* were defined based on synteny plots and the positional information of centromeres in chromosomes as determined by in silico analysis and experimentally validated for selected species. By leveraging these visual representations, established phylogenetic relationships, and adhering to the principle of parsimony, chromosomal alterations were inferred with the following rationale: changes observed in identical order and orientation in 2 sister species were presumed to have been present in their common ancestor. Any changes failing to meet this

criterion were categorized as lineage-specific alterations. To enhance the clarity and readability of the figures, we modified the color schemes and labels in the SynChro, SynVisio, and EasyFig plots using Adobe Illustrator.

Analysis of repeat sequences and transposable elements

Repetitive elements were identified independently for all genomes by leveraging widely used library-based and de novo TE annotation tools as implemented in the EarlGrey pipeline [180]. Briefly, known repeats are first identified with RepeatMasker (CONS-Dfam_withRBRM_3.7) and de novo TE identification is performed with RepeatModeler2. Next, the set of consensus sequences obtained de novo are clustered using CD-HIT-EST to reduce redundancy. The resulting TE consensus sequences are extended through an interactive "BLAST, Extract, Extend" (BEE) process, and redundancy is removed again with CD-HIT-EST. The resulting TE consensus sequences are classified into specific families or labelled as "unclassified" if not matching a known family. The final nonredundant library, which combines both the known TE library and the TE consensus sequences obtained de novo, is utilized to annotate TEs across the genome using RepeatMasker, by applying a conservative threshold ("-cutoff 400"). Lastly, spurious hits less than 100 bp in length are excluded from the TE annotations prior to final quantification. Overlaps between centromeres and repetitive elements were assessed with bedtools v2.27.1 [181]. The uncharacterized status of significant TE numbers in some species may be attributable to the progressive erosion of TE sequences by mutational processes, diminishing their recognizability and identifiability. TE data and statistical analyses associated with Fig 5 are provided in **S6 Appendix.** Plots were generated using Python and stylized for publication with Adobe Illustrator.

Generation of mCherry-tagged Cse4 (CEN-A) strains in different *Kwoniella* species

The Cse4/CENP-A gene was identified in *Kwoniella* genomes by TBLASTN, with *C. neoformans* (CNAG_00063) and *C. amylolentus* (L202_03810) Cse4 sequences as queries. A mCherry-tagged Cse4 fusion protein was generated via overlap extension-PCR (OE-PCR). For this, the upstream/promoter region of *CSE4* and the *CSE4*-ORF with its respective downstream/terminator region were amplified from strain CBS10118, and the mCherry ORF was amplified from plasmid pVY50 [27] using primers with specific complementary 5′ ends of 60 bp each (**S7 Appendix**). These fragments were then purified and assembled via OE-PCR into a complete amplicon encoding the N-terminally mCherry-tagged Cse4/CENP-A gene, regulated by its endogenous promoter and terminator regions. The amplicon, further amplified with primers MP253/MP254 (containing ApaI and XhoI restriction sites; **S7 Appendix**), was digested with both restriction enzymes and gel purified. Similarly, plasmid pVY50 was digested with the same enzymes, followed by gel purification, to retrieve a 5,809-bp fragment composed by the backbone of the plasmid encoding, among other elements, a fungal neomycin (NEO) resistant gene. The complete digested amplicon was then cloned into the corresponding sites of pVY50 to generate plasmid pMP01 (**S7 Appendix**). The same approach was employed to generate plasmids pMP02 and pMP03 encoding mCherry-tagged Cse4/CENP-A of *K. europaea* PYCC6329 and *K. dendrophila* CBS6074, respectively (**S7 Appendix**). The resulting plasmids were introduced into TOP10 *E. coli*, grown overnight at 37°C, and post-miniprep recovery, validated through restriction analysis and Sanger sequencing.

A minimum of 10 μg of circular plasmid DNA was used for biolistic transformation [182] of each *Kwoniella* strain. Transformants were selected on YPD media supplemented with 200 μg/ml of neomycin. Transformation of *K. bestiolae* and *K. europaea* successfully yielded transformants, but attempts to transform *K. dendrophila* CBS6074 with plasmid pMP03 were

unsuccessful. Consequently, *K. pini* CBS10737, phylogenetically close to *K. dendrophila* and with 11 chromosomes, was chosen as an alternative. Biolistic transformation of *K. pini* with pMP03 successfully recovered transformants. At least 2 independent transformants of each species underwent fluorescent microscopy screening to ascertain the expression of the tagged protein. Selected transformants were stained with Hoechst 33342 and imaged using a Delta Vision Elite deconvolution microscope with a CoolSNAP HQ2 CCD camera at Duke University Light Microscopy Core Facility. Images were processed using Fiji-ImageJ (https://imagej.net/Fiji) (RRID:SCR_002285).

Chromatin immunoprecipitation followed by high-throughput sequencing (ChiP-seq)

ChIP-seq was conducted to identify Cse4-enriched regions in tagged species (*K. bestiolae*_m-Cherry-Cse4, *K. europaea*_mCherry-Cse4, and *K. pini*_mCherry-Cse4), using a polyclonal antibody against mCherry (ab183628, Abcam) as previously described [68]. Similarly, ChIP-seq for *K. bestiolae* CBS10118, *K. europaea* PYCC6329, *K. pini* CBS10737, *K mangrovensis* CBS8507, and *K. dendrophila* CBS6074 was performed to detect histone H3K9me2-enriched regions, employing a monoclonal antibody against histone H3K9me2 (ab1220, Abcam). Libraries were prepared and sequenced at the Duke University SGT, using either a NovaSeq 6000 or a HiSeq 4000 instrument to produce 50-bp paired-end reads. ChIP-seq sequencing reads were trimmed with Trim Galore v0.6.7 and subsequently aligned to each respective genome assembly with bowtie2. Read duplicates were removed with Picard and SAMtools, and bamCompare v3.5.4 was used to normalize the ChIP-seq data against the input control. The resulting files were converted to bedGraph format for visualization in IGV or for plotting with pyGenomeTracks.

CHEF electrophoresis of *Kwoniella* chromosomes

Spheroplasts with intact chromosomal DNA were generated in plugs, as previously described [23], for *Kwoniella* strains CBS10118, CBS8507, and PYCC6329 with minor modifications: (i) cells were grown in Yeast Nitrogen Base (YNB) liquid minimal medium supplemented with NaCl (1 M); and (ii) zymolase (25 mg/mL) or *Trichoderma harzianum* lysing enzymes (50 mg/mL for *K. mangrovensis*) were used to lyse the cells embedded in the agarose, with overnight reactions at 37°C. Gels were prepared with 0.8% or 0.9% of Megabase agarose (Bio-Rad), and chromosomal separation was conducted with the CHEF DR-II System and the CHEF Mapper XA System (Bio-Rad, Richmond CA) using different running and buffer conditions, and different size markers selected based on the chromosome size range of each assay (details in **S2 Fig**). Following electrophoresis, gels were stained with ethidium bromide, unstained using the running buffer, and photographed under a UV transillumination imaging system.

Hi-C mapping

Hi-C mapping of *Kwoniella* strains CBS10118, CBS8507, and PYCC6329 was performed as previously described [183], with minor modifications. Cells were grown overnight in YPD, after which a solution of 37% formaldehyde was added to a final concentration of 3% of the total volume. After incubation at 25°C for 20 minutes, the cross-linking reaction was quenched by adding 2.5 M glycine at 2X the volume of formaldehyde used, followed by incubation at 25°C for 20 minutes. Washed cell pellets were resuspended in 50 mL of 1× NEBuffer 2, flash frozen in liquid nitrogen, grinded up to a powder, and then resuspended in the same buffer to an OD600 of 10.0. In situ Hi-C sequencing libraries [184] were generated from 0.75 mL cell suspensions. Cell pellets were resuspended in 250 μL ice-cold Hi-C lysis buffer (10 mM Tris-HCl (pH 8.0), 10 mM NaCl, 0.2% Igepal CA630, 1 tablet/10 mL Roche complete mini EDTA-

free protease inhibitor), kept on ice for 5 minutes, centrifuged (5 minutes at 2,500 × *g* at 4˚C) and washed in 500 μL Hi-C lysis buffer. Pellets were resuspended in 50 μL 0.5% SDS and incubated for 10 minutes at 62˚C to permeabilize nuclei. After adding 140 μL H$_2$O and 25 μL 10% Triton X-100 and 15 minutes at 37˚C to quench the SDS, 25 μL 10× CutSmart buffer and 10 μl 10 U/μL MseI restriction enzyme (New England Biolabs) were added, and chromatin digested overnight at 37˚C with rotation. MseI was heat-inactivated (20 minutes at 62˚C) and fragment ends filled-in and biotinylated by adding 27.5 μl of a cocktail containing 15 μL 1 mM biotin-14-dUTP (Jena BioScience), dCTP, dGTP, dATP (3× 1.5 μL of 10 mM solutions), and 8 μL of 5 U/μl Klenow fragment of DNA polymerase I (New England Biolabs) and a 30-minute incubation at 37˚C with rotation. For blunt-end ligation, 900 μL of a cocktail containing 663 μL H$_2$O, 100 μL 10% Triton X-100, 120 μL 10× T4 DNA ligase buffer and 5 μL of 400 U/μL T4 DNA ligase (New England Biolabs) was added. After 2 hours at room temperature with rotation, tubes were centrifuged (5 minutes at 2,500 × *g*), supernatants were carefully removed and the pellets resuspended in 300 μL 1% SDS, 10 mM Tris-HCl (pH 8.0), 0.5 M NaCl. After adding 10 μL of 20 mg/μL proteinase K (New England Biolabs), proteins were degraded for 30 minutes at 55˚C followed by an overnight incubation at 68˚C with shaking to reverse crosslinks. Insoluble material including apparently intact cells were spun down (5 minutes at 2,500 × *g*). DNA in the supernatant was precipitated in the presence of 1 ul (20 mg) glycogen with 2 volumes of ethanol at −80˚C for 15 minutes and spun down for 15 minutes at 13,000 rpm at 4˚C. The pellet was washed with 800 μL 70% ethanol and dissolved in 130 μL TE buffer (10 mM Tris-HCl (pH 8.0), 0.1 mM EDTA). The DNA was sheared to approximately 450 bp in a 130-μL vial on a Covaris S2 instrument set to 7˚C, duty cycle 10%, intensity 4, 200 cycles/burst, 2 cycles of 35 seconds. Sheared DNA was cleaned-up with 0.55 volumes of AmPure XP beads (Beckman Coulter) and eluted in 300 μL TE buffer. DNA molecules containing biotinylated ligation junctions were pulled down on Dynabeads MyOne Streptavidin T1 beads (Life Technologies). For each capture, 150 μL beads were washed with 400 μL 1× Tween Washing Buffer (TWB; 1M NaCl, 5 mM Tris-HCl (pH 7.5), 0.5 mM EDTA; 0.05% Tween-20) and resuspended in 300 μL 2× Binding Buffer (2× BB; 2M NaCl, 10 mM Tris-HCl (pH 7.5), 1 mM EDTA) and mixed with 300 μL sheared DNA for 15 minutes at room temperature. Beads were washed twice in 600 μL TWB for 2 minutes at 55˚C and once in 100 μL TE buffer. On-bead end repair, adapter ligation, and PCR amplification were performed using the Kapa Hyper Prep kit (Roche). Beads were resuspended in 60 μL of a cocktail containing 50 μL H$_2$O, 7 μL end repair and A-tailing buffer and 3 μL enzyme mix and incubated for 30 minutes at 20˚C and 30 minutes at 65˚C. A cocktail containing 5 μL H$_2$O, 30 μL ligation buffer, 10 μL T4 DNA ligase, and 5 μL undiluted (15 μM) Unique Dual Indexed adapters were added and the reactions incubated for 15 minutes at room temperature. Beads were collected, washed twice for 2 minutes at 55˚C in TWB and once in 100 μL TE buffer, resuspended in a cocktail containing 40 μL H$_2$O, 50 μL 2× Kapa HiFi Hot Start Ready Mix and 10 μL Kapa Illumina amplification primers, split in 2 × 50 μL in strip tubes and thermocycled: 30 seconds at 98˚C; 8 cycles of 10 seconds at 98˚C, 30 seconds at 55˚C, 30 seconds at 72˚C; 7 minutes at 72˚C. Beads were pelleted on a magnet and the supernatant cleaned up with 0.7 volumes of AMPure XP beads. Libraries were characterized by BioAnalyzer, pooled and sequenced on an Illumina HiSeq 2500 instrument. Hi-C plots were generated with Juicebox, using Juicer v1.5.6 after alignment of the Illumina reads with BWA 0.7.12-r1039.

Supporting information

S1 Fig. *Cryptococcus* and *Kwoniella* phylogeny and genomic features. (A) Maximum likelihood phylogeny of *Cryptococcus* and *Kwoniella* inferred through a concatenation-based

approach on a data matrix composed of protein alignments of 3,430 single-copy genes shared across all species and 3 outgroups (depicted in grey). Except where indicated, all branches are 100% supported (SH-aLRT and UFboot tests). Branch lengths are given in number of substitutions per site (scale bar). The isolation origin of each strain is indicated as given in the key. **(B)** Genome sequencing approach for each of the strains. **(C)** BUSCO completeness assessment of each genome gene set. **(D)** Frequency distribution of GC content across species, with mean GC values represented by vertical lines. **(E)** Number of genes, **(F)** mean number of introns within coding sequences (CDSs), and **(G)** their mean length (in base pairs, bp). Box plot comparisons of **(H)** genome sizes, **(I)** number of genes, **(J)** mean intron length, and **(K)** mean number of introns in CDSs, between *Cryptococcus* and *Kwoniella*. The red line, black line, boxes, and grey circles denote the mean value, median value, interquartile range, and outliers, respectively. *P* values obtained by Mann–Whitney U test; n.s., not significant. **(L, M)** Comparative analysis of gene count, intron length, and mean number of introns relative to total genome size. Each plot shows Spearman's correlation coefficients (ρ) and associated *P* values indicating the strength and direction of these relationships. The data underlying this Figure can be found in **S1 Appendix** and at https://doi.org/10.5281/zenodo.11199354. (TIF)

S2 Fig. Genome assembly validation of representative *Kwoniella* species by clamped homogeneous electrical field (CHEF) electrophoresis and Hi-C mapping. (A-D) Electrophoretic karyotypes of selected *Kwoniella* species with different number of chromosomes: *K. bestiolae* with 8 chrs (blue); *K. europaea* and *K. mangrovensis* with 3 chrs. each (orange and green, respectively); and *K. dejecticola* (purple), *K. pini*, and *K. shivajii* with 11 chrs. each. *Saccharomyces cerevisiae*, *Schizosaccharomyces pombe*, and *Hansenula wingei* chromosomes serve as markers, with their sizes in megabase pairs (Mb) shown in black. Color-coded numbers indicate contigs sizes in each respective assembly. Two running conditions were used for better separation of small and large chromosomes in *K. bestiolae* and *K. europaea* (panels A and B). The largest chromosomes in *K. bestiolae* (8.41 Mb), *K. europaea* (16.67 Mb), and *K. mangrovensis* (18.17 Mb) are too large to be resolved by this approach. The karyotypes of *K. dejecticola*, *K. pini*, and *K. shivajii* confirm 11 chrs. in each species, aligning with the contig number and length. The contig size harboring the rDNA array in *K. dejecticola* (indicated by an asterisk) is likely underestimated. **(E)** Hi-C contact matrix showing interaction frequencies between genomic regions, with pixel intensity indicating how often a pair of loci interact. Most of the links are nearby intrachromosomal, validating our assemblies. Interaction frequencies produced with Juicer Tools v1.7.6 are summarized along the genome. Chromosome numbers are given at the bottom of each plot. In *K. mangrovensis*, chr. 1 is broken at the rDNA array (black arrow in each plot) and shown as 2 contigs (1a and 1b). (TIF)

S3 Fig. Centromere conservation between *C. neoformans*, *C. amylolentus*, and *K. shandongensis*. (A) Pairwise synteny relationships between *C. neoformans*, *C. amylolentus*, and *K. shandongensis*, all with 14 chromosomes. Links depict boundaries of syntenic gene blocks identified by MCScanX, with pairwise homologous relationships determined by SynChro. Chromosomes are color-coded based on *C. neoformans* and were reordered or inverted (marked with asterisks) from their original assembly orientations to maximize collinearity. **(B)** Superimposition of synteny blocks and centromere locations reveals 3 intercentromeric rearrangements between *C. neoformans* and *C. amylolentus*, as opposed to a single one between *C. neoformans* and *K. shandongensis*. **(C)** Synteny analysis based on BLASTN comparing chromosomal regions encompassing centromeres in *K. shandongensis* (predicted in silico) relative to previously determined centromeres of *C. neoformans*. Despite the numerous

intrachromosomal rearrangements between these 2 species, centromere-flanking regions exhibit full (e.g., *CnCEN2*) or at least partial (e.g., *CnCEN6/8*) synteny.
(TIF)

S4 Fig. Ancestral chromosome fusion events in *Kwoniella*. Synteny comparison showing that **(A)** chr. 2 of *Kwoniella* sp. DSM27419 resulted from the fusion of *K. shandongensis* chrs. 11 and 12. and that **(B)** chr. 1 of *Kwoniella* sp. DSM27419 emerged from the fusion of 3 chromosomes extant in *K. shandongensis* (chrs. 2, 13, and 14), followed by several intrachromosomal rearrangements. These 2 fusion events, inferred as the oldest within *Kwoniella* (event A in Fig 2), resulted in chromosome arrangements consistent across all species after the split from *K. shandongensis*/*K. newhampshirensis* (albeit with a few subsequent species-specific rearrangements). Note that the centromere-proximal regions of *K. shandongensis* chromosomes align at or near the fusion points on *Kwoniella* sp. DSM27419 fused chromosomes, while telomere-proximal regions are more internal, suggesting large inversions targeting centromeric regions accompanied each fusion event. In *K. heveanensis*, and sibling species *Kwoniella* sp. CBS6097 and *Kwoniella* sp. CBS9495, chr. 2 results from a subsequent fusion of *K. shandongensis* chr. 4 to the already fused chr. 11–12 (event D in Fig 2), followed by several intrachromosomal rearrangements. This event occurred in the common ancestor of these 3 species and the centromere- and telomere-proximal regions have been inverted back by a secondary inversion (double-sided black arrow) that occurred after the initial fusion. Chromosomes inverted from their original assembly orientations are marked with asterisks.
(TIF)

S5 Fig. Formation of a giant chromosome in *K. heveanensis* and sibling species. Synteny comparison showing that chr. 1 of *K. heveanensis* and sibling species *Kwoniella* sp. CBS6097 and *Kwoniella* sp. CBS9495 resulted from fusion of 6 chromosomes, followed by several intrachromosomal rearrangements. Three of the ancestral chromosomes had been fused prior to this event (chrs. 2-13-14). Note that most of centromere-proximal regions of *K. shandongensis* chromosomes are located at or near the fusion points on the giant chromosome, whereas the telomere-proximal regions are more internalized, suggesting that a large inversion targeting the centromeric region is associated with each fusion event. Chr. 11 of *Kwoniella* sp. DSM27419 resulted from reciprocal translocation between *K. shandongensis* chrs. 6 and 7 (event C in Fig 2).
(TIF)

S6 Fig. Formation of a large chromosome in *K. bestiolae*. (A) Synteny comparison showing that *K. bestiolae* chr. 1 resulted from fusion of 4 chromosomes, extant in *K. pini*. Two of the ancestral chromosomes had been fused prior to this event (chrs. 11 and 12). *K. pini* chr. 3 resulted from a translocation between *K. shandongensis* chr. 4 and an ancestrally formed chromosome resulting from fusion of *K. shandongensis* chrs. 2, 13, and 14 (event B in Fig 2). **(B, C)** Zoomed-in synteny views of the regions marked in panel A (pins with lowercase letters from a–h). Note that most of centromere-proximal regions of *K. pini* chromosomes are located at or near the fusion points on the giant chromosome, whereas the telomere-proximal regions are more internalized, suggesting that a large inversion targeting the centromeric region is associated with each fusion event. A secondary inversion (double-sided black arrow) likely occurred in *K. pini* reversing the relative orientation of the centromere and a few flanking genes. Species-specific differences in gene content and relative orientation are expected as these species have diverged for a long time.
(TIF)

S7 Fig. CENP-A expression and kinetochore components across *Cryptococcus* and *Kwoniella*. (A) Kinetochore ensemble schematic with color-coded protein complexes or faded out to indicate absence. **(B)** Matrix showing the presence (blue) and absence (grey) of the kinetochore components proteins depicted in panel A. **(C)** Live cell imaging of *K. europaea*, *K. bestiolae*, and *K. pini* expressing mCherry-tagged CENP-A, showing nucleus subcellular localization (scale bar, 10 μm).
(TIF)

S8 Fig. Localization of CENP-A to contiguous regions defines centromeres on each of the 3 chromosomes of *K. europaea*. (A) Whole chromosome plots showing CENP-A (black) and H3K9me2 (orange) enrichment, CG cytosine DNA methylation (5mCG, green) derived from WGBS, repeat content (pink), TCN-like LTR elements (purple), and GC content show as deviation from the genome average (red, above; blue, below). CENP-A- and H3K9me2-enriched regions were normalized to input DNA. The data are computed in 5-kb nonoverlapping windows. **(B)** Zoomed-in sections show the regions spanning the centromeres and adjacent genes (light blue). Note that centromeres are enriched for CENP-A, H3K9me2, and 5mCG DNA methylation marks and contain repeat elements.
(TIF)

S9 Fig. Localization of CENP-A to contiguous regions defines centromeres on each of the 8 chromosomes of *K. bestiolae*. (A) Whole chromosome plots showing CENP-A (black) and H3K9me2 (orange) enrichment, CG cytosine DNA methylation (5mCG, green) derived from WGBS, repeat content (pink), TCN-like LTR elements (purple) and GC content show as deviation from the genome average (red, above; blue, below). CENP-A- and H3K9me2-enriched regions were normalized to input DNA. **(B)** Zoomed-in sections show the regions spanning the centromeres and adjacent genes (light blue). Note that centromeres are enriched for both CENP-A and H3K9me2 marks but 5mCG enrichment was only observed in a subset of centromeres, and even in these cases, it was localized to specific regions instead of the whole-centromere. The data are computed in 5-kb nonoverlapping windows.
(TIF)

S10 Fig. Localization of CENP-A to contiguous regions defines centromeres on each of the 11 chromosomes of *K. pini*. (A) Whole chromosome plots showing CENP-A (black) and H3K9me2 (orange) enrichment, CG cytosine DNA methylation (5mCG, green) derived from WGBS, repeat content (pink), TCN-like LTR elements (purple) and GC content show as deviation from the genome average (red, above; blue, below). CENP-A- and H3K9me2-enriched regions were normalized to input DNA. **(B)** Zoomed-in sections show the regions spanning the centromeres and adjacent genes (light blue). Note that centromeres are enriched for both CENP-A and H3K9me2 marks but are completely devoid of 5mCG DNA methylation despite the presence of this heterochromatic mark in other genomic regions. The data are computed in 5-kb nonoverlapping windows.
(TIF)

S11 Fig. Evolution of DNA methyltransferases Dnmt5 and DnmtX in *Cryptococcus* and *Kwoniella* involved in cytosine methylation of DNA. (A) Species tree topology indicating the presence/absence of 2 previously characterized DNA methyltransferases: Dnmt5 (encoded by *DMT5* gene) is a maintenance-type DNA methyltransferase and DnmtX (encoded by *DMTX* gene) is a de novo methylase. Phylogenetic and BLAST analysis confirmed initial reports that the ancestral species of the 2 clades likely had both genes, but *DMTX* was lost in the *Cryptococcus* common ancestor, including in the early-branching *Cryptococcus* sp. OR918 lineage analyzed in this study. The *DMTX* gene is also absent in *Bullera alba*, indicating additional losses

are expected to have occurred within the Tremellomycetes. The only instance of *DMT5* loss in our dataset is observed in *C. depauperatus*, and our Nanopore data confirm absence of 5mC methylation in this species. **(B)** Similar structure of Dnmt5 across species, characterized by an N-terminal chromodomain (CD) followed by a cytosine methyltransferase catalytic domain (DNMT), and a domain related to those of SNF2-type ATPases **(C)**. The DnmtX protein is shorter and contains a bromo-associated homology (BAH) domain and a DNMT catalytic domain.
(TIF)

S12 Fig. The predicted centromeres of *K. dendrophila* lack repeat elements and 5mC DNA methylation but are enriched for H3K9me2. (A) Whole chromosome plots displaying H3K9me2 enrichment (orange), CG cytosine DNA methylation (5mCG, green) from WGBS, repeat content (pink), and GC content show as deviation from the genome average (red, above; blue, below). H3K9me2-enriched regions were normalized to input DNA. **(B)** Close-ups of predicted centromeres and adjacent genes (light blue) highlights H3K9me2 enrichment but absence of 5mCG methylation and transposable elements. The data are computed in 5-kb nonoverlapping windows.
(TIF)

S13 Fig. Variable presence of LTR retrotransposons within predicted centromeres of *K. shandongensis* and *K. newhampshirensis*. (A and **C)** Whole chromosome plots displaying CG cytosine DNA methylation (5mCG, green) from WGBS (*K. shandongensis*) or ONT data (*K. newhampshirensis*), alongside repeat content (pink), and GC content show as deviation from the genome average (red, above; blue, below). **(B** and **D)** Close-ups of predicted centromeres and adjacent genes (light blue) highlight diverse 5mCG methylation patterns. While most centromeres encompass unclassified repeats, only a few contain LTR retrotransposons (purple). In *K. newhampshirensis*, chr. 10 corresponds to assembled contigs 14 and 15, broken at the rDNA array, and chrs. 15 and 16 are mini-chromosomes with yet-to-be-determined centromere positions; however, these might correspond to the regions high in 5mCG and low in GC content. The data are computed in 5-kb nonoverlapping windows.
(TIF)

S14 Fig. Evolution of the core RNAi components in *Cryptococcus* and *Kwoniella*. (A) Species tree topology indicating the presence/absence of the core RNAi components (Argonaute, Dicer, and RNA-dependent RNA polymerase) across species as well as the inferred pattern of gene gain (via duplication) and loss during evolution. The common ancestor of the 2 groups was an RNAi-proficient organism, likely expressing 2 Argonaute proteins (Ago1 and Ago4), 1 Dicer (Dcr1), and 1 RNA-dependent RNA polymerase (Rdp1). Psi symbols indicate pseudogenization events and numbers indicate additional species-specific copies. **(B)** Protein domain organization of the 3 Argonaute proteins found in *K. shandongensis*, depicted here as a representative. **(C)** ML phylogeny of the different Argonaute proteins. The tree was constructed with IQ-TREE2 (model LG+F+R5) and rooted at the midpoint. Internal branch support was assessed by 10,000 replicates of the Shimodaira–Hasegawa approximate likelihood ratio test (SH-aLRT) and ultrafast bootstrap (UFboot). Branch lengths are given in number of substitutions per site. The tree file is provided at https://doi.org/10.5281/zenodo.11199354. **(D)** Genomic region containing the *AGO1*, *AGO2*, and *AGO3* genes across species. For simplicity, all other genes were omitted. Within the clade comprising *C. floricola*, *C. wingfieldii*, *C. amylolentus*, and *Cryptococcus* sp. OR849, a high prevalence of repeat elements is observed in this region, which may have contributed to the loss of *AGO1* in *C. floricola* and its

pseudogenization in *Cryptococcus* sp. OR849.
(TIF)

S15 Fig. Evolution of Znf3 in *Cryptococcus* and *Kwoniella*. (A) Species tree topology indicating the presence/absence of Znf3 across species. **(B)** Protein domain organization of Znf3 proteins. Most of the proteins exhibit 4 C2H2 zinc finger domains and a few conserved coiled coil regions, often involved in protein–protein interactions. **(C)** ML phylogeny of the different Znf3 proteins. The tree was constructed with IQ-TREE2 (model JTT+F+I+G4) and rooted with *T. mesenterica*. Internal branch support was assessed by 10,000 replicates of the Shimodaira–Hasegawa approximate likelihood ratio test (SH-aLRT) and ultrafast bootstrap (UFboot). Branch lengths are given in number of substitutions per site. The tree file is provided at https://doi.org/10.5281/zenodo.11199354. **(D)** Genomic region encompassing the *ZNF3* gene across species. For simplicity, all other genes were omitted. The genomic region containing the *ZNF3* in *C. neoformans* H99 was plotted 3 times for comparison. **(E)** Detailed view depicting newly identified losses of *ZNF3* in *Cryptococcus* sp. OR849 and *Cryptococcus* sp. OR918. **(F)** Detailed view depicting a smaller *ZNF3* gene in *Kwoniella* sp. DSM27419. Colored genes in panels E and F denote those consistently present across all species within the compared region.
(TIF)

S16 Fig. *Kwoniella* species with "mini-chromosomes". (A) Validation of "mini-chromosomes" (less than 100 kb) via PFGE in *Kwoniella* sp. DSM27419 and *K. newhampshirensis* CBS13917, and their absence in *Kwoniella* sp. CBS6097 and *Kwoniella* sp. CBS9459. Contig sizes and respective chromosome numbers are shown next to the gel lane. **(B)** Example of a mini-chromosome assembly validation, evidenced by uniform coverage mapping (blue areas) of both short (Illumina) and long (ONT) reads spanning the full chromosome. The panels below show close-up views of the left and right ends of the mini-chromosome emphasizing the presence of telomeric repeats. **(C-F)** Plots displaying individual chromosome sizes, color-coded based on gene genomic coverage (defined as the ratio of total gene length on a contig to the total length of that contig). In panels D and E, the adjacent boxplots illustrate statistically significant difference (Mann–Whitney U test) in gene genomic coverage between mini-chromosomes and other chromosomes. **(G, H)** Boxplots showing a notable difference (Mann–Whitney U test) in GC content between mini-chromosomes and other chromosomes in *Kwoniella* sp. DSM27419 and *K. newhampshirensis* CBS13917, respectively. While chr. 12 of *Kwoniella* sp. DSM27419 was categorized as a non-mini-chromosome in these analyses (larger than 100 kb and, thus, not visible in the gel in panel A), it exhibits intermediate gene genomic coverage. Chromosomes containing rDNA are indicated by an R and their size is likely underestimated. The data underlying this Figure can be found in **S1 Appendix** and at https://doi.org/10.5281/zenodo.11199354.
(TIF)

S17 Fig. Evolution of the *ZRT1-PRA1* pathogenesis gene cluster in *Cryptococcus* and *Kwoniella*. (A) Species tree topology illustrating the evolutionary trajectory of zinc transporter families and the Pra1 zincophore in *Cryptococcus* and *Kwoniella*. Gene presence in extant species is indicated in color, while absence is shown in grey. **(B)** ML phylogeny of major zinc-related transporters in our dataset. The tree shows a distinct separation into 5 groups. Orthologs from *Saccharomyces cerevisiae*, *Candida albicans*, and *Aspergillus fumigatus*, previously characterized (shown in grey), are included for comparative purposes and to aid in functional prediction. Genes included in the Zrt1 and Zrt2 families are predicted to transport zinc and localize to the plasma membrane (PM); those included in the Atx2 family may have more

affinity to manganese transport and localize to Golgi (G); and those within the Yke4 family may function as bidirectional zinc transporters located in the endoplasmic reticulum (ER). The Zrt1 family encompasses 2 different sets of proteins: Zrt1 and Zip2. The *ZRT1* gene is always clustered with *PRA1*, whereas *ZIP2* is found elsewhere in the genome. Note that the *ZRT1-PRA1* gene cluster was lost in all of the *Cryptococcus* pathogenic species. **(C)** ML phylogeny of Pra1 with sequences identified across *Cryptococcus* and *Kwoniella*. A diverged copy of *PRA1* (labelled as *PRA1-2*) is present in the early derived *Cryptococcus* sp. OR918 as well as in most *Kwoniella* species. Midpoint rooted phylogenetic trees in panels B and C, with branch lengths representing number of substitutions per site, were constructed with IQ-TREE2 (using models LG+R6 and WAG+G4, respectively), and with internal branch support assessed by 10,000 replicates of Shimodaira–Hasegawa approximate likelihood ratio test (SH-aLRT) and ultrafast bootstrap (UFboot). The tree files are provided at https://doi.org/10.5281/zenodo.11199354. **(D)** Protein domains of zinc transporters and putative Pra1 zincophores identified in *K. europaea*, shown here as an example. **(E)** Genomic region encompassing the *ZRT1-PRA1* gene cluster in species where it is present. For simplicity, all other genes were omitted. **(F, G)** Synteny analysis illustrating the species-specific losses of the *ZRT1-PRA* gene cluster in *Cryptococcus* sp. OR849 and *K. newhampshirensis*.
(TIF)

S18 Fig. Structural comparison of D-lactate dehydrogenase proteins from AlphaFold predictions. AlphaFold-predicted structures of *Cryptococcus neoformans* (UniProt J9VFV7), *Aspergillus fischeri* (UniProt A1D163), and *Escherichia coli* (UniProt P52643) are individually displayed at the top. Pairwise structure alignments with the *C. neoformans* protein were conducted with the JjFATCAT-rigid algorithm on the Protein Data Bank website (https://www.rcsb.org/alignment). The table below presents the resulting root mean square deviation (RMSD) and template modeling (TM) scores, among other metrics. The comparison reveals high structural similarity across these proteins, evidenced by low RMSD and high TM scores. The notably lower RMSD score between the 2 fungal proteins, aligns with the proposed hypothesis of a horizontal gene transfer event from an Aspergilli donor lineage to pathogenic *Cryptococcus* species.
(TIF)

S1 Text. Identification and evolutionary analysis of RNAi components in *Cryptococcus* and *Kwoniella*.
(PDF)

S2 Text. Identification of shelterin complex and telomere maintenance genes in *Cryptococcus* and *Kwoniella*.
(PDF)

S1 Appendix. Genome assembly, genomic features, and information on raw sequencing data generated in this study. (**A**) List of *Cryptococcus* and *Kwoniella* isolates used in this study and summary of genome assembly statistics and other genomic features. (**B**) Genome sequencing, assembly, and polishing approaches. (**C**) NCBI accession numbers of each genome and raw read data generated and used in this study. (**D**) Centromere coordinates and telomeric sequences. (**E**) Gene genomic coverage and GC content in *Kwoniella* species containing minichromosomes. (**F**) Genomic features (genome size, number of protein coding genes, number of introns in coding sequences (CDSs), mean intron length, and number of introns in CDSs) and associated statistical tests. (**G**) Reference genome assemblies of *C. gattii* species complex and *C. deneoformans* JEC21 available prior to this study.
(XLSX)

S2 Appendix. List of genes analyzed in this study with a presumed role in chromosomal integrity. A) Kinetochore components. (B) RNAi and SCANR complex components. (C) Shelterin and other predicted genes presumably involved in telomere maintenance. (D) List of S. cerevisiae essential-DAmP (Decreased Abundance by mRNA Perturbation) genes that exhibit short telomere phenotype and corresponding *Cryptococcus and Kwoniella* orthologs. (E) List of *S. cerevisiae* genes that results in shorter telomere length when deleted and corresponding *Cryptococcus and Kwoniella* orthologs. (F) DNA and histone methyltransferases.
(XLSX)

S3 Appendix. Significance of branch model fit for *Kwoniella* chromosome number-based subset, dN/dS results from branch model.
(XLSX)

S4 Appendix. List of genes absent in *C. depauperatus* and in *Cryptococcus* pathogens and those that are specifically present in *Cryptococcus* pathogenic species. (**A**) OGs absent in *C. depauperatus* but present in all other species. (**B**) OGs absent in *Cryptococcus* pathogens but present in all other species. (**C**) OGs absent in *Cryptococcus* pathogens but present in 95% of the other species. (**D**) OGs present in *Cryptococcus* pathogens and absent in all other species.
(XLSX)

S5 Appendix. Genes involved in capsule and melanin production, growth at 37˚C, and those that are highly expression in human cerebrospinal fluid (CSF) for *Cryptococcus* pathogens, nonpathogenic *Cryptococcus*, *Kwoniella*, and outgroup species.
(XLSX)

S6 Appendix. Transposable element (TE) content in *Cryptococcus* and *Kwoniella* genomes, centromere length raw data, and associated statistical analysis. (**A**) Centromere length across species (related to Fig 5A). (**B**) EarlGrey results for each TE category and species (related to Fig 5B). (**C**) Relative percentage of LTR retrotransposons found in centromeric (CEN) versus non-centromeric (Non-CEN) regions, normalized by the total percentage of LTRs (related to Fig 5C). (**D**) Percentage of TEs across species (related to Fig 5D). (**E**) Percentage of TEs in pathogenic and saprophytic *Cryptococcus* species (related to Fig 5E). (**F**) Percentage of TEs versus genome size. (**G**) Percentage of TEs versus average centromere length (related to Fig 5F).
(XLSX)

S7 Appendix. List of strains, primers, and plasmids used in this study.
(XLSX)

S1 Raw Images. Raw gel images for S2 and S16 Figs.
(PDF)

Acknowledgments

Author Contributions

Conceptualization: Marco A. Coelho, Márcia David-Palma, Sheng Sun, Christina A. Cuomo, Joseph Heitman.

Data curation: Marco A. Coelho, Minou Nowrousian, Christina A. Cuomo.

Formal analysis: Marco A. Coelho, Terrance Shea, Katharine Bowers, Sage McGinley-Smith, Minou Nowrousian, Christina A. Cuomo.

Funding acquisition: Christina A. Cuomo, Joseph Heitman.

Investigation: Marco A. Coelho, Márcia David-Palma, Arman W. Mohammad, Andreas Gnirke, Sheng Sun.

Project administration: Sheng Sun, Christina A. Cuomo, Joseph Heitman.

Resources: Andrey M. Yurkov, Christina A. Cuomo, Joseph Heitman.

Supervision: Christina A. Cuomo, Joseph Heitman.

Visualization: Marco A. Coelho.

Writing – original draft: Marco A. Coelho, Márcia David-Palma, Joseph Heitman.

Writing – review & editing: Marco A. Coelho, Márcia David-Palma, Sheng Sun, Christina A. Cuomo, Joseph Heitman.

References

1. Rayens E, Norris KA. Prevalence and healthcare burden of fungal infections in the United States, 2018. Open Forum Infect Dis. 2022; 9(1):ofab593. Epub 2022/01/18. https://doi.org/10.1093/ofid/ofab593 PMID: 35036461; PubMed Central PMCID: PMC8754384.

2. Fisher MC, Denning DW. The WHO fungal priority pathogens list as a game-changer. Nat Rev Microbiol 2023; 21(4):211–212. https://doi.org/10.1038/s41579-023-00861-x PMID: 36747091

3. Brown SP, Cornforth DM, Mideo N. Evolution of virulence in opportunistic pathogens: generalism, plasticity, and control. Trends Microbiol. 2012; 20(7):336–342. Epub 20120505. https://doi.org/10.1016/j.tim.2012.04.005 PMID: 22564248; PubMed Central PMCID: PMC3491314.

4. Polvi EJ, Li X, O'Meara TR, Leach MD, Cowen LE. Opportunistic yeast pathogens: reservoirs, virulence mechanisms, and therapeutic strategies. Cell Mol Life Sci. 2015; 72(12):2261–2287. https://doi.org/10.1007/s00018-015-1860-z PMID: 25700837

5. Francisco EC, de Jong AW, Hagen F. Cryptococcosis and *Cryptococcus*. Mycopathologia. 2021; 186 (5):729–731. https://doi.org/10.1007/s11046-021-00577-7

6. Steenbergen JN, Shuman HA, Casadevall A. *Cryptococcus neoformans* interactions with amoebae suggest an explanation for its virulence and intracellular pathogenic strategy in macrophages. Proc Natl Acad Sci U S A. 2001; 98(26):15245–15250. Epub 20011211. https://doi.org/10.1073/pnas.261418798 PMID: 11742090; PubMed Central PMCID: PMC65014.

7. Desjardins CA, Giamberardino C, Sykes SM, Yu CH, Tenor JL, Chen Y, et al. Population genomics and the evolution of virulence in the fungal pathogen *Cryptococcus neoformans*. Genome Res. 2017; 27(7):1207–1219. Epub 2017/06/15. https://doi.org/10.1101/gr.218727.116 PMID: 28611159; PubMed Central PMCID: PMC5495072.

8. Rokas A. Evolution of the human pathogenic lifestyle in fungi. Nat Microbiol. 2022; 7(5):607–619. https://doi.org/10.1038/s41564-022-01112-0 PMID: 35508719

9. Hagen F, Khayhan K, Theelen B, Kolecka A, Polacheck I, Sionov E, et al. Recognition of seven species in the *Cryptococcus gattii/Cryptococcus neoformans* species complex. Fungal Genet Biol. 2015; 78:16–48. https://doi.org/10.1016/j.fgb.2015.02.009 PMID: 25721988

10. Findley K, Rodriguez-Carres M, Metin B, Kroiss J, Fonseca A, Vilgalys R, et al. Phylogeny and phenotypic characterization of pathogenic *Cryptococcus* species and closely related saprobic taxa in the Tremellales. Eukaryot Cell. 2009; 8(3):353–361. Epub 2009/01/20. https://doi.org/10.1128/ec.00373-08 PMID: 19151324; PubMed Central PMCID: PMC2653247.

11. Passer AR, Clancey SA, Shea T, David-Palma M, Averette AF, Boekhout T, et al. Obligate sexual reproduction of a homothallic fungus closely related to the *Cryptococcus* pathogenic species complex. Elife. 2022; 11:e79114. https://doi.org/10.7554/eLife.79114 PMID: 35713948

12. Passer AR, Coelho MA, Billmyre RB, Nowrousian M, Mittelbach M, Yurkov AM, et al. Genetic and genomic analyses reveal boundaries between species closely related to *Cryptococcus* pathogens. MBio. 2019; 10(3). Epub 20190611. https://doi.org/10.1128/mBio.00764-19 PMID: 31186317; PubMed Central PMCID: PMC6561019.

13. Rajasingham R, Govender NP, Jordan A, Loyse A, Shroufi A, Denning DW, et al. The global burden of HIV-associated cryptococcal infection in adults in 2020: a modelling analysis. Lancet Infect Dis. 2022; 22(12):1748–1755. https://doi.org/10.1016/S1473-3099(22)00499-6 PMID: 36049486

14. Tan GSE, Singh R, Chong TYR, Su PQ, Lee JSS, Wong KJH, et al. Severe primary cutaneous *Cryptococcus gattii* causing ulcerative cellulitis in an immunocompetent patient. Lancet Infect Dis. 2019; 19 (10):1148. https://doi.org/10.1016/S1473-3099(19)30409-8 PMID: 31559968

15. Franco-Paredes C, Womack T, Bohlmeyer T, Sellers B, Hays A, Patel K, et al. Management of *Cryptococcus gattii* meningoencephalitis. Lancet Infect Dis. 2015; 15(3):348–355. https://doi.org/10.1016/S1473-3099(14)70945-4 PMID: 25467646

16. Farrer RA, Chang M, Davis MJ, van Dorp L, Yang DH, Shea T, et al. A new lineage of *Cryptococcus gattii* (VGV) discovered in the central zambezian Miombo woodlands. MBio. 2019; 10(6). Epub 20191112. https://doi.org/10.1128/mBio.02306-19 PMID: 31719178; PubMed Central PMCID: PMC6851281.

17. Liu XZ, Wang QM, Goker M, Groenewald M, Kachalkin AV, Lumbsch HT, et al. Towards an integrated phylogenetic classification of the Tremellomycetes. Stud Mycol. 2015; 81:85–147. Epub 2016/03/10. https://doi.org/10.1016/j.simyco.2015.12.001 PMID: 26955199; PubMed Central PMCID: PMC4777781.

18. Liu XZ, Wang QM, Theelen B, Groenewald M, Bai FY, Boekhout T. Phylogeny of tremellomycetous yeasts and related dimorphic and filamentous basidiomycetes reconstructed from multiple gene sequence analyses. Stud Mycol. 2015; 81:1–26. Epub 2016/03/10. https://doi.org/10.1016/j.simyco.2015.08.001 PMID: 26955196; PubMed Central PMCID: PMC4777771.

19. Li AH, Yuan FX, Groenewald M, Bensch K, Yurkov AM, Li K, et al. Diversity and phylogeny of basidiomycetous yeasts from plant leaves and soil: Proposal of two new orders, three new families, eight new genera and one hundred and seven new species. Stud Mycol. 2020; 96:17–140. https://doi.org/10.1016/j.simyco.2020.01.002 PMID: 32206137

20. Guerreiro MA, Springer DJ, Rodrigues JA, Rusche LN, Findley K, Heitman J, et al. Molecular and genetic evidence for a tetrapolar mating system in the basidiomycetous yeast *Kwoniella mangrovensis* and two novel sibling species. Eukaryot Cell. 2013;12. https://doi.org/10.1128/ec.00065-13 PMID: 23524993

21. Metin B, Findley K, Heitman J. The mating type locus *(MAT)* and sexual reproduction of *Cryptococcus heveanensis*: Insights into the evolution of sex and sex-determining chromosomal regions in Fungi. PLoS Genet. 2010; 6(5):e1000961. https://doi.org/10.1371/journal.pgen.1000961 PMID: 20502678

22. Sylvester K, Wang QM, James B, Mendez R, Hulfachor AB, Hittinger CT. Temperature and host preferences drive the diversification of *Saccharomyces* and other yeasts: a survey and the discovery of eight new yeast species. FEMS Yeast Res. 2015; 15(3). Epub 20150304. https://doi.org/10.1093/femsyr/fov002 PMID: 25743785.

23. Findley K, Sun S, Fraser JA, Hsueh YP, Averette AF, Li W, et al. Discovery of a modified tetrapolar sexual cycle in *Cryptococcus amylolentus* and the evolution of *MAT* in the *Cryptococcus* species complex. PLoS Genet. 2012; 8(2):e1002528. Epub 2012/02/24. https://doi.org/10.1371/journal.pgen.1002528 PMID: 22359516; PubMed Central PMCID: PMC3280970.

24. Sun S, Coelho MA, David-Palma M, Priest SJ, Heitman J. The Evolution of Sexual Reproduction and the Mating-Type Locus: Links to Pathogenesis of *Cryptococcus* Human Pathogenic Fungi. Annu Rev Genet. 2019; 53:417–444. Epub 20190919. https://doi.org/10.1146/annurev-genet-120116-024755 PMID: 31537103; PubMed Central PMCID: PMC7025156.

25. Nielsen K, Cox GM, Wang P, Toffaletti DL, Perfect JR, Heitman J. Sexual cycle of *Cryptococcus neoformans* var. *grubii* and virulence of congenic **a** and α isolates. Infect Immun. 2003; 71(9):4831–4841. Epub 2003/08/23. https://doi.org/10.1128/IAI.71.9.4831-4841.2003 PMID: 12933823; PubMed Central PMCID: PMC187335.

26. Boekhout T, Amend AS, El Baidouri F, Gabaldón T, Geml J, Mittelbach M, et al. Trends in yeast diversity discovery. Fungal Diversity. 2022; 114(1):491–537. https://doi.org/10.1007/s13225-021-00494-6 WOS:000725954300001.

27. Sun S, Yadav V, Billmyre RB, Cuomo CA, Nowrousian M, Wang L, et al. Fungal genome and mating system transitions facilitated by chromosomal translocations involving intercentromeric recombination. PLoS Biol. 2017; 15(8):e2002527. https://doi.org/10.1371/journal.pbio.2002527 PMID: 28800596

28. Janbon G, Ormerod KL, Paulet D, Byrnes EJ 3rd, Yadav V, Chatterjee G, et al. Analysis of the genome and transcriptome of *Cryptococcus neoformans var. grubii* reveals complex RNA expression and microevolution leading to virulence attenuation. PLoS Genet. 2014; 10(4):e1004261. Epub 2014/04/20. https://doi.org/10.1371/journal.pgen.1004261 PMID: 24743168; PubMed Central PMCID: PMC3990503.

29. Grohs Ferrareze PA, Maufrais C, Silva Araujo Streit R, Priest SJ, Cuomo CA, Heitman J, et al. Application of an optimized annotation pipeline to the *Cryptococcus deuterogattii* genome reveals dynamic primary metabolic gene clusters and genomic impact of RNAi loss. G3 (Bethesda). 2021; 11(2). https://doi.org/10.1093/g3journal/jkaa070 PMID: 33585873; PubMed Central PMCID: PMC8022950.

30. Priest SJ, Yadav V, Heitman J. Advances in understanding the evolution of fungal genome architecture. F1000Res. 2020; 9. Epub 20200727. https://doi.org/10.12688/f1000research.25424.1 PMID: 32765832; PubMed Central PMCID: PMC7385547.

31. Mehrabi R, Gohari AM, Kema GHJ. Karyotype variability in plant-pathogenic Fungi. Annu Rev Phytopathol. 2017; 55(1):483–503. https://doi.org/10.1146/annurev-phyto-080615-095928 PMID: 28777924.

32. Wellenreuther M, Mérot C, Berdan E, Bernatchez L. Going beyond SNPs: The role of structural genomic variants in adaptive evolution and species diversification. Mol Ecol. 2019; 28(6):1203–1209. https://doi.org/10.1111/mec.15066 PMID: 30834648

33. Wellband K, Mérot C, Linnansaari T, Elliott JAK, Curry RA, Bernatchez L. Chromosomal fusion and life history-associated genomic variation contribute to within-river local adaptation of Atlantic salmon. Mol Ecol. 2019; 28(6):1439–1459. Epub 20181221. https://doi.org/10.1111/mec.14965 PMID: 30506831.

34. Guerrero RF, Kirkpatrick M. Local adaptation and the evolution of chromosome fusions. Evolution. 2014; 68(10):2747–2756. Epub 20140801. https://doi.org/10.1111/evo.12481 PMID: 24964074.

35. Yadav V, Sun S, Heitman J. On the evolution of variation in sexual reproduction through the prism of eukaryotic microbes. Proc Natl Acad Sci. 2023; 120(10):e2219120120. https://doi.org/10.1073/pnas.2219120120 PMID: 36867686

36. Coelho MA, Bakkeren G, Sun S, Hood ME, Giraud T. Fungal Sex: The Basidiomycota. Microbiol Spectr. 2017; 5(3). Epub 2017/06/10. https://doi.org/10.1128/microbiolspec.FUNK-0046-2016 PMID: 28597825; PubMed Central PMCID: PMC5467461.

37. Hartmann FE, Duhamel M, Carpentier F, Hood ME, Foulongne-Oriol M, Silar P, et al. Recombination suppression and evolutionary strata around mating-type loci in fungi: documenting patterns and understanding evolutionary and mechanistic causes. New Phytol. 2021; 229(5):2470–2491. Epub 20201201. https://doi.org/10.1111/nph.17039 PMID: 33113229; PubMed Central PMCID: PMC7898863.

38. Selmecki A, Forche A, Berman J. Aneuploidy and isochromosome formation in drug-resistant *Candida albicans*. Science. 2006; 313(5785):367–370. https://doi.org/10.1126/science.1128242 PMID: 16857942

39. Bravo Ruiz G, Ross ZK, Holmes E, Schelenz S, Gow NAR, Lorenz A. Rapid and extensive karyotype diversification in haploid clinical *Candida auris* isolates. Curr Genet. 2019; 65(5):1217–1228. https://doi.org/10.1007/s00294-019-00976-w PMID: 31020384

40. Matson MEH, Liang Q, Lonardi S, Judelson HS. Karyotype variation, spontaneous genome rearrangements affecting chemical insensitivity, and expression level polymorphisms in the plant pathogen *Phytophthora infestans* revealed using its first chromosome-scale assembly. PLoS Pathog. 2022; 18(10):e1010869. https://doi.org/10.1371/journal.ppat.1010869 PMID: 36215336

41. Fan Y, Linardopoulou E, Friedman C, Williams E, Trask BJ. Genomic structure and evolution of the ancestral chromosome fusion site in 2q13-2q14.1 and paralogous regions on other human chromosomes. Genome Res. 2002; 12(11):1651–62. https://doi.org/10.1101/gr.337602 PMID: 12421751; PubMed Central PMCID: PMC187548.

42. Luo J, Sun X, Cormack BP, Boeke JD. Karyotype engineering by chromosome fusion leads to reproductive isolation in yeast. Nature. 2018; 560(7718):392–396. https://doi.org/10.1038/s41586-018-0374-x PMID: 30069047

43. Yadav V, Sun S, Coelho MA, Heitman J. Centromere scission drives chromosome shuffling and reproductive isolation. Proc Natl Acad Sci U S A. 2020; 117(14):7917–7928. Epub 2020/03/21. https://doi.org/10.1073/pnas.1918659117 PMID: 32193338; PubMed Central PMCID: PMC7149388.

44. de Vos JM, Augustijnen H, Bätscher L, Lucek K. Speciation through chromosomal fusion and fission in *Lepidoptera*. Philos Trans R Soc Lond B Biol Sci. 2020; 375(1806):20190539. Epub 20200713. https://doi.org/10.1098/rstb.2019.0539 PMID: 32654638; PubMed Central PMCID: PMC7423279.

45. Yin Y, Fan H, Zhou B, Hu Y, Fan G, Wang J, et al. Molecular mechanisms and topological consequences of drastic chromosomal rearrangements of muntjac deer. Nat Commun. 2021; 12(1):6858. https://doi.org/10.1038/s41467-021-27091-0 PMID: 34824214

46. Ijdo J, Baldini A, Ward DC, Reeders ST, Wells RA. Origin of human chromosome 2: an ancestral telomere-telomere fusion. Proc Natl Acad Sci U S A. 1991; 88(20):9051–9055. Epub 1991/10/15. https://doi.org/10.1073/pnas.88.20.9051 PMID: 1924367; PubMed Central PMCID: PMC52649.

47. Miga KH. Chromosome-specific centromere sequences provide an estimate of the ancestral chromosome 2 fusion event in Hominin genomes. J Hered. 2017; 108(1):45–52. Epub 20160716. https://doi.org/10.1093/jhered/esw039 PMID: 27423248.

48. Wang X, Jin D, Wang Z, Guo H, Zhang L, Wang L, et al. Telomere-centric genome repatterning determines recurring chromosome number reductions during the evolution of eukaryotes. New Phytol. 2015; 205(1):378–389. Epub 20140820. https://doi.org/10.1111/nph.12985 PMID: 25138576.

49. Lysak MA, Berr A, Pecinka A, Schmidt R, McBreen K, Schubert I. Mechanisms of chromosome number reduction in Arabidopsis thaliana and related Brassicaceae species. Proc Natl Acad Sci U S A. 2006; 103(13):5224–5229. Epub 20060320. https://doi.org/10.1073/pnas.0510791103 PMID: 16549785; PubMed Central PMCID: PMC1458822.

50. Fradin H, Kiontke K, Zegar C, Gutwein M, Lucas J, Kovtun M, et al. Genome architecture and evolution of a unichromosomal asexual nematode. Curr Biol. 2017; 27(19):2928–2939.e6. Epub 20170921. https://doi.org/10.1016/j.cub.2017.08.038 PMID: 28943090; PubMed Central PMCID: PMC5659720.

51. Gordon JL, Byrne KP, Wolfe KH. Mechanisms of chromosome number evolution in yeast. PLoS Genet. 2011; 7(7):e1002190. https://doi.org/10.1371/journal.pgen.1002190 PMID: 21811419

52. Cuomo CA, Guldener U, Xu JR, Trail F, Turgeon BG, Di Pietro A, et al. The *Fusarium graminearum* genome reveals a link between localized polymorphism and pathogen specialization. Science. 2007; 317(5843):1400–1402.

53. Ma LJ, van der Does HC, Borkovich KA, Coleman JJ, Daboussi MJ, Di Pietro A, et al. Comparative genomics reveals mobile pathogenicity chromosomes in *Fusarium*. Nature. 2010; 464(7287):367–373. https://doi.org/10.1038/nature08850 PMID: 20237561; PubMed Central PMCID: PMC3048781.

54. Connolly LR, Smith KM, Freitag M. The *Fusarium graminearum* histone H3 K27 methyltransferase KMT6 regulates development and expression of secondary metabolite gene clusters. PLoS Genet. 2013; 9(10):e1003916. Epub 20131031. https://doi.org/10.1371/journal.pgen.1003916 PMID: 24204317; PubMed Central PMCID: PMC3814326.

55. Sankaranarayanan SR, Ianiri G, Coelho MA, Reza MH, Thimmappa BC, Ganguly P, et al. Loss of centromere function drives karyotype evolution in closely related *Malassezia* species. Elife. 2020; 9. Epub 2020/01/21. https://doi.org/10.7554/eLife.53944 PMID: 31958060; PubMed Central PMCID: PMC7025860.

56. Coelho MA, Ianiri G, David-Palma M, Theelen B, Goyal R, Narayanan A, et al. Frequent transitions in mating-type locus chromosomal organization in *Malassezia* and early steps in sexual reproduction. Proc Natl Acad Sci. 2023; 120(32):e2305094120. https://doi.org/10.1073/pnas.2305094120 PMID: 37523560

57. Yurkov AM, Rohl O, Pontes A, Carvalho C, Maldonado C, Sampaio JP. Local climatic conditions constrain soil yeast diversity patterns in Mediterranean forests, woodlands and scrub biome. FEMS Yeast Res. 2016; 16(1):fov103. Epub 20151113. https://doi.org/10.1093/femsyr/fov103 PMID: 26568202.

58. Loftus BJ, Fung E, Roncaglia P, Rowley D, Amedeo P, Bruno D, et al. The genome of the basidiomycetous yeast and human pathogen Cryptococcus neoformans. Science. 2005; 307(5713):1321–1324. Epub 2005/01/18. https://doi.org/10.1126/science.1103773 PMID: 15653466; PubMed Central PMCID: PMC3520129.

59. D'Souza CA, Kronstad JW, Taylor G, Warren R, Yuen M, Hu G, et al. Genome variation in *Cryptococcus gattii*, an emerging pathogen of immunocompetent hosts. MBio. 2011; 2(1):e00342–10. Epub 2011/02/10. https://doi.org/10.1128/mBio.00342-10 PMID: 21304167; PubMed Central PMCID: PMC3037005.

60. Floudas D, Binder M, Riley R, Barry K, Blanchette RA, Henrissat B, et al. The Paleozoic origin of enzymatic lignin decomposition reconstructed from 31 fungal genomes. Science. 2012; 336(6089):1715–1719. Epub 2012/06/30. https://doi.org/10.1126/science.1221748 PMID: 22745431.

61. Sun S, Coelho MA, Heitman J, Nowrousian M. Convergent evolution of linked mating-type loci in basidiomycete fungi. PLoS Genet. 2019; 15(9):e1008365. https://doi.org/10.1371/journal.pgen.1008365 PMID: 31490920

62. Zhao R-L, Li G-J, Sánchez-Ramírez S, Stata M, Yang Z-L, Wu G, et al. A six-gene phylogenetic overview of Basidiomycota and allied phyla with estimated divergence times of higher taxa and a phyloproteomics perspective. Fungal Diversity. 2017; 84(1):43–74. https://doi.org/10.1007/s13225-017-0381-5

63. He M-Q, Zhao R-L, Hyde KD, Begerow D, Kemler M, Yurkov A, et al. Notes, outline and divergence times of Basidiomycota. Fungal Diversity. 2019; 99(1):105–367. https://doi.org/10.1007/s13225-019-00435-4

64. Casadevall A, Freij JB, Hann-Soden C, Taylor J. Continental drift and speciation of the *Cryptococcus neoformans* and *Cryptococcus gattii* species complexes. mSphere. 2017; 2(2). Epub 20170419. https://doi.org/10.1128/mSphere.00103-17 PMID: 28435888; PubMed Central PMCID: PMC5397565.

65. Sharpton TJ, Neafsey DE, Galagan JE, Taylor JW. Mechanisms of intron gain and loss in *Cryptococcus*. Genome Biol. 2008; 9(1):R24. Epub 20080130. https://doi.org/10.1186/gb-2008-9-1-r24 PMID: 18234113; PubMed Central PMCID: PMC2395259.

66. Yadav V, Sun S, Billmyre RB, Thimmappa BC, Shea T, Lintner R, et al. RNAi is a critical determinant of centromere evolution in closely related fungi. Proc Natl Acad Sci U S A. 2018; 115(12):3108–3113. Epub 2018/03/05. https://doi.org/10.1073/pnas.1713725115 PMID: 29507212.

67. Schotanus K, Yadav V, Heitman J. Epigenetic dynamics of centromeres and neocentromeres in *Cryptococcus deuterogattii*. PLoS Genet. 2021; 17(8):e1009743. Epub 2021/09/01. https://doi.org/10.1371/journal.pgen.1009743 PMID: 34464380; PubMed Central PMCID: PMC8407549.

68. Schotanus K, Heitman J. Centromere deletion in *Cryptococcus deuterogattii* leads to neocentromere formation and chromosome fusions. Elife. 2020; 9. Epub 2020/04/21. https://doi.org/10.7554/eLife.56026 PMID: 32310085; PubMed Central PMCID: PMC7188483.

69. Drillon G, Carbone A, Fischer G. SynChro: a fast and easy tool to reconstruct and visualize synteny blocks along eukaryotic chromosomes. PLoS ONE. 2014; 9(3):e92621. Epub 20140320. https://doi.org/10.1371/journal.pone.0092621 PMID: 24651407; PubMed Central PMCID: PMC3961402.

70. Kegel A, Betts-Lindroos H, Kanno T, Jeppsson K, Strom L, Katou Y, et al. Chromosome length influences replication-induced topological stress. Nature. 2011; 471(7338):392–396. Epub 20110302. https://doi.org/10.1038/nature09791 PMID: 21368764.

71. Furuyama S, Biggins S. Centromere identity is specified by a single centromeric nucleosome in budding yeast. Proc Natl Acad Sci U S A. 2007; 104(37):14706–14711. Epub 20070905. https://doi.org/10.1073/pnas.0706985104 PMID: 17804787; PubMed Central PMCID: PMC1976213.

72. Guin K, Sreekumar L, Sanyal K. Implications of the Evolutionary Trajectory of Centromeres in the Fungal Kingdom. Annu Rev Microbiol. 2020; 74:835–853. Epub 20200724. https://doi.org/10.1146/annurev-micro-011720-122512 PMID: 32706633.

73. Smith KM, Galazka JM, Phatale PA, Connolly LR, Freitag M. Centromeres of filamentous fungi. Chromosome Res. 2012; 20(5):635–656. https://doi.org/10.1007/s10577-012-9290-3 PMID: 22752455; PubMed Central PMCID: PMC3409310.

74. Sanyal K, Baum M, Carbon J. Centromeric DNA sequences in the pathogenic yeast Candida albicans are all different and unique. Proc Natl Acad Sci U S A. 2004; 101(31):11374–11379. Epub 20040722. https://doi.org/10.1073/pnas.0404318101 PMID: 15272074; PubMed Central PMCID: PMC509209.

75. Seidl Michael F, Kramer HM, Cook David E, Fiorin Gabriel L, van den Berg Grardy CM, Faino L, et al. Repetitive Elements Contribute to the Diversity and Evolution of Centromeres in the Fungal Genus Verticillium. MBio. 2020; 11(5):e01714–20. https://doi.org/10.1128/mBio.01714-20 PMID: 32900804

76. Sridhar S, Hori T, Nakagawa R, Fukagawa T, Sanyal K. Bridgin connects the outer kinetochore to centromeric chromatin. Nat Commun. 2021; 12(1):146. Epub 20210108. https://doi.org/10.1038/s41467-020-20161-9 PMID: 33420015; PubMed Central PMCID: PMC7794384.

77. Catania S, Dumesic PA, Pimentel H, Nasif A, Stoddard CI, Burke JE, et al. Evolutionary persistence of DNA methylation for millions of years after ancient loss of a *de novo* methyltransferase. Cell. 2020; 180(2):263–277.e20. Epub 20200116. https://doi.org/10.1016/j.cell.2019.12.012 PMID: 31955845; PubMed Central PMCID: PMC7197499.

78. Dumesic Phillip A, Homer Christina M, Moresco James J, Pack Lindsey R, Shanle Erin K, Coyle Scott M, et al. Product Binding Enforces the Genomic Specificity of a Yeast Polycomb Repressive Complex. Cell. 2015; 160(1):204–218. https://doi.org/10.1016/j.cell.2014.11.039 PMID: 25533783

79. Gao D, Jiang N, Wing RA, Jiang J, Jackson SA. Transposons play an important role in the evolution and diversification of centromeres among closely related species. Front Plant Sci. 2015; 6:216. Epub 20150407. https://doi.org/10.3389/fpls.2015.00216 PMID: 25904926; PubMed Central PMCID: PMC4387472.

80. Wong LH, Choo KH. Evolutionary dynamics of transposable elements at the centromere. Trends Genet. 2004; 20(12):611–616. https://doi.org/10.1016/j.tig.2004.09.011 PMID: 15522456.

81. Cheng Z, Dong F, Langdon T, Ouyang S, Buell CR, Gu M, et al. Functional rice centromeres are marked by a satellite repeat and a centromere-specific retrotransposon. Plant Cell. 2002; 14(8):1691–1704. https://doi.org/10.1105/tpc.003079 PMID: 12172016; PubMed Central PMCID: PMC151459.

82. Janbon G, Maeng S, Yang DH, Ko YJ, Jung KW, Moyrand F, et al. Characterizing the role of RNA silencing components in *Cryptococcus neoformans*. Fungal Genet Biol. 2010; 47(12):1070–1080. Epub 20101109. https://doi.org/10.1016/j.fgb.2010.10.005 PMID: 21067947; PubMed Central PMCID: PMC3021383.

83. Nakayashiki H, Kadotani N, Mayama S. Evolution and diversification of RNA silencing proteins in fungi. J Mol Evol. 2006; 63(1):127–135. Epub 20060616. https://doi.org/10.1007/s00239-005-0257-2 PMID: 16786437.

84. Feretzaki M, Billmyre RB, Clancey SA, Wang X, Heitman J. Gene network polymorphism illuminates loss and retention of novel RNAi silencing components in the *Cryptococcus* pathogenic species complex. PLoS Genet. 2016; 12(3):e1005868. Epub 20160304. https://doi.org/10.1371/journal.pgen.1005868 PMID: 26943821; PubMed Central PMCID: PMC4778953.

85. Dumesic PA, Natarajan P, Chen C, Drinnenberg IA, Schiller BJ, Thompson J, et al. Stalled spliceosomes are a signal for RNAi-mediated genome defense. Cell. 2013; 152(5):957–968. Epub 20130214. https://doi.org/10.1016/j.cell.2013.01.046 PMID: 23415457; PubMed Central PMCID: PMC3645481.

86. Burke JE, Longhurst AD, Natarajan P, Rao B, Liu J, Sales-Lee J, et al. A non-Dicer RNase III and four other novel factors required for RNAi-mediated transposon suppression in the human pathogenic yeast *Cryptococcus neoformans*. G3 (Bethesda). 2019; 9(7):2235–2244. Epub 20190709. https://doi.org/10.1534/g3.119.400330 PMID: 31092606; PubMed Central PMCID: PMC6643885.

87. Yu EY, Zahid SS, Ganduri S, Sutherland JH, Hsu M, Holloman WK, et al. Structurally distinct telomere-binding proteins in *Ustilago maydis* execute non-overlapping functions in telomere replication, recombination, and protection. Commun Biol. 2020; 3(1):777. Epub 2020/12/18. https://doi.org/10.1038/s42003-020-01505-z PMID: 33328546; PubMed Central PMCID: PMC7744550.

88. de Lange T. Shelterin-mediated telomere protection. Annu Rev Genet. 2018; 52:223–247. Epub 20180912. https://doi.org/10.1146/annurev-genet-032918-021921 PMID: 30208292.

89. Torres DE, Reckard AT, Klocko AD, Seidl MF. Nuclear genome organization in fungi: from gene folding to Rabl chromosomes. FEMS Microbiol Rev. 2023; 47(3). https://doi.org/10.1093/femsre/fuad021 PMID: 37197899; PubMed Central PMCID: PMC10246852.

90. Ungar L, Yosef N, Sela Y, Sharan R, Ruppin E, Kupiec M. A genome-wide screen for essential yeast genes that affect telomere length maintenance. Nucleic Acids Res. 2009; 37(12):3840–3849. Epub 20090422. https://doi.org/10.1093/nar/gkp259 PMID: 19386622; PubMed Central PMCID: PMC2709559.

91. Askree SH, Yehuda T, Smolikov S, Gurevich R, Hawk J, Coker C, et al. A genome-wide screen for Saccharomyces cerevisiae deletion mutants that affect telomere length. Proc Natl Acad Sci U S A. 2004; 101(23):8658–8663. Epub 20040525. https://doi.org/10.1073/pnas.0401263101 PMID: 15161972; PubMed Central PMCID: PMC423251.

92. Folco HD, Xiao H, Wheeler D, Feng H, Bai Y, Grewal SIS. The cysteine-rich domain in CENP-A chaperone Scm3HJURP ensures centromere targeting and kinetochore integrity. Nucleic Acids Res. 2023. Epub 20231212. https://doi.org/10.1093/nar/gkad1182 PMID: 38084929.

93. Camahort R, Li B, Florens L, Swanson SK, Washburn MP, Gerton JL. Scm3 is essential to recruit the histone H3 variant Cse4 to centromeres and to maintain a functional kinetochore. Mol Cell. 2007; 26(6):853–865. Epub 20070614. https://doi.org/10.1016/j.molcel.2007.05.013 PMID: 17569568.

94. Kim JH, Kang JS, Chan CS. Sli15 associates with the ipl1 protein kinase to promote proper chromosome segregation in Saccharomyces cerevisiae. J Cell Biol. 1999; 145(7):1381–1394. https://doi.org/10.1083/jcb.145.7.1381 PMID: 10385519; PubMed Central PMCID: PMC2133162.

95. Sherwin D, Gutierrez-Morton E, Bokros M, Haluska C, Wang Y. A new layer of regulation of chromosomal passenger complex (CPC) translocation in budding yeast. Mol Biol Cell. 2023; 34(10):ar97. Epub 20230705. https://doi.org/10.1091/mbc.E23-02-0063 PMID: 37405742; PubMed Central PMCID: PMC10551702.

96. Takacs T, Nemeth MT, Bohner F, Vagvolgyi C, Jankovics F, Wilson D, et al. Characterization and functional analysis of zinc trafficking in the human fungal pathogen *Candida parapsilosis*. Open Biol. 2022; 12(7):220077. Epub 20220713. https://doi.org/10.1098/rsob.220077 PMID: 35857903; PubMed Central PMCID: PMC9277298.

97. Lehtovirta-Morley LE, Alsarraf M, Wilson D. Pan-domain analysis of ZIP zinc transporters. Int J Mol Sci. 2017; 18(12). Epub 20171206. https://doi.org/10.3390/ijms18122631 PMID: 29211002; PubMed Central PMCID: PMC5751234.

98. Citiulo F, Jacobsen ID, Miramon P, Schild L, Brunke S, Zipfel P, et al. *Candida albicans* scavenges host zinc via Pra1 during endothelial invasion. PLoS Pathog. 2012; 8(6):e1002777. Epub 20120628. https://doi.org/10.1371/journal.ppat.1002777 PMID: 22761575; PubMed Central PMCID: PMC3386192.

99. Wilson D. An evolutionary perspective on zinc uptake by human fungal pathogens. Metallomics 2015; 7(6):979–985. https://doi.org/10.1039/c4mt00331d PMID: 25652414; PubMed Central PMCID: PMC4433550.

100. Roselletti E, Pericolini E, Nore A, Takacs P, Kozma B, Sala A, et al. Zinc prevents vaginal candidiasis by inhibiting expression of an inflammatory fungal protein. Sci Transl Med. 2023; 15(725):eadi3363. Epub 20231206. https://doi.org/10.1126/scitranslmed.adi3363 PMID: 38055800.

101. Almeida F, Wolf JM, Casadevall A. Virulence-associated enzymes of *Cryptococcus neoformans*. Eukaryot Cell. 2015; 14(12):1173–1185. Epub 20151009. https://doi.org/10.1128/EC.00103-15 PMID: 26453651; PubMed Central PMCID: PMC4664877.

102. Haynes BC, Skowyra ML, Spencer SJ, Gish SR, Williams M, Held EP, et al. Toward an integrated model of capsule regulation in *Cryptococcus neoformans*. PLoS Pathog. 2011; 7(12):e1002411. Epub 20111208. https://doi.org/10.1371/journal.ppat.1002411 PMID: 22174677; PubMed Central PMCID: PMC3234223.

103. O'Meara TR, Alspaugh JA. The *Cryptococcus neoformans* capsule: a sword and a shield. Clin Microbiol Rev. 2012; 25(3):387–408. https://doi.org/10.1128/CMR.00001-12 PMID: 22763631; PubMed Central PMCID: PMC3416491.

104. Lee D, Jang EH, Lee M, Kim SW, Lee Y, Lee KT, et al. Unraveling melanin biosynthesis and signaling networks in *Cryptococcus neoformans*. MBio. 2019; 10(5). Epub 20191001. https://doi.org/10.1128/mBio.02267-19 PMID: 31575776; PubMed Central PMCID: PMC6775464.

105. Cordero RJB, Camacho E, Casadevall A. Melanization in *Cryptococcus neoformans* requires complex regulation. MBio. 2020; 11(1). Epub 20200204. https://doi.org/10.1128/mBio.03313-19 PMID: 32019794; PubMed Central PMCID: PMC7002353.

106. Jung KW, Yang DH, Maeng S, Lee KT, So YS, Hong J, et al. Systematic functional profiling of transcription factor networks in *Cryptococcus neoformans*. Nat Commun. 2015; 6:6757. Epub 20150407. https://doi.org/10.1038/ncomms7757 PMID: 25849373; PubMed Central PMCID: PMC4391232.

107. Walton FJ, Idnurm A, Heitman J. Novel gene functions required for melanization of the human pathogen Cryptococcus neoformans. Mol Microbiol. 2005; 57(5):1381–1396. https://doi.org/10.1111/j.1365-2958.2005.04779.x PMID: 16102007.

108. Idnurm A, Reedy JL, Nussbaum JC, Heitman J. Cryptococcus neoformans virulence gene discovery through insertional mutagenesis. Eukaryot Cell. 2004; 3(2):420–429. https://doi.org/10.1128/EC.3.2.420-429.2004 PMID: 15075272; PubMed Central PMCID: PMC387659.

109. Stempinski PR, Zielinski JM, Dbouk NH, Huey ES, McCormack EC, Rubin AM, et al. Genetic contribution to high temperature tolerance in *Cryptococcus neoformans*. Genetics. 2021; 217(1):1–15. https://doi.org/10.1093/genetics/iyaa009 PMID: 33683363; PubMed Central PMCID: PMC8045695.

110. Yu CH, Sephton-Clark P, Tenor JL, Toffaletti DL, Giamberardino C, Haverkamp M, et al. Gene expression of diverse *Cryptococcus* isolates during infection of the human central nervous system. MBio. 2021; 12(6):e0231321. Epub 20211102. https://doi.org/10.1128/mBio.02313-21 PMID: 34724829; PubMed Central PMCID: PMC8561399.

111. Panepinto J, Liu L, Ramos J, Zhu X, Valyi-Nagy T, Eksi S, et al. The DEAD-box RNA helicase Vad1 regulates multiple virulence-associated genes in *Cryptococcus neoformans*. J Clin Invest. 2005; 115(3):632–641. https://doi.org/10.1172/JCI23048 PMID: 15765146; PubMed Central PMCID: PMC1051994.

112. King MC, Wilson AC. Evolution at two levels in humans and chimpanzees. Science. 1975; 188(4184):107–116. https://doi.org/10.1126/science.1090005 PMID: 1090005.

113. Lin X, Huang JC, Mitchell TG, Heitman J. Virulence Attributes and Hyphal Growth of C. neoformans Are Quantitative Traits and the MATα Allele Enhances Filamentation. PLoS Genet. 2006; 2(11):e187. https://doi.org/10.1371/journal.pgen.0020187 PMID: 17112316

114. Bahn YS, Sun S, Heitman J, Lin X. Microbe profile: *Cryptococcus neoformans* species complex. Microbiology (Reading). 2020; 166(9):797–799. https://doi.org/10.1099/mic.0.000973 PMID: 32956032; PubMed Central PMCID: PMC7717486.

115. Saijo T, Chen J, Chen SC, Rosen LB, Yi J, Sorrell TC, et al. Anti-granulocyte-macrophage colony-stimulating factor autoantibodies are a risk factor for central nervous system infection by *Cryptococcus gattii* in otherwise immunocompetent patients. MBio. 2014; 5(2):e00912–14. Epub 20140318. https://doi.org/10.1128/mBio.00912-14 PMID: 24643864; PubMed Central PMCID: PMC3967522.

116. Applen Clancey S, Ciccone EJ, Coelho MA, Davis J, Ding L, Betancourt R, et al. *Cryptococcus deuterogattii* VGIIa infection associated with travel to the Pacific Northwest outbreak region in an anti-granulocyte-macrophage colony-stimulating factor autoantibody-positive patient in the United States. MBio. 2019; 10(1). Epub 20190212. https://doi.org/10.1128/mBio.02733-18 PMID: 30755511; PubMed Central PMCID: PMC6372798.

117. Mixao V, Gabaldon T. Hybridization and emergence of virulence in opportunistic human yeast pathogens. Yeast. 2018; 35(1):5–20. Epub 20170914. https://doi.org/10.1002/yea.3242 PMID: 28681409; PubMed Central PMCID: PMC5813172.

118. Samarasinghe H, Xu J. Hybrids and hybridization in the *Cryptococcus neoformans* and *Cryptococcus gattii* species complexes. Infect Genet Evol. 2018; 66:245–255. Epub 2018/10/21. https://doi.org/10.1016/j.meegid.2018.10.011 PMID: 30342094.

119. Rhodes J, Desjardins CA, Sykes SM, Beale MA, Vanhove M, Sakthikumar S, et al. Tracing genetic exchange and biogeography of *Cryptococcus neoformans* var. *grubii* at the global population level. Genetics. 2017; 207(1):327–346. Epub 2017/07/07. https://doi.org/10.1534/genetics.117.203836 PMID: 28679543; PubMed Central PMCID: PMC5586382.

120. Todd RT, Forche A, Selmecki A. Ploidy variation in fungi: polyploidy, aneuploidy, and genome evolution. Microbiol Spectr. 2017;5(4). https://doi.org/10.1128/microbiolspec.FUNK-0051-2016 PMID: 28752816; PubMed Central PMCID: PMC5656283.

121. Fu C, Davy A, Holmes S, Sun S, Yadav V, Gusa A, et al. Dynamic genome plasticity during unisexual reproduction in the human fungal pathogen *Cryptococcus deneoformans*. PLoS Genet. 2021; 17(11): e1009935. Epub 2021/11/30. https://doi.org/10.1371/journal.pgen.1009935 PMID: 34843473; PubMed Central PMCID: PMC8670703.

122. Gusa A, Williams JD, Cho JE, Averette AF, Sun S, Shouse EM, et al. Transposon mobilization in the human fungal pathogen *Cryptococcus* is mutagenic during infection and promotes drug resistance in vitro. Proc Natl Acad Sci U S A. 2020; 117(18):9973–9980. Epub 20200417. https://doi.org/10.1073/pnas.2001451117 PMID: 32303657; PubMed Central PMCID: PMC7211991.

123. Priest SJ, Yadav V, Roth C, Dahlmann TA, Kuck U, Magwene PM, et al. Uncontrolled transposition following RNAi loss causes hypermutation and antifungal drug resistance in clinical isolates of *Cryptococcus neoformans*. Nat Microbiol. 2022; 7(8):1239–1251. Epub 20220802. https://doi.org/10.1038/s41564-022-01183-z PMID: 35918426.

124. Munoz JF, McEwen JG, Clay OK, Cuomo CA. Genome analysis reveals evolutionary mechanisms of adaptation in systemic dimorphic fungi. Sci Rep. 2018; 8(1):4473. Epub 20180314. https://doi.org/10.1038/s41598-018-22816-6 PMID: 29540755; PubMed Central PMCID: PMC5852033.

125. Cisse OH, Ma L, Dekker JP, Khil PP, Youn JH, Brenchley JM, et al. Genomic insights into the host specific adaptation of the *Pneumocystis genus*. Commun Biol. 2021; 4(1):305. Epub 20210308. https://doi.org/10.1038/s42003-021-01799-7 PMID: 33686174; PubMed Central PMCID: PMC7940399.

126. Ianiri G, Coelho MA, Ruchti F, Sparber F, McMahon TJ, Fu C, et al. HGT in the human and skin commensal *Malassezia*: A bacterially derived flavohemoglobin is required for NO resistance and host interaction. Proc Natl Acad Sci U S A. 2020; 117(27):15884–15894. Epub 20200623. https://doi.org/10.1073/pnas.2003473117 PMID: 32576698; PubMed Central PMCID: PMC7354939.

127. Sun S, Hoy MJ, Heitman J. Fungal pathogens. Curr Biol. 2020; 30(19):R1163–R1169. https://doi.org/10.1016/j.cub.2020.07.032 PMID: 33022261.

128. Fridrich A, Modepalli V, Lewandowska M, Aharoni R, Moran Y. Unravelling the developmental and functional significance of an ancient Argonaute duplication. Nat Commun. 2020; 11(1):6187. Epub 20201203. https://doi.org/10.1038/s41467-020-20003-8 PMID: 33273471; PubMed Central PMCID: PMC7713132.

129. Li Z, Li W, Guo M, Liu S, Liu L, Yu Y, et al. Origin, evolution and diversification of plant ARGONAUTE proteins. Plant J. 2022; 109(5):1086–1097. Epub 20211214. https://doi.org/10.1111/tpj.15615 PMID: 34845788; PubMed Central PMCID: PMC9208301.

130. Williams V, Del Poeta M. Role of glucose in the expression of *Cryptococcus neoformans* antiphagocytic protein 1, App1. Eukaryot Cell. 2011; 10(3):293–301. Epub 20110114. https://doi.org/10.1128/EC.00252-10 PMID: 21239626; PubMed Central PMCID: PMC3067477.

131. Body BA, Oneson RH, Herold DA. Use of cerebrospinal fluid lactic acid concentration in the diagnosis of fungal meningitis. Ann Clin Lab Sci. 1987; 17(6):429–434. PMID: 3688826.

132. Yu CH, Chen Y, Desjardins CA, Tenor JL, Toffaletti DL, Giamberardino C, et al. Landscape of gene expression variation of natural isolates of *Cryptococcus neoformans* in response to biologically relevant stresses. Microb Genom. 2020; 6(1). https://doi.org/10.1099/mgen.0.000319 PMID: 31860441; PubMed Central PMCID: PMC7067042.

133. Rude TH, Toffaletti DL, Cox GM, Perfect JR. Relationship of the glyoxylate pathway to the pathogenesis of *Cryptococcus neoformans*. Infect Immun. 2002; 70(10):5684–5694. https://doi.org/10.1128/IAI.70.10.5684–5694.2002 PMID: 12228298; PubMed Central PMCID: PMC128360.

134. Aksenova AY, Greenwell PW, Dominska M, Shishkin AA, Kim JC, Petes TD, et al. Genome rearrangements caused by interstitial telomeric sequences in yeast. Proc Natl Acad Sci U S A. 2013; 110 (49):19866–19871. Epub 20131104. https://doi.org/10.1073/pnas.1319313110 PMID: 24191060; PubMed Central PMCID: PMC3856781.

135. Fraser JA, Huang JC, Pukkila-Worley R, Alspaugh JA, Mitchell TG, Heitman J. Chromosomal translocation and segmental duplication in *Cryptococcus neoformans*. Eukaryot Cell. 2005; 4(2):401–406. https://doi.org/10.1128/ec.4.2.401–406.2005 PMID: 15701802; PubMed Central PMCID: PMC549341.

136. Shao Y, Lu N, Wu Z, Cai C, Wang S, Zhang L-L, et al. Creating a functional single-chromosome yeast. Nature. 2018; 560(7718):331–335. https://doi.org/10.1038/s41586-018-0382-x PMID: 30069045

137. Gu X, Ye T, Zhang X-R, Nie L, Wang H, Li W, et al. Single-chromosome fission yeast models reveal the configuration robustness of a functional genome. Cell Rep. 2022; 40(8):111237. https://doi.org/10.1016/j.celrep.2022.111237 PMID: 36001961

138. Stimpson KM, Song IY, Jauch A, Holtgreve-Grez H, Hayden KE, Bridger JM, et al. Telomere disruption results in non-random formation of de novo dicentric chromosomes involving acrocentric human chromosomes. PLoS Genet. 2010; 6(8). Epub 20100812. https://doi.org/10.1371/journal.pgen.1001061 PMID: 20711355; PubMed Central PMCID: PMC2920838.

139. de Lange T. How telomeres solve the end-protection problem. Science. 2009; 326(5955):948–952. https://doi.org/10.1126/science.1170633 PMID: 19965504; PubMed Central PMCID: PMC2819049.

140. de Lange T. A loopy view of telomere evolution. Front Genet. 2015; 6:321. Epub 20151020. https://doi.org/10.3389/fgene.2015.00321 PMID: 26539211; PubMed Central PMCID: PMC4612135.

141. Bautista-España D, Anastacio-Marcelino E, Horta-Valerdi G, Celestino-Montes A, Kojic M, Negrete-Abascal E, et al. The telomerase reverse transcriptase subunit from the dimorphic fungus *Ustilago maydis*. PLoS ONE. 2014; 9(10):e109981. https://doi.org/10.1371/journal.pone.0109981 PMID: 25299159

142. Zahid S, Aloe S, Sutherland JH, Holloman WK, Lue NF. *Ustilago maydis* telomere protein Pot1 harbors an extra N-terminal OB fold and regulates homology-directed DNA repair factors in a dichotomous and context-dependent manner. PLoS Genet. 2022; 18(5):e1010182. https://doi.org/10.1371/journal.pgen.1010182 PMID: 35587917

143. Sanpedro-Luna JA, Jacinto-Vázquez JJ, Anastacio-Marcelino E, Posadas-Gutiérrez CM, Olmos-Pineda I, González-Bernal JA, et al. Telomerase RNA plays a major role in the completion of the life cycle in *Ustilago maydis* and shares conserved domains with other Ustilaginales. PLoS ONE. 2023; 18(3):e0281251. Epub 20230323. https://doi.org/10.1371/journal.pone.0281251 PMID: 36952474; PubMed Central PMCID: PMC10035886.

144. Logeswaran D, Li Y, Akhter K, Podlevsky JD, Olson TL, Forsberg K, et al. Biogenesis of telomerase RNA from a protein-coding mRNA precursor. Proc Natl Acad Sci U S A. 2022; 119(41):e2204636119. Epub 20221005. https://doi.org/10.1073/pnas.2204636119 PMID: 36197996; PubMed Central PMCID: PMC9564094.

145. Gusa A, Yadav V, Roth C, Williams JD, Shouse EM, Magwene P, et al. Genome-wide analysis of heat stress-stimulated transposon mobility in the human fungal pathogen Cryptococcus deneoformans. Proc Natl Acad Sci U S A. 2023; 120(4):e2209831120. Epub 20230120. https://doi.org/10.1073/pnas.2209831120 PMID: 36669112; PubMed Central PMCID: PMC9942834.

146. Miao VP, Covert SF, VanEtten HD. A fungal gene for antibiotic resistance on a dispensable ("B") chromosome. Science. 1991; 254(5039):1773–1776. https://doi.org/10.1126/science.1763326 PMID: 1763326.

147. Coleman JJ, Rounsley SD, Rodriguez-Carres M, Kuo A, Wasmann CC, Grimwood J, et al. The genome of *Nectria haematococca*: contribution of supernumerary chromosomes to gene expansion. PLoS Genet. 2009; 5(8):e1000618. Epub 20090828. https://doi.org/10.1371/journal.pgen.1000618 PMID: 19714214; PubMed Central PMCID: PMC2725324.

148. Komluski J, Stukenbrock EH, Habig M. Non-Mendelian transmission of accessory chromosomes in fungi. Chromosome Res. 2022; 30(2–3):241–53. Epub 20220726. https://doi.org/10.1007/s10577-022-09691-8 PMID: 35881207; PubMed Central PMCID: PMC9508043.

149. Wang H, Huang R, Ren J, Tang L, Huang S, Chen X, et al. The evolution of mini-chromosomes in the fungal genus *Colletotrichum*. MBio. 2023; 14(4):e0062923. Epub 20230607. https://doi.org/10.1128/mbio.00629-23 PMID: 37283539; PubMed Central PMCID: PMC10470602.

150. Kominek J, Doering DT, Opulente DA, Shen X-X, Zhou X, DeVirgilio J, et al. Eukaryotic acquisition of a bacterial operon. Cell. 2019; 176(6):1356–1366.e10. https://doi.org/10.1016/j.cell.2019.01.034 PMID: 30799038

151. Fisher S, Barry A, Abreu J, Minie B, Nolan J, Delorey TM, et al. A scalable, fully automated process for construction of sequence-ready human exome targeted capture libraries. Genome Biol. 2011; 12(1):R1. Epub 20110104. https://doi.org/10.1186/gb-2011-12-1-r1 PMID: 21205303; PubMed Central PMCID: PMC3091298.

152. Gnerre S, Maccallum I, Przybylski D, Ribeiro FJ, Burton JN, Walker BJ, et al. High-quality draft assemblies of mammalian genomes from massively parallel sequence data. Proc Natl Acad Sci U S A. 2011;

108(4):1513–1518. Epub 20101227. https://doi.org/10.1073/pnas.1017351108 PMID: 21187386; PubMed Central PMCID: PMC3029755.

153. Koren S, Walenz BP, Berlin K, Miller JR, Bergman NH, Phillippy AM. Canu: scalable and accurate long-read assembly via adaptive k-mer weighting and repeat separation. Genome Res. 2017; 27 (5):722–736. Epub 20170315. https://doi.org/10.1101/gr.215087.116 PMID: 28298431; PubMed Central PMCID: PMC5411767.

154. Walker BJ, Abeel T, Shea T, Priest M, Abouelliel A, Sakthikumar S, et al. Pilon: an integrated tool for comprehensive microbial variant detection and genome assembly improvement. PLoS ONE. 2014; 9 (11):e112963. Epub 20141119. https://doi.org/10.1371/journal.pone.0112963 PMID: 25409509; PubMed Central PMCID: PMC4237348.

155. Li H, Durbin R. Fast and accurate short read alignment with Burrows-Wheeler transform. Bioinformatics. 2009; 25(14):1754–1760. Epub 20090518. https://doi.org/10.1093/bioinformatics/btp324 PMID: 19451168; PubMed Central PMCID: PMC2705234.

156. Li H. Minimap2: pairwise alignment for nucleotide sequences. Bioinformatics. 2018; 34(18):3094–3100. https://doi.org/10.1093/bioinformatics/bty191 PMID: 29750242; PubMed Central PMCID: PMC6137996.

157. Robinson JT, Thorvaldsdottir H, Winckler W, Guttman M, Lander ES, Getz G, et al. Integrative genomics viewer. Nat Biotechnol. 2011; 29(1):24–26. https://doi.org/10.1038/nbt.1754 PMID: 21221095; PubMed Central PMCID: PMC3346182.

158. Bruna T, Hoff KJ, Lomsadze A, Stanke M, Borodovsky M. BRAKER2: automatic eukaryotic genome annotation with GeneMark-EP+ and AUGUSTUS supported by a protein database. NAR Genom Bioinform. 2021; 3(1):lqaa108. Epub 20210106. https://doi.org/10.1093/nargab/lqaa108 PMID: 33575650; PubMed Central PMCID: PMC7787252.

159. Manni M, Berkeley MR, Seppey M, Simao FA, Zdobnov EM. BUSCO Update: Novel and Streamlined Workflows along with Broader and Deeper Phylogenetic Coverage for Scoring of Eukaryotic, Prokaryotic, and Viral Genomes. Mol Biol Evol. 2021; 38(10):4647–4654. https://doi.org/10.1093/molbev/msab199 PMID: 34320186; PubMed Central PMCID: PMC8476166.

160. Kriventseva EV, Kuznetsov D, Tegenfeldt F, Manni M, Dias R, Simao FA, et al. OrthoDB v10: sampling the diversity of animal, plant, fungal, protist, bacterial and viral genomes for evolutionary and functional annotations of orthologs. Nucleic Acids Res. 2019; 47(D1):D807–D811. https://doi.org/10.1093/nar/gky1053 PMID: 30395283; PubMed Central PMCID: PMC6323947.

161. Shishkin AA, Giannoukos G, Kucukural A, Ciulla D, Busby M, Surka C, et al. Simultaneous generation of many RNA-seq libraries in a single reaction. Nat Methods. 2015; 12(4):323–325. Epub 20150302. https://doi.org/10.1038/nmeth.3313 PMID: 25730492; PubMed Central PMCID: PMC4712044.

162. Dobin A, Davis CA, Schlesinger F, Drenkow J, Zaleski C, Jha S, et al. STAR: ultrafast universal RNA-seq aligner. Bioinformatics. 2013; 29(1):15–21. Epub 20121025. https://doi.org/10.1093/bioinformatics/bts635 PMID: 23104886; PubMed Central PMCID: PMC3530905.

163. Krueger F, Andrews SR. Bismark: a flexible aligner and methylation caller for Bisulfite-Seq applications. Bioinformatics. 2011; 27(11):1571–1572. Epub 20110414. https://doi.org/10.1093/bioinformatics/btr167 PMID: 21493656; PubMed Central PMCID: PMC3102221.

164. Simpson JT, Workman RE, Zuzarte PC, David M, Dursi LJ, Timp W. Detecting DNA cytosine methylation using nanopore sequencing. Nat Methods. 2017; 14(4):407–410. Epub 20170220. https://doi.org/10.1038/nmeth.4184 PMID: 28218898.

165. Lopez-Delisle L, Rabbani L, Wolff J, Bhardwaj V, Backofen R, Gruning B, et al. pyGenomeTracks: reproducible plots for multivariate genomic datasets. Bioinformatics. 2021; 37(3):422–423. https://doi.org/10.1093/bioinformatics/btaa692 PMID: 32745185; PubMed Central PMCID: PMC8058774.

166. Emms DM, Kelly S. OrthoFinder: phylogenetic orthology inference for comparative genomics. Genome Biol. 2019; 20(1):238. Epub 20191114. https://doi.org/10.1186/s13059-019-1832-y PMID: 31727128; PubMed Central PMCID: PMC6857279.

167. Katoh K, Standley DM. MAFFT multiple sequence alignment software version 7: improvements in performance and usability. Mol Biol Evol. 2013; 30(4):772–780. Epub 20130116. https://doi.org/10.1093/molbev/mst010 PMID: 23329690; PubMed Central PMCID: PMC3603318.

168. Capella-Gutierrez S, Silla-Martinez JM, Gabaldon T. trimAl: a tool for automated alignment trimming in large-scale phylogenetic analyses. Bioinformatics. 2009; 25(15):1972–1973. Epub 20090608. https://doi.org/10.1093/bioinformatics/btp348 PMID: 19505945; PubMed Central PMCID: PMC2712344.

169. Siol M, Coudoux T, Ravel S, De Mita S. EggLib 3: a python package for population genetics and genomics. Mol Ecol Resour. 2022; 22(8):3176–3187. Epub 2022/06/27. https://doi.org/10.1111/1755-0998.13672 PMID: 35753060.

170. Yang Z, Nielsen R. Mutation-selection models of codon substitution and their use to estimate selective strengths on codon usage. Mol Biol Evol. 2008; 25(3):568–579. Epub 20080103. https://doi.org/10.1093/molbev/msm284 PMID: 18178545.

171. Yang Z. PAML 4: phylogenetic analysis by maximum likelihood. Mol Biol Evol. 2007; 24(8):1586–1591. Epub 20070504. https://doi.org/10.1093/molbev/msm088 PMID: 17483113.

172. Alvarez-Carretero S, Kapli P, Yang Z. Beginner's guide on the use of PAML to detect positive selection. Mol Biol Evol. 2023; 40(4). Epub 2023/04/25. https://doi.org/10.1093/molbev/msad041 PMID: 37096789; PubMed Central PMCID: PMC10127084.

173. Minh BQ, Schmidt HA, Chernomor O, Schrempf D, Woodhams MD, von Haeseler A, et al. IQ-TREE 2: New Models and Efficient Methods for Phylogenetic Inference in the Genomic Era. Mol Biol Evol. 2020; 37(5):1530–1534. https://doi.org/10.1093/molbev/msaa015 PMID: 32011700; PubMed Central PMCID: PMC7182206.

174. Tamura K, Stecher G, Kumar S. MEGA11: Molecular Evolutionary Genetics Analysis Version 11. Mol Biol Evol. 2021; 38(7):3022–3027. https://doi.org/10.1093/molbev/msab120 PMID: 33892491; PubMed Central PMCID: PMC8233496.

175. Tamura K, Tao Q, Kumar S. Theoretical Foundation of the RelTime Method for Estimating Divergence Times from Variable Evolutionary Rates. Mol Biol Evol. 2018; 35(7):1770–1782. https://doi.org/10.1093/molbev/msy044 PMID: 29893954; PubMed Central PMCID: PMC5995221.

176. Kumar S, Stecher G, Suleski M, Hedges SB. TimeTree: a resource for timelines, timetrees, and divergence times. Mol Biol Evol. 2017; 34(7):1812–1819. Epub 2017/04/08. https://doi.org/10.1093/molbev/msx116 PMID: 28387841.

177. Letunic I, Bork P. Interactive Tree Of Life (iTOL) v5: an online tool for phylogenetic tree display and annotation. Nucleic Acids Res. 2021; 49(W1):W293–W296. https://doi.org/10.1093/nar/gkab301 PMID: 33885785; PubMed Central PMCID: PMC8265157.

178. Wang Y, Tang H, Debarry JD, Tan X, Li J, Wang X, et al. MCScanX: a toolkit for detection and evolutionary analysis of gene synteny and collinearity. Nucleic Acids Res. 2012; 40(7):e49. Epub 20120104. https://doi.org/10.1093/nar/gkr1293 PMID: 22217600; PubMed Central PMCID: PMC3326336.

179. Sullivan MJ, Petty NK, Beatson SA. Easyfig: a genome comparison visualizer. Bioinformatics. 2011; 27(7):1009–1010. Epub 20110128. https://doi.org/10.1093/bioinformatics/btr039 PMID: 21278367; PubMed Central PMCID: PMC3065679.

180. Baril T, Galbraith J, Hayward A. Earl Grey: a fully automated user-friendly transposable element annotation and analysis pipeline. bioRxiv [Preprint]. 2023:2022.06.30.498289. https://doi.org/10.1101/2022.06.30.498289

181. Quinlan AR, Hall IM. BEDTools: a flexible suite of utilities for comparing genomic features. Bioinformatics. 2010; 26(6):841–842. Epub 20100128. https://doi.org/10.1093/bioinformatics/btq033 PMID: 20110278; PubMed Central PMCID: PMC2832824.

182. Toffaletti DL, Rude TH, Johnston SA, Durack DT, Perfect JR. Gene transfer in *Cryptococcus neoformans* by use of biolistic delivery of DNA. J Bacteriol. 1993; 175(5):1405–1411. Epub 1993/03/01. https://doi.org/10.1128/jb.175.5.1405–1411.1993 PMID: 8444802; PubMed Central PMCID: PMC193227.

183. Belton JM, Dekker J. Hi-C in budding yeast. Cold Spring Harb Protoc. 2015; 2015(7):649–661. Epub 2015/07/03. https://doi.org/10.1101/pdb.prot085209 PMID: 26134906.

184. Rao SS, Huntley MH, Durand NC, Stamenova EK, Bochkov ID, Robinson JT, et al. A 3D map of the human genome at kilobase resolution reveals principles of chromatin looping. Cell. 2014; 159 (7):1665–1680. Epub 20141211. https://doi.org/10.1016/j.cell.2014.11.021 PMID: 25497547; PubMed Central PMCID: PMC5635824.